Arab American University-Jenin

Faculty of Graduate Studies

Fabrication and Characterization of Wide Band Photoconductor Array

By

Sufyan Rateb Shehada

Supervisor

Dr. Muayad Abu Saa

Co. Supervisor

Dr. Hazem Khanfar

This thesis was submitted in partial fulfillment of the requirements for the Master's degree in

Physics

September/2017

Fabrication and Characterization of Wide Band Photoconductor Array

By

Sufyan R. S. Shehada

This thesis was defended successfully on…….and approved by:

Committee members	Signature
1. Dr. Muayad Abu Saa (Supervisor)	…….
2. Dr. Hazem Khanfar (Co-supervisor)	.....
3. Prof. Dr. Atef Fayez Qasrawi (Internal Examiner)	…….
4. Dr Mohammad Elsaid (External Examiner)	.....

Declaration

The work provided in this thesis, unless otherwise referened, is the researcher's own work and has not been submitted elsewhere for any other degree or qualification.

Name: Sufyan Shehada

Signature:

Date:

To My Parents

Acknowledgments

This work would not have been possible without the support and guidance I received from a great number of family, friends and colleagues. First, I would like to thank my Mom and my Dad for their perpetual love and support throughout my extended academic journey. I also thank all of my friends for their support and encouragement throughout these challenging years.

Also, I would like to thank my advisors, Dr. Muayad Abu Saa, Dr. Hazem Khanfar and Prof. Dr. Atef Qasrawi for their mentorship throughout my time at the University of AAUJ. They provided me with a clear example to follow.

Abstract

In this thesis, a wide band photoconductor array is designed and characterized. The wide band photoconductor array is designed from materials exhibiting energy band gaps of values in the range 1.1-3.33 eV. Our photoconductor array consists of Cadmium sulfide, Gallium Selenide, Indium Selenide, Germanium, Zinc Sulfide and Indium Selenide/ Cadmium sulfide heterojunction. The photoconductor array is subjected to various types of laser excitations including lasers of wavelengths of 406, 632, 850 and 1550 nm and tungsten light. The measurements allowed determining the array photoresponsivity, photosensitivity, external quantum efficiency and internal quantum efficiency.

The photosensitivity and generated photocurrent increase with power for lasers and tungsten light while external quantum efficiency, internal quantum efficiency and photoresponsivity decrease with power of lasers and tungsten.

The maximum value of photosensitivity is achieved for Cadmium sulfide while the maximum value of generated photocurrent is achieved for connected array. The maximum values of external quantum efficiency, internal quantum efficiency and photoresponsivity are achieved for Indium Selenide.

Keywords: photoconductor, photoresponsivity, external quantum efficiency, internal quantum efficiency, photosensitivity.

Table of Contents

List of tables

List of Figures

Chapter One
Introduction and Literature Survey

Materials can be divided into three types: insulators, semiconductors, and conductors based on their electrical resistivity and conductivity. Typically, the resistivity of insulators is larger than 10^{12} Ohm.cm, the resistivity of conductors is in the range of 10^{-6} to 10^{-5} Ohm.cm, and the resistivity of semiconductors is in the range of 10^{-5} to 10^{11} Ohm.cm [1,2]. Electrical resistivity of semiconductors depends on temperature, illumination and doping. Semiconductors have two energy bands, conduction band and valence band. The band gap is the energy difference between the bottom of the conduction band and the top of the valence band [2]. The band diagram is shown in figure1.1.

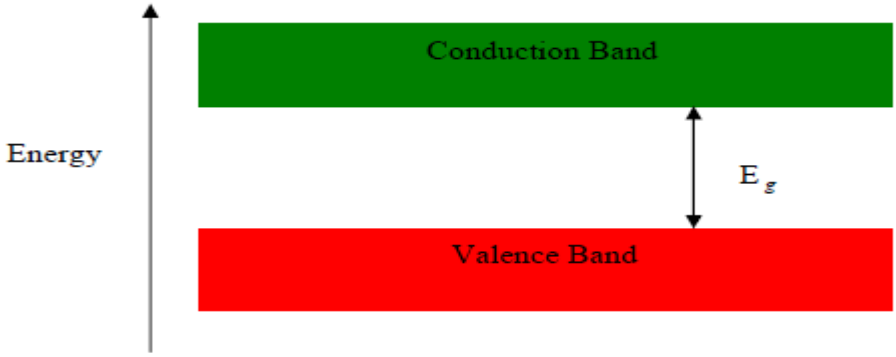

Fig. 1.1: The band diagram of a semiconductor

When an electron in the valence band possess enough energy (e.g. through incident photon), electron will be excited to the conduction band and leaves a hole in the valence band [3]. The electric carriers (electrons in the conduction band and the holes in the valence band) contribute to increasing the electrical conductivity. Because of these properties,

semiconductors have many areas of applications such as, transistors [4], switches [5], temperature sensors [6], photovoltaic devices solar cell [7], photo electronic devices [8] and photodetectors [9].

A photodetector is a device that converts an optical energy into another type of energy, (ex: electrical energy) [10]. Photodetectors can be sorted into several types, such as phototransistors [11], heterojunction photodiode [12]), infrared diodes [13], photodiodes [14] and photoconductors [15]. The working mechanism of photodetector is based on the photoelectric effect [16]. In a semiconductor material that is illuminated by an optical beam, if the photon energy is larger than the energy band gap of the semiconductor material, then for each absorbed photon an electron is transmitted to the conduction band. Different types of transitions are possible and different working mechanisms, such as interband, interband impurity and barrier transitions [17,18]. When external electric field applied, it is possible to collect the electrons in an external circuit and convert the optical signal into an electrical signal. In a photodiode the external quantum efficiency cannot be higher than one [19]. Also, it has small responsivity [20]. But it has fast response time. Photoconductors, on the other hand, are having high responsivity values and external quantum efficiency [21].Also, photoconductors are capable of high gain [22]. The photodiodes have a junction (i.e. p-n, p-i-n or Schottky) to separate and collect the photogenerated carriers [23,24]. They are commonly used in industrial applications due to their high performance and low cost. On the contrary, the Photoconductors do not have the same structure and they are based on photoconductivity [25], which is the change of conductivity of a semiconductor when it is exposed to light. When photoconductors are compared with photodiodes, it is easy to fabricate a photoconductor consists simply of a slab of semiconductor, in bulk or thin-film form, with Ohmic contacts affixed to the opposite ends [26] as shown in figure 1.2. The photoconductors are usually synthesis with relatively simple processes like thermal evaporation

and sputtering [27]. In our study, we are interested in the photoconductor device in order to design photoconductor array.

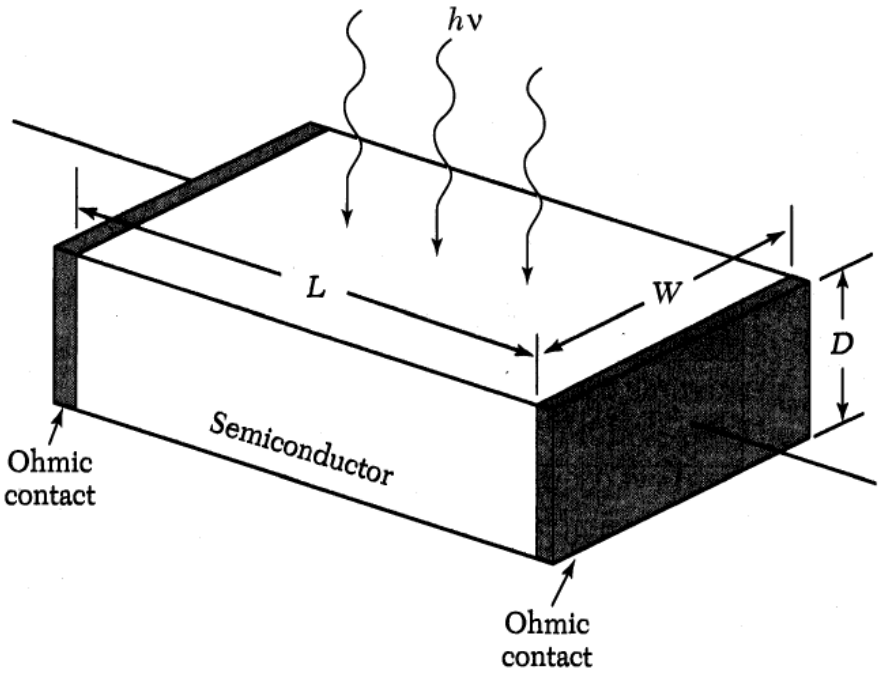

Fig.1.2: photoconductor that consists of a slab of semiconductor and two Ohmic contacts at the ends.

Photoconductor is named as light-dependent resistor or photoresistor [28]. It is an important type of photodetectors which is based on the phenomenon of photoconductivity. Photoconductor has a high conductivity due to the absorption of a suitable photon energy for electromagnetic radiation, such as infrared (IR), ultraviolet (UV) light and visible light [29]. Photoconductors have large resistance in the dark and high conductivity under suitable illumination with a photon energy that is larger than the band gap energy of the semiconductor [30]. Typically, photoconductor has a semiconductor layer that is sandwiched by two Ohmic contacts. Photoconductors are used for detecting radiation in the UV, Visible and near IR region [29]. Also, it can be used for detecting X-rays. Furthermore,

it has many applications in environmental monitoring [31], optical communications and military fields [32, 33]. The typical photodetector performance parameters are photoresponsivity [34], external quantum efficiency [35], photosensitivity [36], internal quantum efficiency [37]. Based on these parameters, the performance of the photoconductor is evaluated. These parameters will be discussed in the next chapter.

Thesis Outline

In this thesis, photoconductor array is proposed and fabricated, its performance is characterized and the working principle was also discussed.

This thesis is organized into 5 chapters.

Chapter 1: Introduction. This chapter covers the backgrounds and motivations of the photoconductor and an outline of this thesis.

Chapter 2: Theoretical Backgrounds. This chapter describes backgrounds reviews of materials properties, Optical absorption, energy band gap and the parameters of photoconductors.

Chapter 3: Experimental Details. This chapter shows Photoconductor array thin film preparation, Optical measurements and Current-Voltage Measurements in details.

Chapter 4: Results and Discussion. This chapter discusses Optical properties, energy band gap and photoelectric properties in details.

Chapter 5: Conclusion.

Chapter Two
Theoretical Background

2.1 Material properties

Many types of semiconductors are used in photoconductor devices, such as Silicon [38], InGaAs [39], GaN [40], ZnO [41], GaAs [42], Graphene–metal junction. Also, Silicon and GaN are used for UV photodetection [43,44]. For our photoconductor array we used the following material in manufacturing of our photoconductor array because they have a vary good properties that support our aim of this work.

Cadmium sulfide (CdS) is a semiconducting that is used in many applications. The wide direct band gap of (2.4 eV) [45] at room temperature has been considered as a prospective property for using it in optoelectronic devices. Also, compact crystallographic cell structure, low absorption loss and electronic affinity make CdS as a promising optoelectronic device for making solar cells with $CuInS_2$ (CIS), $CuInSe_2$ (CISe) and InP [46]. Thin films of CdS have other applications such as electrochemical cells [47], gas sensors [48], CdS NB MESFET photodetector [49] and metal-Schottky barrier cells [41]. It is mainly used as an optical window material. Nanoparticles of CdS doped with other semiconductors serve as photo sensor detection [50]. Thin films of CdS can be grown by physical and chemical methods such as chemical bath deposition (CBD) [51,52] and vacuum deposition [53].

Gallium Selenide (GaSe) is a member of III-VI semiconductor family. GaSe is an important material in many fields of both fundamental research and technical applications because of

it's structural, optical, electronic, photoelectronic properties. It is an excellent nonlinear optical material with an indirect band gap of 2.11 eV .The direct band gap is higher than it's indirect band gap by 25 meV [54, 55]. GaSe has many applications in photoelectronic devices [56, 57], photoelectric analyzers of polarized light [58], nonlinear optics, terahertz (THz) generation [59], detectors for monitoring high energy Muon beams [60, 61], X-ray beam detection [62] and light detection at ultraviolet wavelengths [63]. GaSe thin films had been grown by using different growing techniques [64,65].

Indium Selenide (InSe) is very attractive material for fabrication of new types of optoelectronic devices in the form of thin films. InSe has different growth techniques such as molecular beam epitaxy (MBE) [66], vapor deposition [67] and evaporation techniques [68]. The structural properties of InSe were studied [69,70,71,72]. It provides an important class of direct band gap semiconductors [73,74, 75, 76, 77]. Also, there is In_2Se_3 with phasesα, β and γ with energy band gap of 1.42 eV, 1.55 eV and 2 eV, respectively [78]. InSe has Small effective mass in the conduction band [79], large electron mobility [80] at room temperature due to weak electron–phonon scattering [81] and optical activity in absorption and emission [82]. Because of these properties, they are widely used in many applications such as solar energy conversion [83], terahertz generation [84], nonlinear optics [85], solar cell fabrication [86], photodiodes [87], rectifiers [88,89], gas sensors [90], detectors [91] and switching devices [92].

Germanium (Ge) is an indirect band gap semiconductor which possesses many properties such as high refractive index, small effective mass and high mobility as compared to Si, It has a cubic-F lattice at room temperature. The energy band gap of Ge could be tuned from

(0.67eV bulk) to (2eV 3-nm-diameter nanocrystals) [93,94]. Oxygen implementer is an important factor along with quantum confinement which changes the optical properties of Ge and making it a promising material for efficiently absorbing photons in solar cell applications [95], MOSFETs [96], photodetectors [97], IR laser radiation detectors [98] and high-speed transistors [99]. Compared to devices based on III-V semiconductors, devices based-on Ge has lower cost due to the material and the fabrication [100, 101].

Zinc Sulfide (ZnS) is an important II-VI group semiconductor with a direct band gap between (3.5eV -3.7 eV) [102]. ZnS can be found in different crystal structures such as cubic zinc blende (sphalerite) and hexagonal (wurtzite). Cubic form of ZnS has a band gap of 3.54 eV while the hexagonal form of ZnS has a band gap of 3.91 eV [103, 104]. Because ZnS has high index of refraction, high transmittance in the visible range [105], it is used in many applications such as light-emitting diodes [106], multilayer dielectric filters [107], spintronics [108], photocatalysts [109] sensors [110], injection lasers [111], thin film electroluminescent devices [112], infrared windows [113] and solar cells [114]. Many techniques were used to produce ZnS such as spray pyrolysis [115], thermal evaporation [116], molecular beam epitaxy [117], chemical bath deposition [118], photochemical deposition technique [119], atomic layer deposition [120] and RF reactive sputtering [121].

2.2 Optical absorption and energy band gap

Intrinsic optical absorption of one photon across the band gap is the dominant optical absorption process in a semiconductor. When the energy of the incident photon (hν) is

larger than the band gap energy, the excitation of electron from the valence band to the conduction band occurs. Photons passing through the material are then absorbed and the number of electron-hole pairs generated depends on the number of incident photons $\Phi_o(\nu)$ per unit area, per unit time and per unit energy. Frequency (ν) is related to wavelength (λ) through the relation, $\upsilon = c/\lambda$, where c is the velocity of light in a vacuum. Photon flux $\Phi(x, \upsilon)$ decreases exponentially inside the semiconductor according to the relation [122],

$$\phi(x,\nu) = \phi o(\nu)\ \exp(-\alpha k) \qquad (2.1)$$

Where α is the absorption coefficient of the material given by $\alpha = 4\pi k\upsilon/c$ with k is the extinction coefficient. The absorption coefficient can be deduced from the absorption spectra using the relation,

$$I = I_0 \exp(-\alpha d) \qquad (2.2)$$

Where I is the transmitted intensity and I_0 is the incident intensity of the light and d is the thickness of the film. For the parabolic band structure, the relation between absorption coefficient and band gap of the material is given by [123, 124],

$$\alpha h\nu = C\left(h\nu - E_g\right)^m \qquad (2.3)$$

Where C is a constant factor determined by the transition probability, and m is a number that depends on the type of transition process and h is plank's constant, Eg is the optical energy band gap. α can be expressed as a function of photon energy ($h\nu$). Possible values of m are 1/2, 2, 3/2, and 3 for allowed direct, allowed indirect, forbidden direct and forbidden indirect electronic transitions respectively [125, 126, 127, 128]. In the case of allowed direct band gap material, $m = 1/2$. From the plot between $(\alpha h\nu)^2$ and $h\nu$ we obtain a

straight line, and its intercept with the horizontal axis is the energy band gap of a semiconductor.

2.3 External Quantum Efficiency (EQE)

External Quantum Efficiency is defined as the ratio of the number of photogenerated charges current to the number of incident photons on the photoconductor [129, 130]. EQE is a function of wavelength, absorption coefficient and light frequency.

$$EQE(\lambda) = \frac{I_{Ph}}{Ps}\frac{hc}{\lambda e} \qquad (2.4)$$

Where I_d is the dark current, I_l is the light current and I_{ph} = (I_l - I_d) is the photocurrent, s is effective area , P is the incident light power, c is the speed of light in vacuum, λ is the wavelength of the incident light and e is the electron charge [131].

2.4 Internal Quantum Efficiency (IQE)

It is defined as the ratio between the number of the electron-hole pairs created by the light and the number of the absorbed photons. Not all generated carries (electrons and holes) can reach the electrodes because of loss mechanisms. The IQE is measured from EQE because it is not easy to calculate it directly [132].

$$IQE(\lambda) = \frac{EQE(\lambda)}{1 - T - R} \qquad (2.5)$$

Where R is the spectral reflectance and the device transmittance T [129].

2.5 Photoresponsivity

The photoresponsivity is defined as the ratio of the output photocurrent signal to the power of the input optical signal. It is an important parameter that tells us the available output signal of a photoconductor for a given input signal (light signal) [133] R_S is:

$$R_S = \frac{I_{ph}}{Ps} \qquad (2.6)$$

R_S is a measure of the effectiveness of the conversion of light power into electrical current [134].

2.6 Photosensitivity

Photosensitivity is defined as the ratio of photo-generated current to dark current in the photoconductor [135]. S is given by the formula:

$$S = \frac{I_{\mathrm{ph}}}{I_d} \qquad (2.7)$$

Where I_d is the dark current, I_l is the light current and $I_{ph} = (I_l - I_d)$ is the photocurrent [136].

Chapter Three
Experimental Details

3.1 Photoconductor array thin film preparation

The photoconductor array which consists of CdS, GaSe, InSe, ZnS and Ge thin films is prepared by thermal evaporation system (VCM 600 V2) that is shown in figure 3.1.

Fig. 3.1: Norm VCM 600 physical vapor deposition system.

In the preparation process the glass substrate was cleaned by using ultrasonic machine being arranged to work at 60^{o} C for 20 minutes. All glass substrates covered by Teflon expect the sides [figure 3.2] we evaporate Indium metal in the sides of the glass substrates to achieve electrical contact. An ignot of mass of 0.2g were placed in the tungsten boat

andthe glass substrates are placed on the sample holder at 20 cm above tungsten boat. Then, manual shutter and the chamber are closed. Thermal evaporation steps were as follows:

- The vent is closed.
- The main power switch and rough pump are turned on.
- When 10 mbar pressure is achieved turbo pump is turned on and we wait till it reach a pressure value of 10^{-5} mbar. Then we start the evaporation by heating tungsten boat by increasing the current. After that the shutter is opened.
- At a thickness of 1 μm read by thickness monitor , the shutter and current were turned off.
- Turbo pump and rough pump were then closed.

The samples were divided into 5 regions by Teflon. In each uncovered region we evaporate one of the following materials CdS, GaSe, InSe, ZnS and Ge following the same previously descried steps .All samples were kept at the same thickness as shown in figure 3.2.

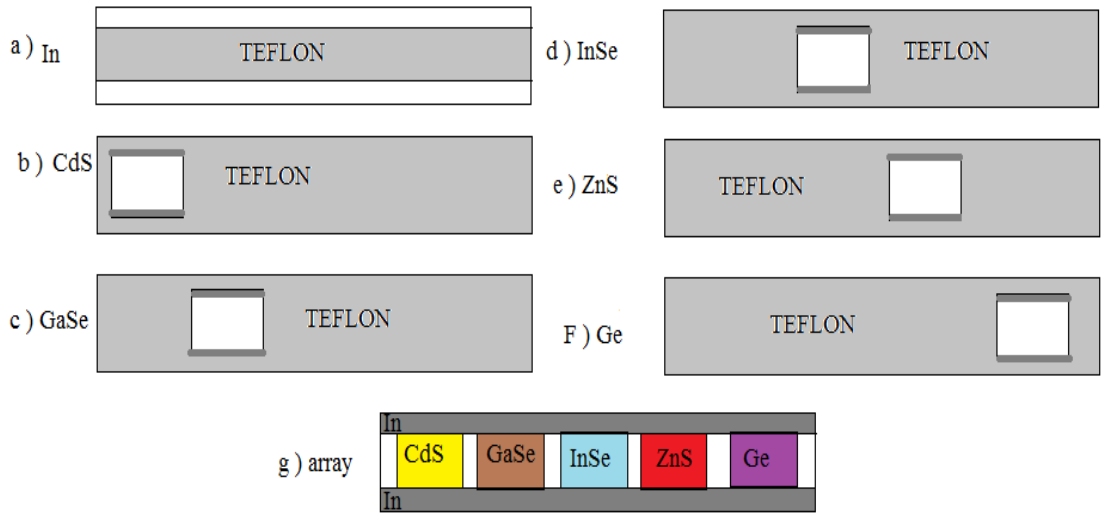

Fig. 3.2: The geometrical design of the TEFLON covered glass substrate and photoconductor array.

3.2 Optical measurements

The optical transmittance and reflectance are measured in the incident light wavelength range of 300 to 1100 nm by means of a Thermo Scientific Evolution 300 UV-VIS-NIR spectrophotometer that is equipped with VeeMax II spectrophotometer as shown in figure 3.3. The reflectance of all samples is measured at normal incidence at an angle of 15°.

The Thermo Scientific Evolution 300 UV-VIS-NIR spectrophotometer includes an extended wavelength range from the UV to the near-IR silicon photodiode detectors. The data were collected and manipulated by means of the VISION software. The transmittance and reflectance measurements were used to determine the optical band gap and materials absorbability.

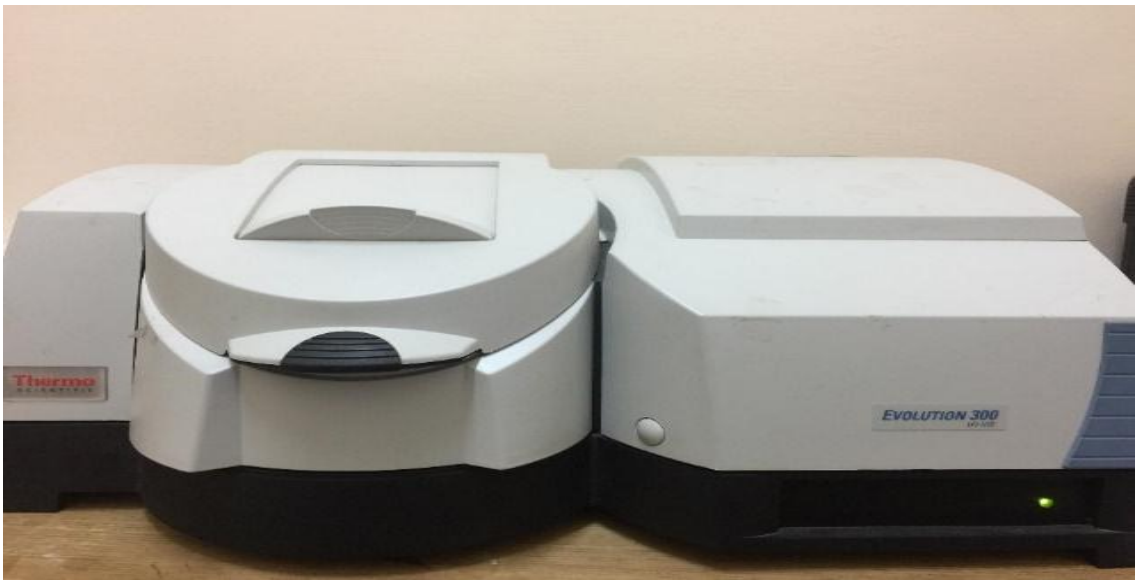

Fig. 3.3: Thermo Scientific Evolution 300 UV-VIS-NIR spectrophotometer.

3.3 Current-Voltage Measurements

The current voltage (I-V) characteristics are measured by connecting the samples between two Indium contacts using programmable Keithley 6485 picoammeter and Keithley 230 voltage source as shown in figures 3.4 and 3.5. measurement were carried out in the dark and under irradiation of tungsten, 406 nm, 632 nm and 850 nm lasers. The 6485 Picoammeter has high sensitivity to measure currents less than 0.1 μA. Even at higher currents, the device gives accurate current measurements. It measures voltage and resistance. The data were measured by using Keithley high-quality low-noise coaxial cables to reduce external effects. The I-V curves show the relationship between the current flowing through a photoconductor device and the applied voltage across its terminals. The curves introduce an Ohmic device. All the measurements were carried out at room temperature and standard pressure.

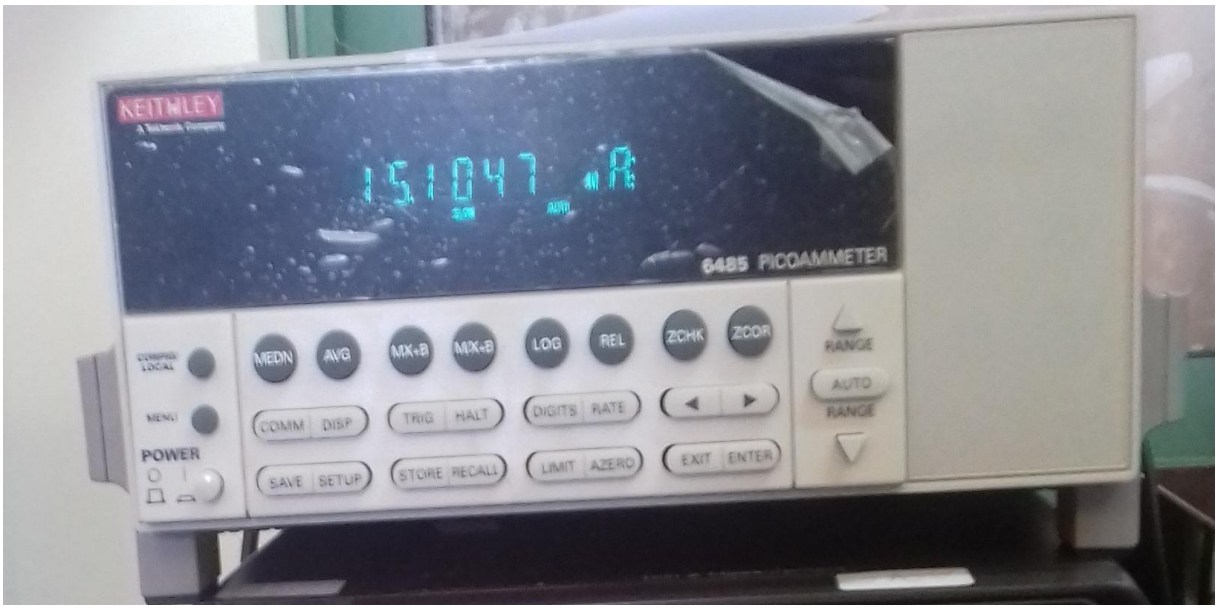

Fig. 3.4: Keithley 6485 pico-ammeter

Fig. 3.5: Keithley 230 voltage source

Chapter Four
Results and Discussion

4.1: Optical properties and energy band gaps

In order to determine the optical properties and energy band gaps for photoconductor array materials, the transmission (*T*), reflection (*R*) and absorption(*A*) measurements are measured by using (Evolution™ 300 UV-Vis Spectrophotometer).

The optical properties (*T*, *R* and *A*) are studied as a function of wavelength (λ) for Cadmium Sulfide(CdS), Gallium Selenide(GaSe), Zinc Sulfide (ZnS), Indium Selenide (InSe), Germanium (Ge) and InSe/CdS heterojunction.

Figure 4.1 shows Optical transmission spectra of photoconductor array materials. We found that *T* for CdS increases slowly as λ increases up to *T*=16% which is observed at λ= 450 nm. Beyond λ=450 nm, *T* increases rabidly and it reach's a maximum value of *T*= 93.1% at λ= 600 nm. For λ larger than 600 nm, *T* starts to decrease and it reachs a minimum value of *T*= 64.5% as shown in figure 4.1. Our results agree with Ikhmayies *et al* [137] .

T for InSe/CdS heterojunction behaves as that of CdS, but it reaches the max value of *T*= 94.1% at λ= 762 nm. For λ larger than 762 nm, it starts to decrease slowly and it reachs a minimum value of *T*= 60.2% as shown in the figure 4.1. *T* for InSe increases slowly as λ increases up to *T*= 33.1% at λ= 584 nm. After 584 nm *T* increases rabidly to reach a maximum value of *T*= 89.1% at λ 774 nm.

For wavelength larger than 774 nm *T* decreases slowly to reach a minimum value of *T* = 65.5% as shown in figure 4.1.

Similar behavior of transmittance for GaSe and ZnS, *T* increases rapidly from λ= 438 nm up to λ= 538 nm. At λ= 538 nm, *T*= 38.3% for GaSe and *T*= 32.6 % for ZnS. Beyond λ= 538, *T* increases slowly to reach a maximum value of *T*= 89.2% at λ= 742 nm for GaSe and *T*= 90.6% at λ= 804 nm for ZnS, as shown in figure 4.1.

T for Ge increases slowly from λ= 602 nm up to λ= 928 nm and *T*= 26.8% at λ= 928 nm. Beyond λ= 928 nm, *T* increases rabidly to reach a maximum value of *T*= 66.8% at λ= 1094 nm as shown in figurer 4.1.

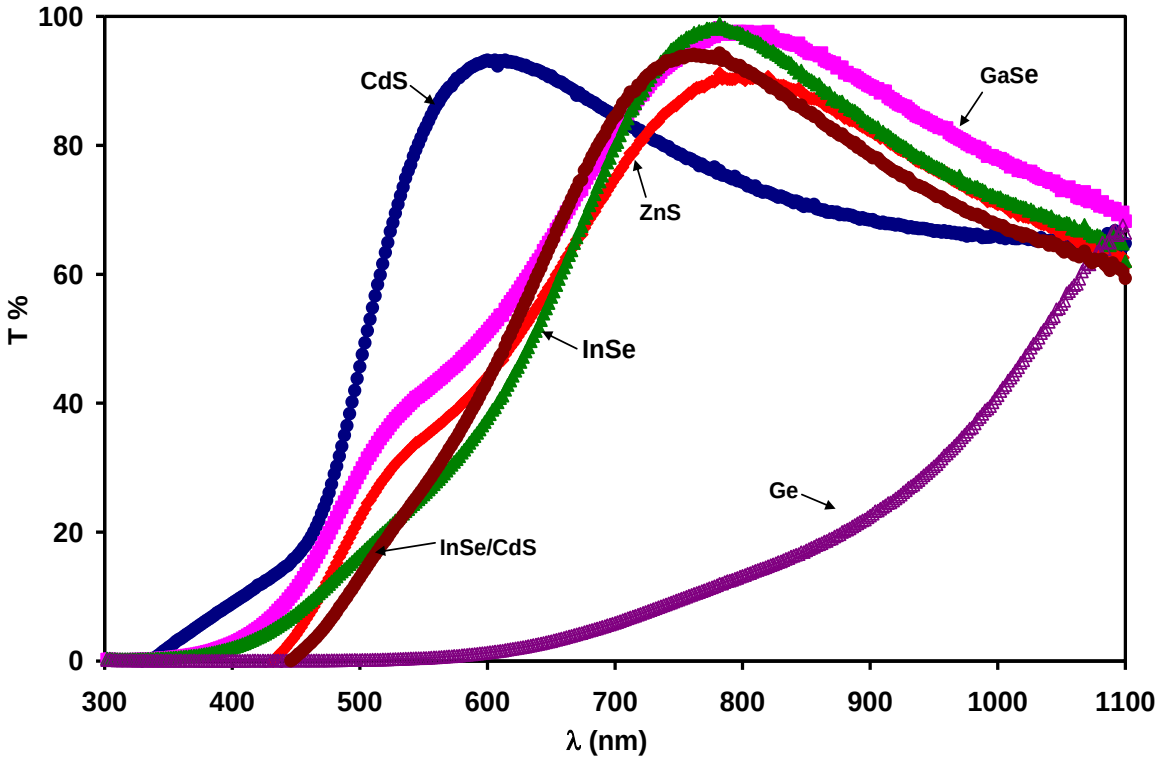

Fig. 4.1: Optical transmission spectra of photoconductor array materials.

Figurer 4.2 shows optical reflection spectra of photoconductor array materials. *R* for CdS has one maximum peak of *R*= 18.2% at λ= 492 nm. Also it has one minimum peak of *R*= 5.16% at λ= 600 nm. *R* for InSe and GaSe has similar response for incidence wavelength λ. InSe and GaSe have two maximum peaks of R=28.6% and 29.8% at λ= 586 nm and λ= 1080 nm, respectively, are observed for InSe. The maximum reflectance R= 26.5% and *R*= 21.9% at λ= 604 nm and at λ= 1096 nm, respectively, are observed for GaSe. The two minimum peaks are *R*= 17.1% and *R*= 5.41% at λ= 480 nm λ= 788 nm, respectively nm for InSe. Similarly two minimum peaks for GaSe *R*= 9.9% and *R*= 4.17% at λ= 494 nm and λ= 820 nm, respectively. As shown in figure 4.2. *R* of InSe/CdS heterojunction shows clearly that it has two maximum peaks which are lower than maximum peaks of InSe and larger than CdS. We found that *R* = 19.6% at two different wavelength λ= 550 nm and λ= 1088 nm. While the minimum peaks are lower than that of InSe and CdS. The first minimum peaks *R*= 8% at λ= 342 nm and the second one was 1.4% at λ= 750 nm, as shown in figure 4.2.

In our study for Ge, we indicated that R has one maximum peak of *R*= 30.3% at λ= 876 nm, but Ge has two minimum peaks of *R*= 22.01% at λ= 668 nm and *R*= 11.1% at λ= 1096 nm as shown in figure 4.2.

Finally, ZnS has two maximum peaks *R*= 20.7% at λ= 426 nm and the *R*= 20.07% at λ= 1076 nm. Also ZnS has two minimum peaks *R*= 6.13% at λ= 356 nm and *R*= 5.25% at λ= 606 nm as shown in figure 4.2**.**

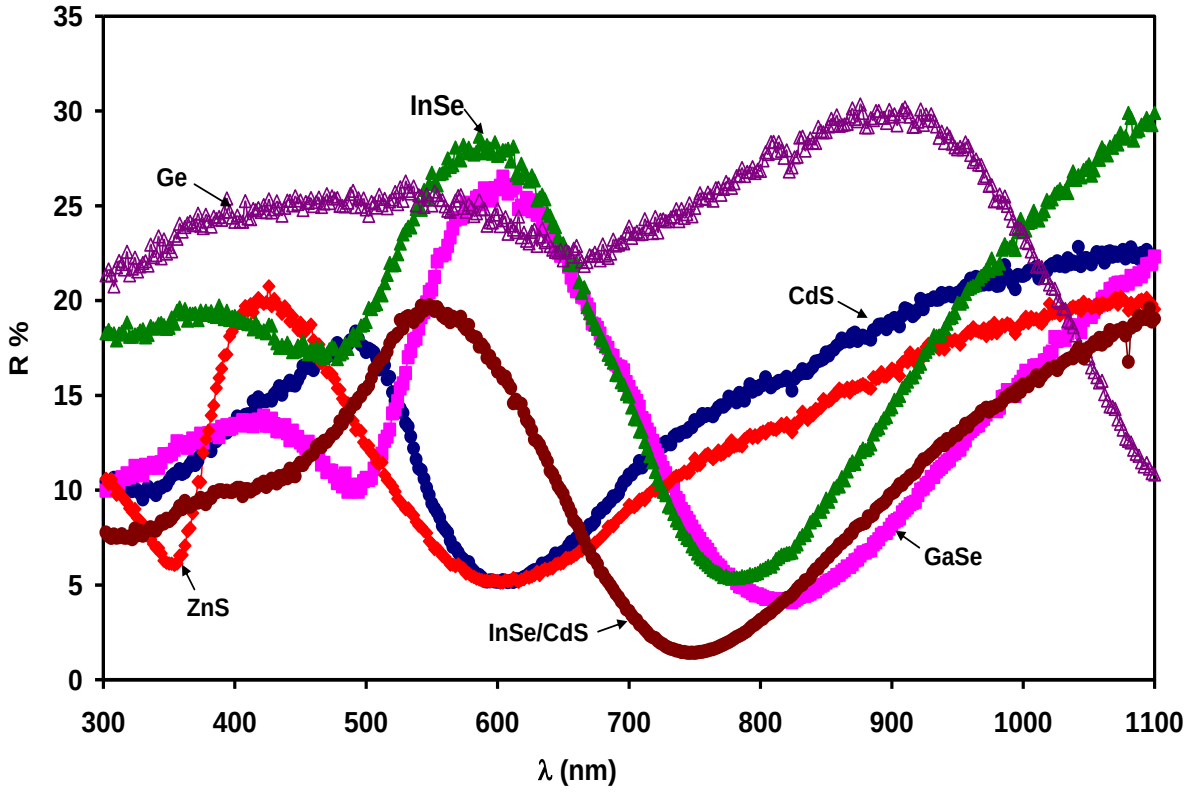

Fig. 4.2: Optical Reflection spectra of photoconductor array materials.

Analysis of optical absorption is a productive tool for finding the energy band gap. *T* and *R* spectra were recorded in the photon energy (*E*= *hv*) range of 1.0-4.5 eV. From these spectral data the absorption coefficient (α) calculated by using the relation [138]:

$$T= (1-R)^2 \exp(-\alpha d) \qquad (4.1)$$

Where *d* is the film thickness. The data are illustrated in Figurer 4.3. It is clear that the absorption coefficient α of CdS thin films sharply increases with increasing photon energy in the region of 2.22-2.67 eV. The value of α increases from 0.59×10^3 to 6.3×10^3 cm^{-1} in

the region of $2.22 \leq E \leq 2.67$ eV and then slightly continues increasing until it reaches a value of 9.3×10^3 cm^{-1} at E= 3.98 eV.

We found that α for InSe and InSe/CdS heterojunction thin films increases with increasing photon energy in the region of 2.00-2.70 eV. The value of α increases sharply from 3.96×10^3 to 8.35×10^3 cm^{-1} for InSe in the region of $2.00 \leq E \leq 2.70$ eV. Also, α sharply increases from 3.24×10^3 to 8.41×10^3in the region of $2.00 \leq E \leq 2.70$ eV for InSe/CdS heterojunction. Beyond E= 2.70 eV, α starts a slight increase until it reaches a maximum value of $\alpha= 9.04\times10^3$ cm^{-1} for InSe and $\alpha= 9.91\times10^3$ cm^{-1} for InSe/CdS heterojunction at the same value of E= 3.98 eV as shown in figure 4.3.

From figure 4.3 we recognized that α of Ge thin film sharply increases with increasing photon energy from 3.22×10^3 cm^{-1} to 8.23×10^3 cm^{-1} in the region of $1.12 \leq E \leq 1.83$ eV. Beyond E= 1.83eV, α increases slightly until it reaches a value of $\alpha= 8.67\times10^3$ cm^{-1} at E= 3.98 eV.

From figure 4.3 it is clear that α of GaSe sharply increases with increasing photon energy α increases from 1.37×10^3 to 7.35×10^3 cm^{-1} in the region of $1.80 \leq E \leq 2.53$ eV. Beyond E = 2.53 eV, α continues increasing until it reaches a value of 8.53×10^3 cm^{-1} at E= 2.75 eV. But, beyond the value of E= 2.75, α increases slowly to reach a maximum value of $\alpha = 9.84\times10^3$ cm^{-1} at E= 3.98 eV. The absorption coefficient α for ZnS sharply increases with increasing photon energy. α increases from 1.92×10^3 to 7.07×10^3 cm^{-1} in the region of $3.32 \leq E \leq 3.72$ eV as shown in figure 4.3.

.

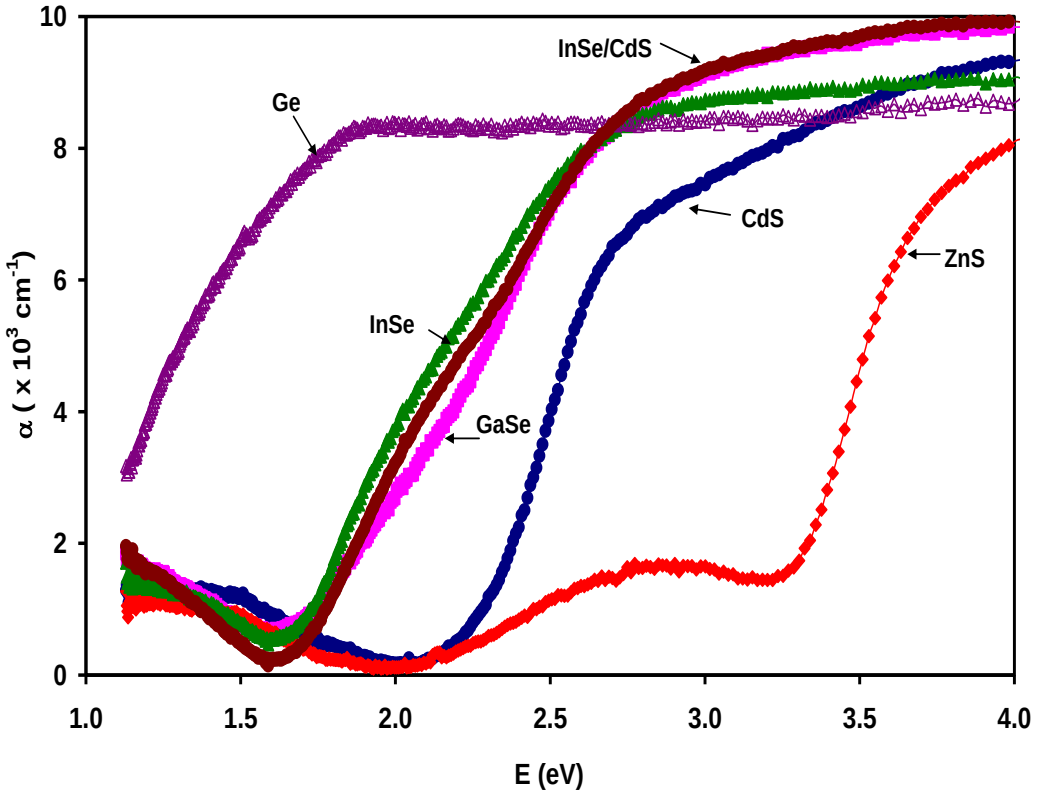

Fig. 4.3: Variation of absorption coefficient as function of incident photon energy.

The energy band gap (E_g) can be calculated from Tauc plot of $(\alpha h\nu)^2$ *versus* ($h\nu$) [139]

$$\alpha h \nu = C(h \nu - Eg)^{1/2} , \qquad (4.2)$$

Where α is the absorption coefficient, $h\nu$ is the photon energy in (eV), E_g is the direct band gap energy, and C is a constant that depends on the transtion probability. Figure 4.4 shows the Tauc plots. The energy band gaps were determined from the extrapolation as indicated by the dotted lines in figure 4.4, and the results are listed in (table 4.1). E_g= 2.39 eV for CdS, which agrees with Ikhmayiesa *et al* where they found that the energy band gap for CdS equals 2.40 eV [140]. Also the energy band gap for GaSe E_g= 2.15 eV, this value is close to that estimated by Qasrawi as E_g= 1.96 eV [141]. The energy band gap for ZnS

being E_g= 3.33 eV agrees with that obtained by Hwang which is equal 3.54 eV [142]. The Eg for InSe in literature is 1.39 [143], but we found that Eg equal 2.02 eV which is due to formation In_2Se_3 with γ phases [78]. The energy band gap for Ge is 1.14 eV which is differing from previous studies [93] which is equal 0.7 eV this difference due to formation of GeO at the top surface of the film, the GeO has energy band gap of 1.2 eV [94]. For InSe/CdS heterojunction Eg= 2.10 eV. All results are listed in table 4.1.

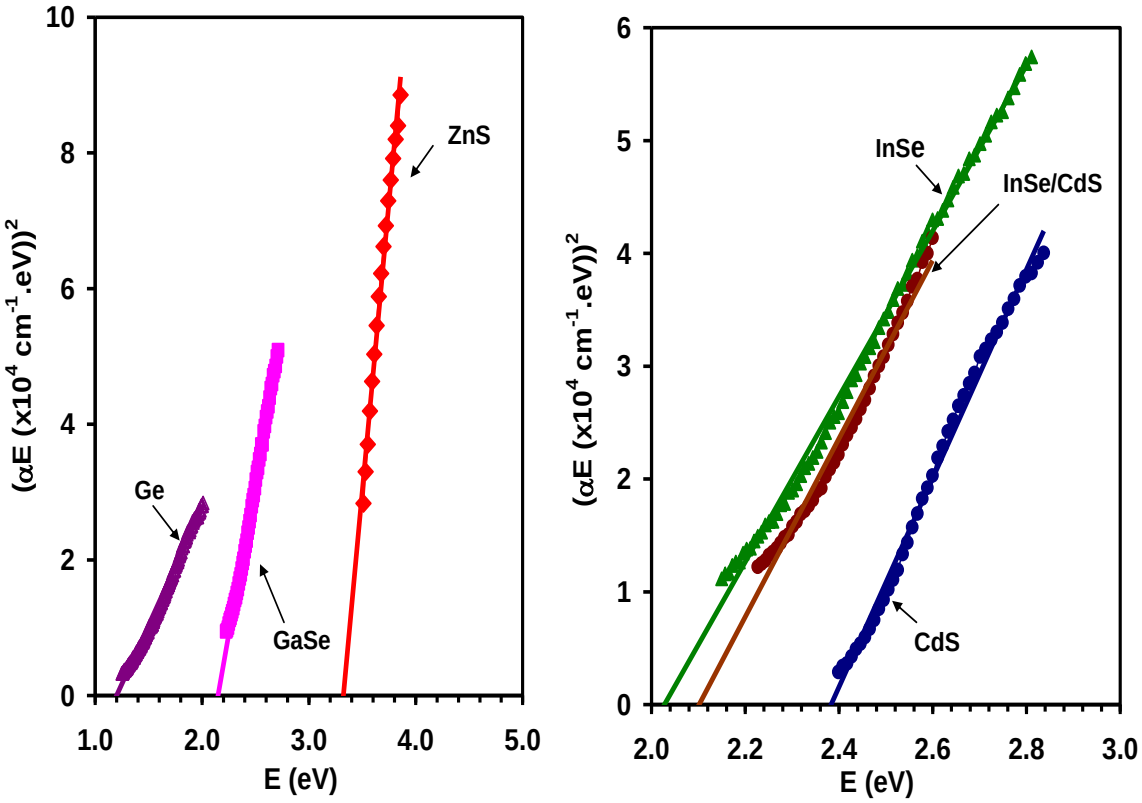

Fig. 4.4: Plot of $(\alpha h\upsilon)^2$ vs. E of photoconductor array materials for (a) GaSe, ZnS and Ge and (b) CdS, InSe and InSe/CdS

Table 4. 1: Optical properties and energy band gaps for photoconductor array materials

material types	**E_g** (eV)	**Area (cm^2)**	**Max T/ λ (nm)**	**Max R/ λ (nm)**	**Eg reference**	**Rejoin of strong absorption (eV)**
CdS	2.39	1.4	93.1%/600	18.2%/492	2.40	2.22- 2.67
GaSe	2.15	0.6	89.2%/742	26.5%/604	1.96	1.80-2.53
ZnS	3.33	1.2	90.6%/804	20.7%/426	3.54	3.30-3.72
InSe	2.02	0.48	89.1%/774	28.6%/586	2.0	2.00 -2.70
Ge	1.14	1.1	66.6%/1090	30.3%/876	1.2	1.12 -1.83
InSe/CdS	2.10	0.39	94.1%/ 762	19.6%/550		2.00 -2.70

The tabled data of energy band gaps indicate information about the operating region of the proposed photoconductor. the proposed device is supposed to operate in the incident photon energy range of 1.14 -3.33 eV .This wide range extend from the blue limit to the near IR and make the photoconductor suitable for many optoelectronic application like IR detection , photovoltaic application and visible light communication. Receives in visible light communication get use from room lighting and from lasers of wave lengths of 406, 632 and 850 nm.

4.2: Photoelectric properties

In this work, we designed a photoconductor array, consisting of materials with energy band gaps ranging from 1.14 to 3.33 eV. First, we studied these materials separately to find their photoelectrical properties. After that we studied them as one material serially connected photoconductor array to recognize the best construction for our photoconductor.

4.2.1 Photoelectric properties of CdS

The I-V characteristics of the CdS measured in the dark and under tungsten light in the range of irradiation power of 1.0-12.0 W. It is also measured under 406-nm (0.5-6.0 mW) and 632 nm (1mW) lasers. In n- types semiconductors , the metal work function (ϕ_m) is required to be lower than the semiconductor work function (ϕ_s) to obtain Ohmic contact for Indium metal which has a work function of 4.09 eV that is less than the CdS work function (4.7eV) [144]. From figure 4.5 it is clear that the current recorded in the dark and under light illumination increase linearly with increases voltage investigated that In/CdS/In is an ohmic contact. Although material maybe ohmic in the dark it dose not necessarily means that it should be ohmic under light because that only depends on the generation recombination rates.

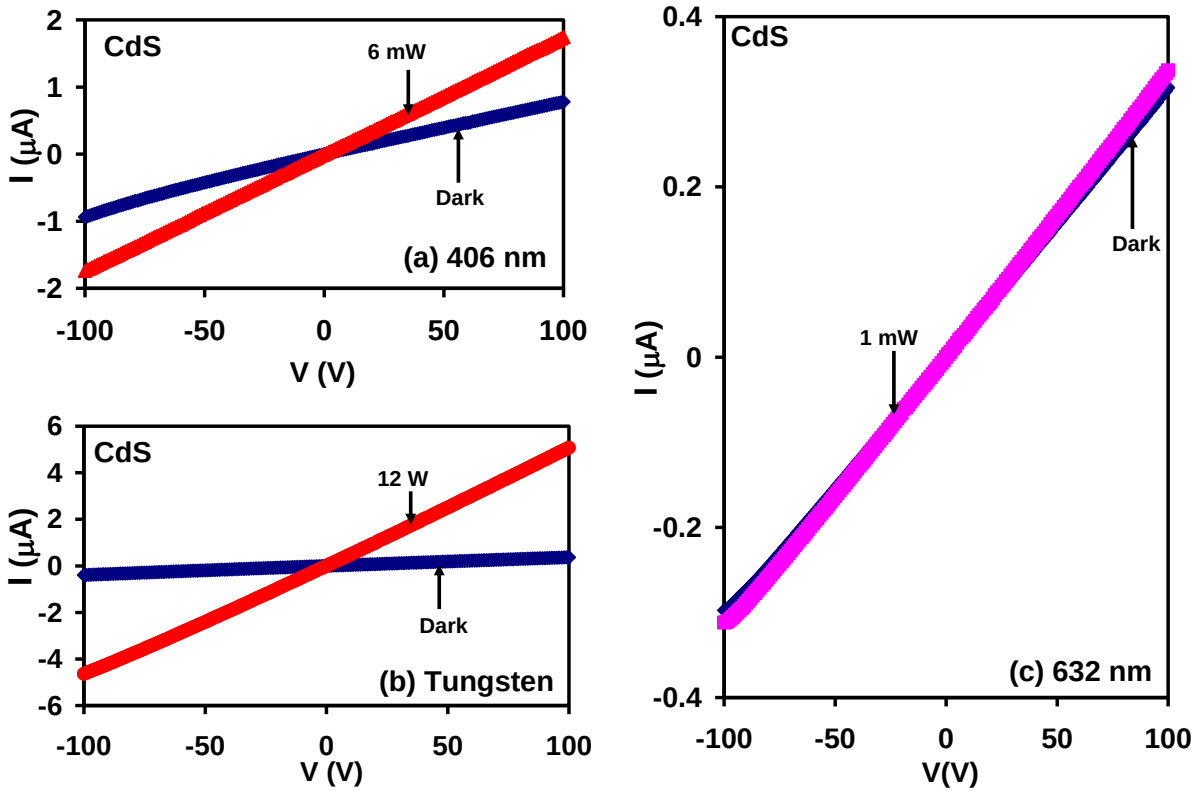

Fig. 4.5: Dark and light current I-V characteristics of CdS for (a) 406-nm laser, (b) tungsten and (c) 632 nm laser

In/CdS/In is illuminated with tungsten, 406 nm and 632 nm lasers under voltage bias ranges in range of (-100 to +100 Volt). When In/CdS/In is exited, the generated photocurrent changes because of the effect of the applied electric field which leds to a photocurrent that are added to the dark current, which effectively increases the conductivity [145]. As shown in figure 4.5 (a) the current under light is larger than the dark current meaning that CdS id photo sensitive to light irradiation. This behavior appears because the photon energy of 406 nm laser is larger than the energy gap of CdS leading to electron-hole pairs generated from valance band to conduction band which increases the current. The generated e-h pairs are

separated by the applied electric filed, thus the e`s move to the conduction band and recombine with holes in the valance band [143]. Also, the light current for tungsten and 632 nm laser is larger than the dark current although their energy photons are smaller than the energy gap of CdS this is possibly due to transition of carriers from defect states in the band gap to the conduction band [146]. The extrinsic absorption is dominated by transitions from the valence band to inter bands or impurity states that are formed by defects, inhomogeneities and un purposely present dopants[147] . The generated photocurrent ($I_{ph} = I_L - I_d$) increases with power for lasers and tungsten in voltage biasing rang (-100 to +100 volt) as shown in figure 4.6(a)-(c). The maximum value of photocurrent is obtained for tungsten with photocurrent of 4.705 μA at a power of 12 W. Also, the generated photocurrent for 406 nm laser is the highest compared to 632 nm laser as shown in figure 4.6(b)-(c).The reason for increasing photocurrent with increasing the incident power because stronger light-matter interaction will take place in In/CdS/In [148]. As the absorption is intrinsic (photon energy for 406 nm is larger than Eg) increasing the light power indicates an increase in the incident photon energy which is quantized. Since the energy of photon is kept constant, then tee power have means increasing the number of incident photon. In accordance to Einstein theory each photon must pick up an e causing the sharp increase in photocurrent [149].

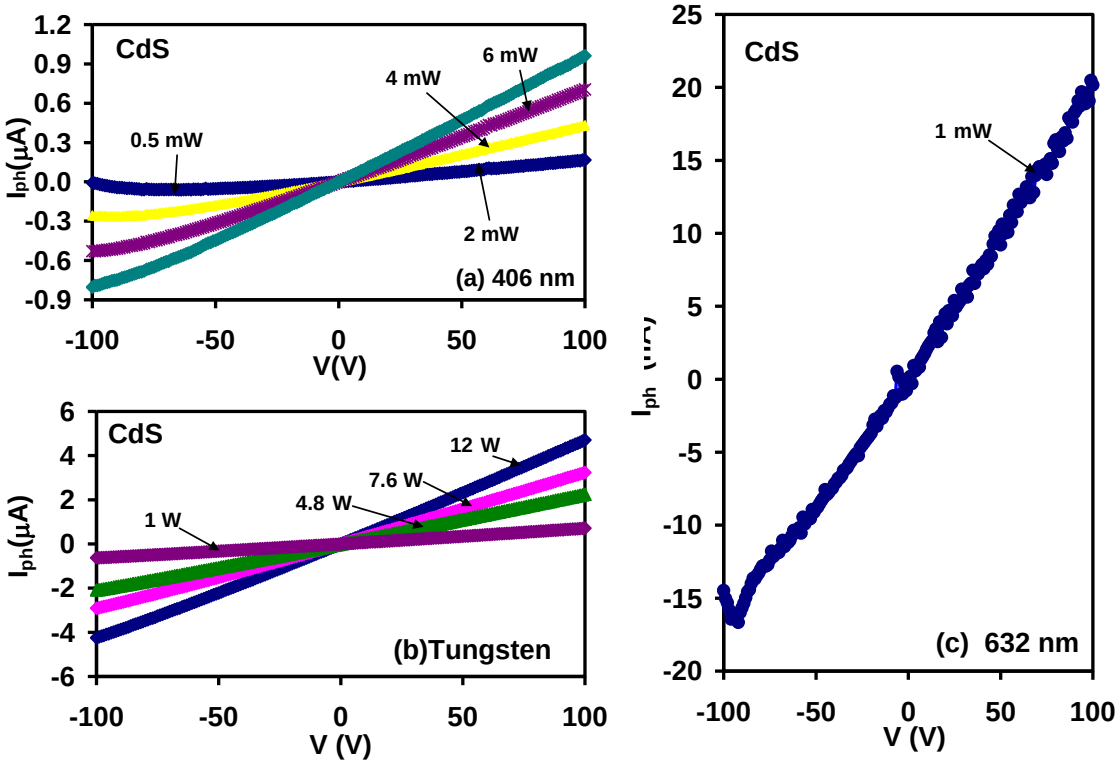

Fig. 4.6: photocurrent I-V characteristics of CdS for (a) 406-nm laser, (b) tungsten and (c) 632 nm laser.

Figure 4.7 shows the photoresponsivity (R) of the In/CdS/In which is calculated by using the following equation [133, 150]:

$$R_S = \frac{I_{Ph}}{PA} \quad , \qquad (4.3)$$

Where I_{ph} is the photocurrent, A is the illuminated area and P is the incident light intensity. Figure 4.7 shows a plot of R_S versus power (at a bias voltage at 100 V) for In/CdS/In prepared under 406 nm and 632 nm lasers and tungsten.

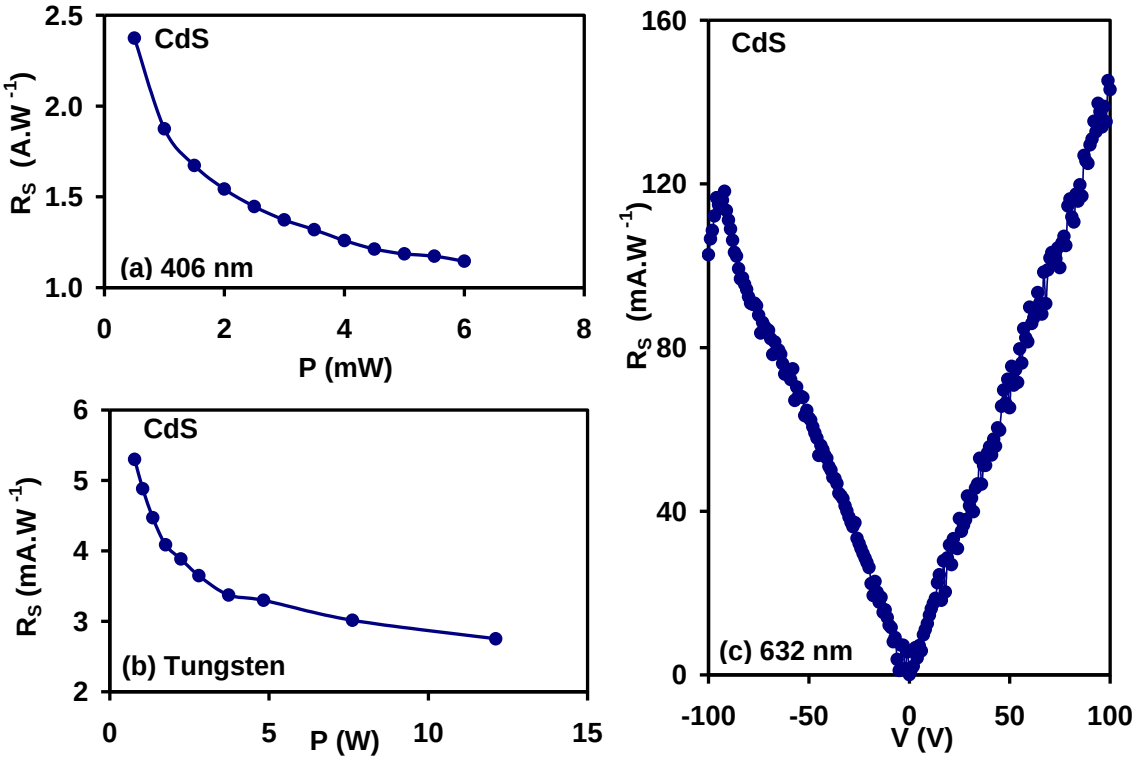

Fig. 4.7: The photoresponsivity (R_S) characteristics of CdS for (a) 406-nm laser, (b) tungsten and (c) 632 nm laser.

The photoresponsivity (R_S) decreases with increases the power of 406 nm laser and tungsten as shown in figure 4.7(a), (b) while *Rs* is increasing with increasing voltage as shown in figure 4.7(c) for 632 nm laser at power of 1 mW. The decrease in photoresponsivity with increased power of 406 nm laser and tungsten could be attributed to filling of the long-lived trap states at higher powers [151, 152] also, the decreasing of R_S with power is due to the increased recombination rate of photogenerated carriers [147,153]. The highest R_S value is observed at 406 nm laser at a power of 0.5 mW and it is 2.3734 A.W^{-1} as shown in figure 4.7(a). Also, it is very clear that R_S is very small values for 632 nm laser and tungsten. R_S = 143 mA.W^{-1} for 632 nm laser at a power of 1 mW power

which agrees with the results in [143]. R_S = 2.75 mA.W $^{-1}$ for tungsten at a power of 12 W. As the number of photons increases the number of generated e-h pairs increases, thus, more photons move more photocurrent and thus the responsivity is expected. However, when material contain surface traps and surface recombination centers [154] as well s deep impurity level. The dynamics of the light become highly complicated particularly, when recombination centers are empty they may be have as electron traps. Similarly do all acceptor centers. For this reason there should be demarcation levels that balance these mechanisms. The demarcation levels behave as sensitizers [155], that balance the recombination mechanism. Since the applied electric filed is very high, then most of trapping levels are saturated with increases light intensity, there is no center to actualize the recombination. This makes the recombination mechanism less effective and as a result, the material dose not sense to light.

Another important parameter is the photosensitivity (*S*). *S* of CdS thin film was determined at different powers of tungsten, 406 nm and 632 nm lasers (at applied bias voltage of 100 volt) by using the following relationship [135, 156]:

$$S = \frac{I_l - I_d}{I_d} \qquad (4.4)$$

Where I_d and I_L represent the photocurrents in the dark and under illumination, respectively. As shown in figure 4.8 (a), (b). *S* increases with increases power of tungsten and 406 nm lasers due to increases photogenerated current. The device is more sensitive to tungsten light than other lasers. At a bias voltage of 100 volts, the device was more sensitive to tungsten light, *S*= 1277% at a power of 12 W for tungsten which agrees with the results in

[143]. *S*= 21.2 % at a power of 0.5 mW for 406 nm laser. But it is seeming constant and small for 632 nm laser in the bias voltage range(-100 to +100 volt) as shown in figure 4.8 (c) because the power of 632 nm laser is constant so the number of photon that reach the device is the same although the bias voltage changing.

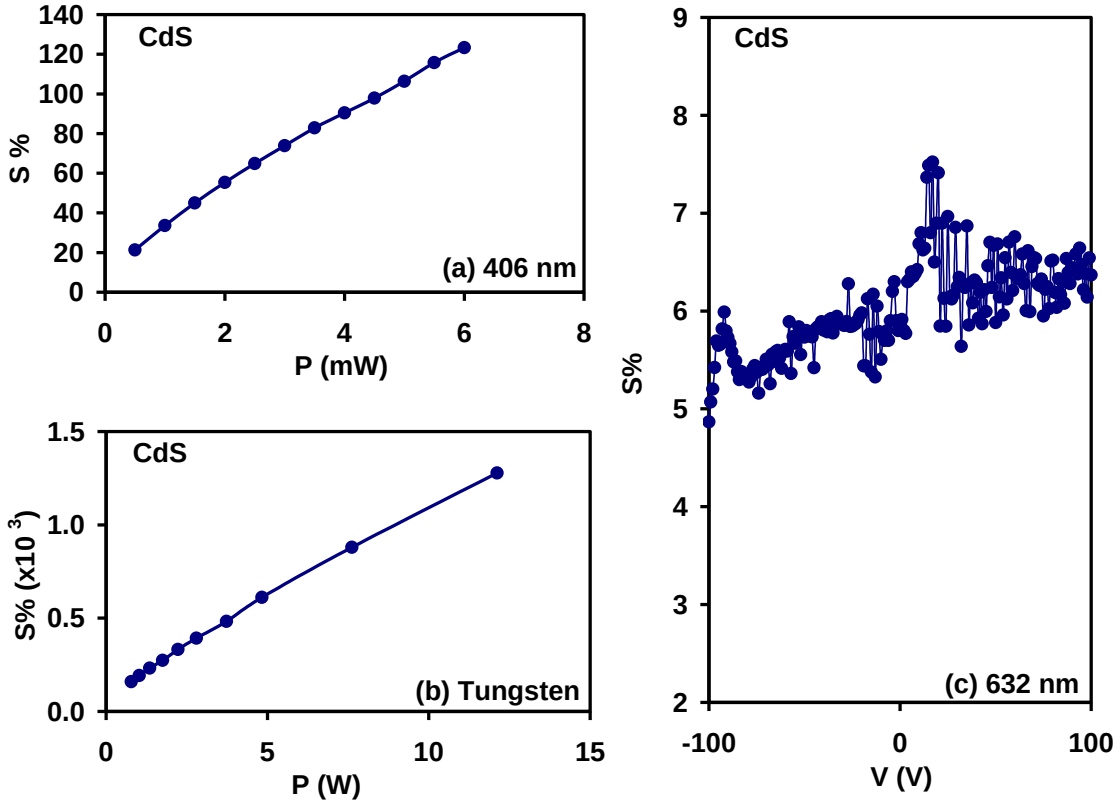

Fig. 4.8: The photosensitivity (*S*) characteristics of CdS for (a) 406-nm laser, (b) tungsten and (c) 632 nm laser.

Figure 4.9 shows the External Quantum Efficiency (EQE) for CdS (it is the number of electrons detected per incident photon). EQE can be calculated from the following equation [129, 147]:

$$EQE = \frac{R_s hc}{\lambda e}[\%], \qquad (4.5)$$

Where R_S is the photoresponsivity, h is Planck's constant, c is the speed of light, e is the electron charge and λ is the wavelength.

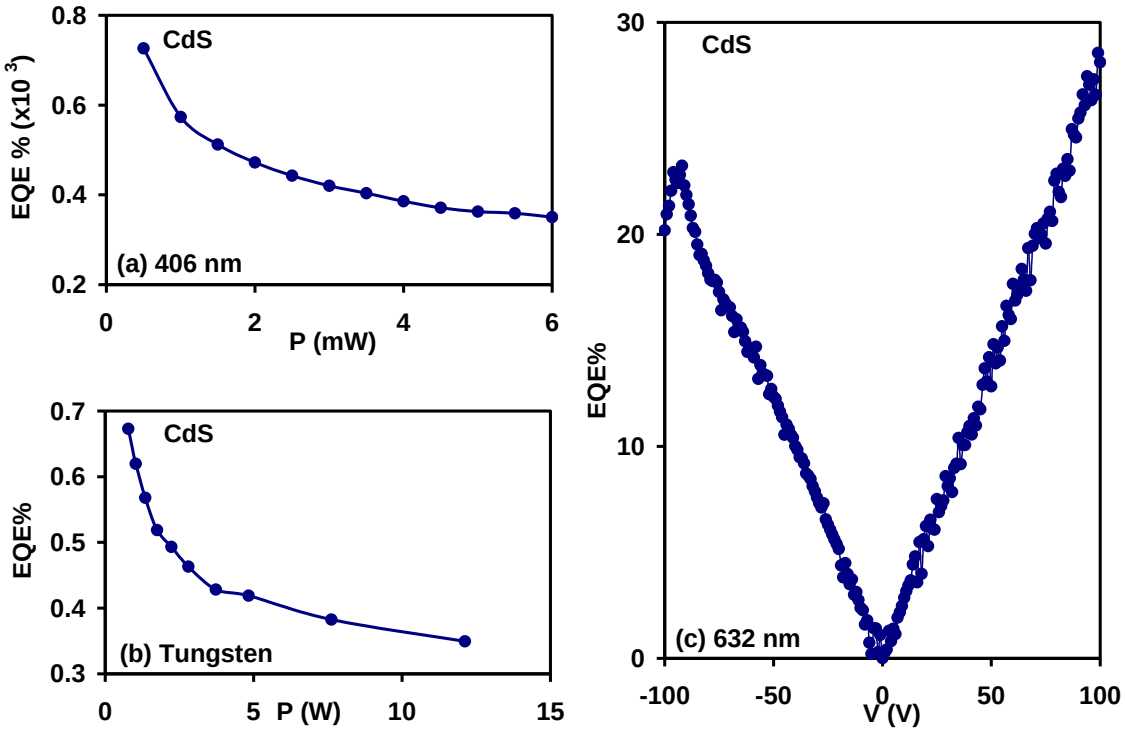

Fig. 4.9: The External Quantum Efficiency (EQE) characteristics of CdS for (a) 406-nm laser, (b) tungsten and (c) 632 nm laser.

It is clear that from figure 4.9 (a) and (b) EQE for 406 nm laser and tungsten decreases with power. While EQE for 632 nm laser increases with applied voltage at a power of 1 mW as shown in figure 4.9(c). The decreasing of EQE with power for 406 nm laser and tungsten is due to decreasing in R_S with power and due to the absorption saturation a can be seen from figure 4.3 [157]. Also, may be due to long-lived trap states and the presence of

demarcation level [153]. EQE= 726.5 % for CdS which is the maximum value for 406 nm laser at a power of 0.5 mW as shown in figure 4.9. EQE has small values for tungsten and 632 nm laser as shown in figure 4.9.

Figure 4.10 shows the internal quantum efficiency **(**IQE) It is defined as the ratio between the number of the electron-hole pairs created by the light and the number of the absorbed photons. IQE can be calculated from the following equation [129,158]:

$$IQE(\lambda) = \frac{EQE(\lambda)}{1-A}[\%], \quad (4.6)$$

Where EQE is the external quantum efficiency and *A* is the absorption.

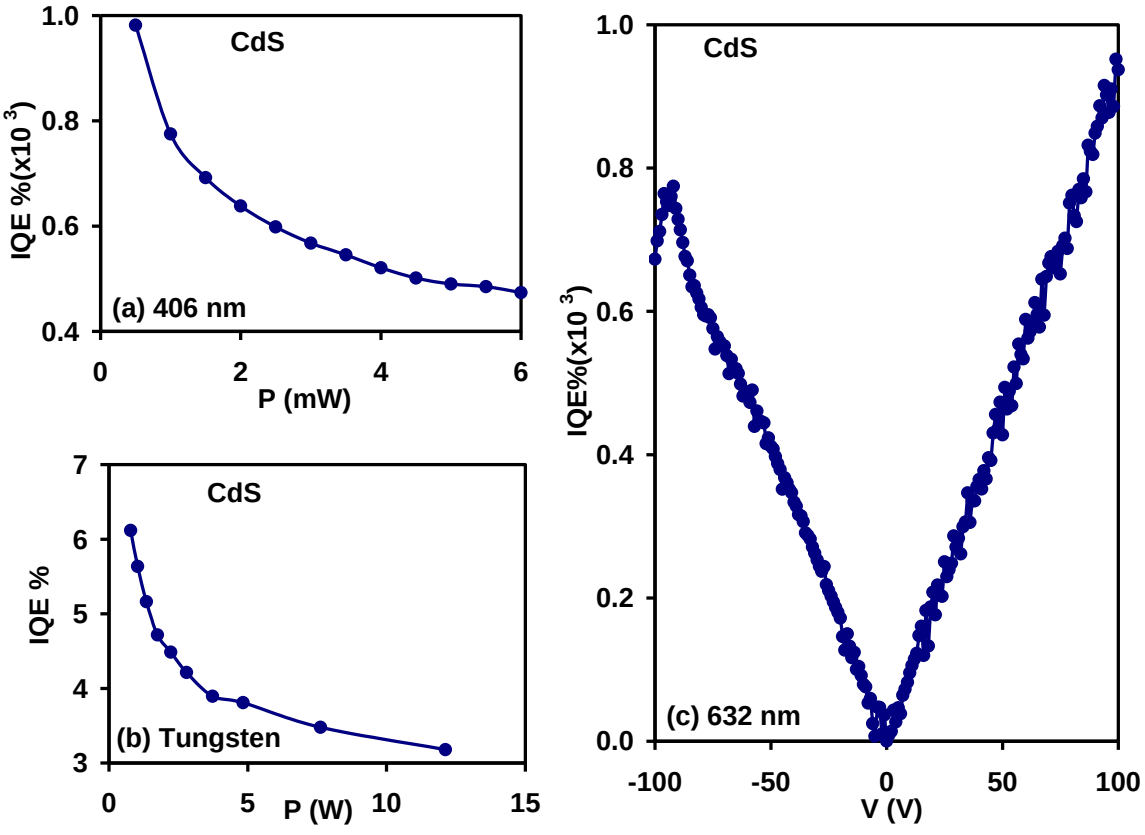

Fig. 4.10: The Internal Quantum Efficiency (IQE) characteristics of CdS for (a) 406-nm laser, (b) tungsten and (c) 632 nm laser**.**

IQE decreases with power for 406 nm laser and tungsten and IQE increases with voltage for 632 nm laser as shown in figure 4.10(a)-(c). IQE= 981.5% at a power of 0.5 mW for 406 nm laser which is the maximum value, IQE= 937% for 632 nm laser at a power of 1 mW. This is due to the large value of absorption at a wavelength of 632 nm. While IQE has very small values for tungsten. Finally all value for I_{ph}, R_S, S, EQE and IQE for In/CdS/In at different excitation of 406 nm, 632 nm lasers and tungsten are listed in table 4.2.

Table 4.2: Results for In/CdS/In for 406 nm, 632 nm lasers and tungsten excitation.

In/CdS/In	I_{ph} (nA)	S%	R_S (mA.W $^{-1}$)	EQE%	Power	IQE%
406 nm	166	21.2	2373.4	726.3	0.5 mW	981.5
tungsten	4705	1277	2.75	0.34	12 W	3.17
632 nm	20.1	6.36	143	28.1	1 mW	937.2

4.2.2 Photoelectric properties of InSe

Now we will talk about the photoelectric properties for InSe as a single device (In/InSe/In). The I-V characteristics of the InSe measured in the dark, under tungsten, 406-nm, 632 nm and 850 nm lasers. InSe is n- type semiconductor; the metal work function (ϕ_m) is required to be lower than the semiconductor work function (ϕ_s) to obtain Ohmic contact. In metal has a work function of (4.09 eV) which is less than the InSe work function (5.2 eV) [159]. As shown in figure 4.11 it is clear that the dark current increase linearly with increases voltage.

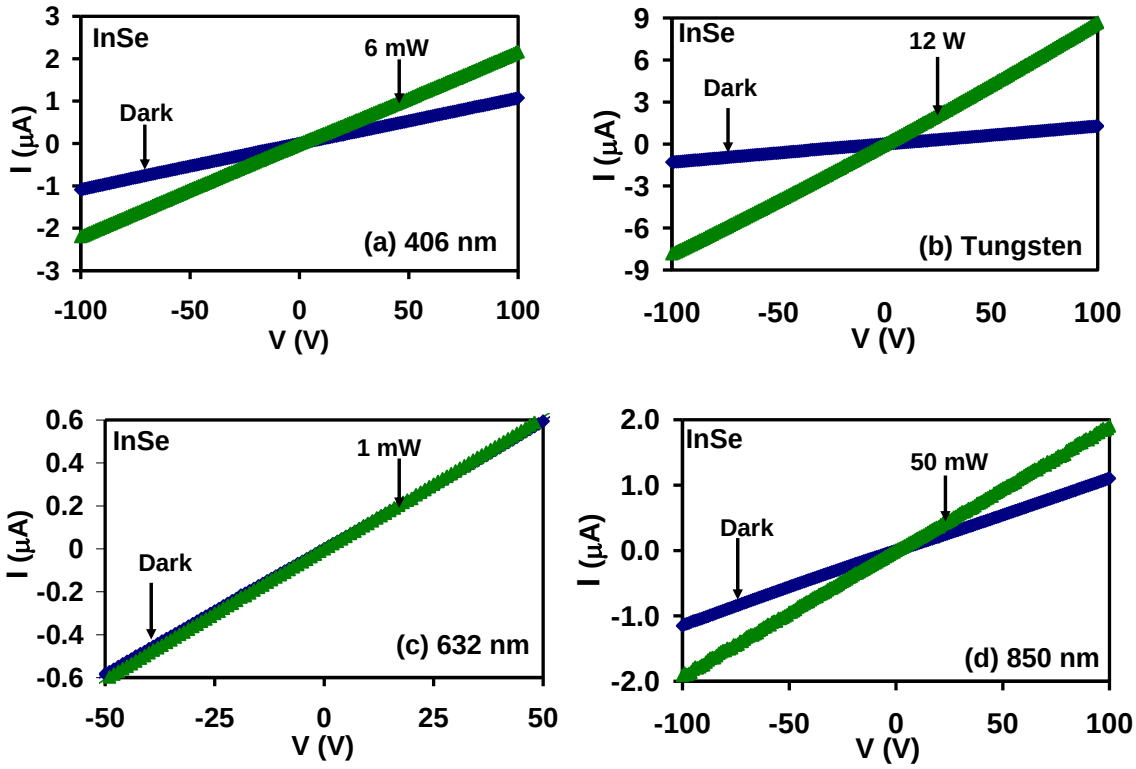

Fig. 4.11: Dark and light current I-V characteristics of InSe for (a) 406-nm laser, (b) tungsten, (c) 632 nm and (d) 850 nm lasers.

When In/InSe/In is excited with light, the generated photocurrent increases due to the effect of the light intensity which leads to a photocurrent that are added to the dark current. This effectively increases the photoconductivity [144]. As shown in figure 4.11(a) the light current is larger than the dark current because the photon energy of 406 nm laser larger than the energy gap of InSe leading to electron-hole pairs generated from valance band to conduction band which increases the current [160]. The light currents for tungsten, 850 nm and 632 nm lasers are larger than the dark current despite their energy photons is smaller than the energy gap of InSe this is may be due to transition of carriers from defect states in the band gap to the conduction band (extrinsic absorption)[145, 146]. The generated

photocurrent increases with power for lasers and tungsten in voltage biasing rang (-100 to +100 volt) as shown in figure 4.12(a)-(d) this is refers to stronger light-matter interaction will take place in In/InSe/In [147,161].

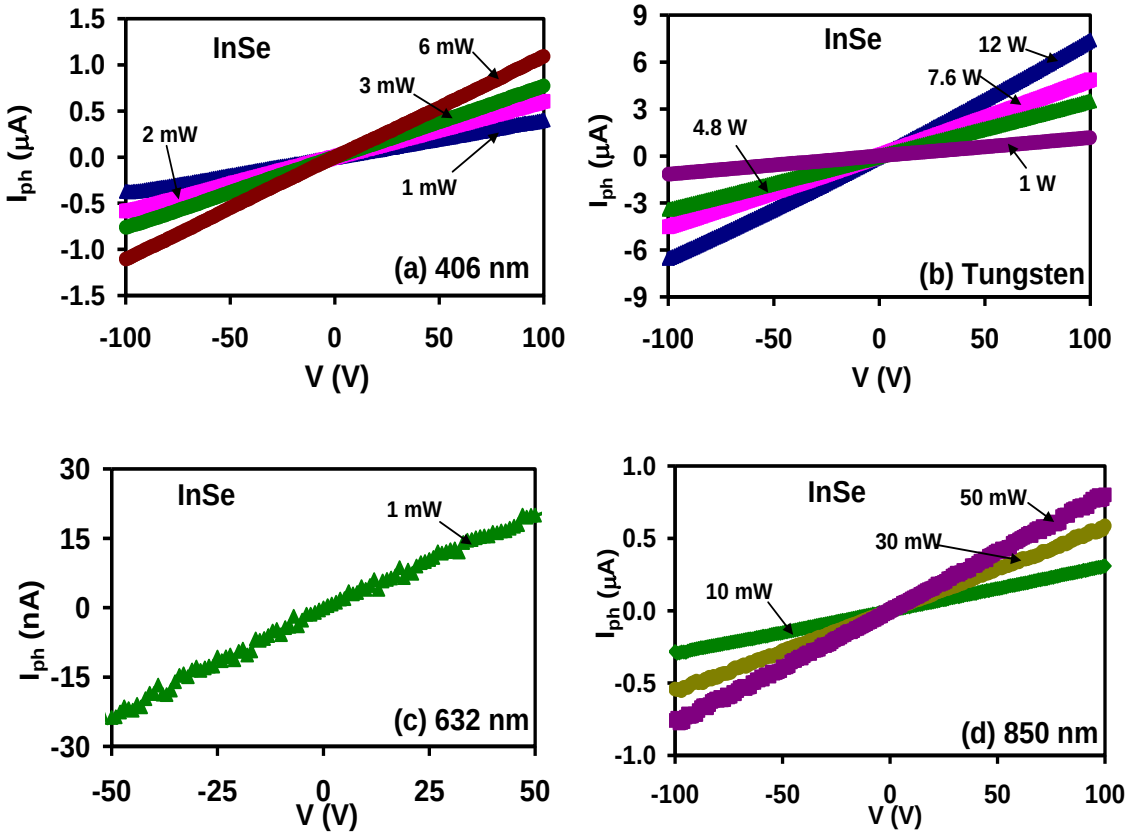

Fig. 4.12: I-V characteristics of InSe for (a) 406-nm laser, (b) tungsten, (c) 632 nm laser, and (d) 850 nm laser.

The maximum value of photocurrent is obtained for tungsten with photocurrent of 7.4 μA at a power of 12 W. Also, the generated photocurrent for 406 nm laser is the larger compared to 632 nm and 850 nm lasers as shown in figure 4.12(a), (c), and (d).

R_S decreases with power of 406 nm and 850 nm lasers and tungsten as shown in figure 4.13(a), (b), and (d). For 632 nm lasers R_S increases with voltage as shown in figure 4.13

(c). R_S decreases with power of lasers and tungsten due increased recombination rate of photogenerated carriers [147, 156] , filling of the long-lived trap states [149, 150] and due to saturation of the trap states [162] . InSe is highly response for 406 nm laser. The maximum value of R_S is 4.9 A.W $^{-1}$ at a power of 0.5 mW at 100 volt as shown in figure 4.13(a). R_S= 208.7 mA.W $^{-1}$ for 632 nm laser at 50 volts which agrees with the results in [163]. But R_S= 6.65 mA.W^{-1} it is the smaller one due to large power of tungsten.

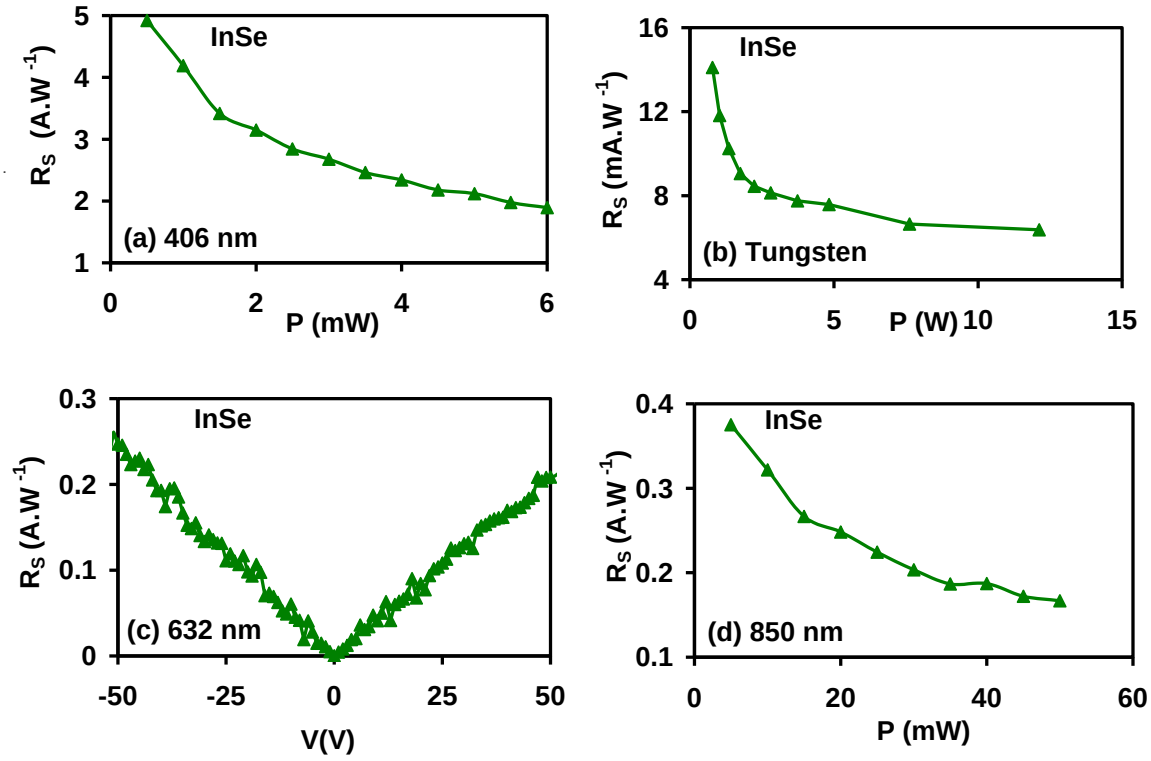

Fig. 4.13: The photoresponsivity (R_S) characteristics of InSe for (a) 406-nm laser, (b) tungsten, (c) 632 nm laser, and (d) 850 nm laser

On the other hand, the photosensitivity increases with power of 406 nm and 850 nm lasers and tungsten as shown in figure 4.14(a), (b), and (d) because of increasing the number of

generated carriers with power. While *S* is constant and small for 632 nm laser in the bias voltage range -50 to50 volts as shown in figure 4.14(c). *S* has maximum value of 577% at a power of 12 W for tungsten light. S= 21% for 406 nm laser at a power of 0.5 mW. Also, S=16 % for 850 nm laser at a power of 5 mW.

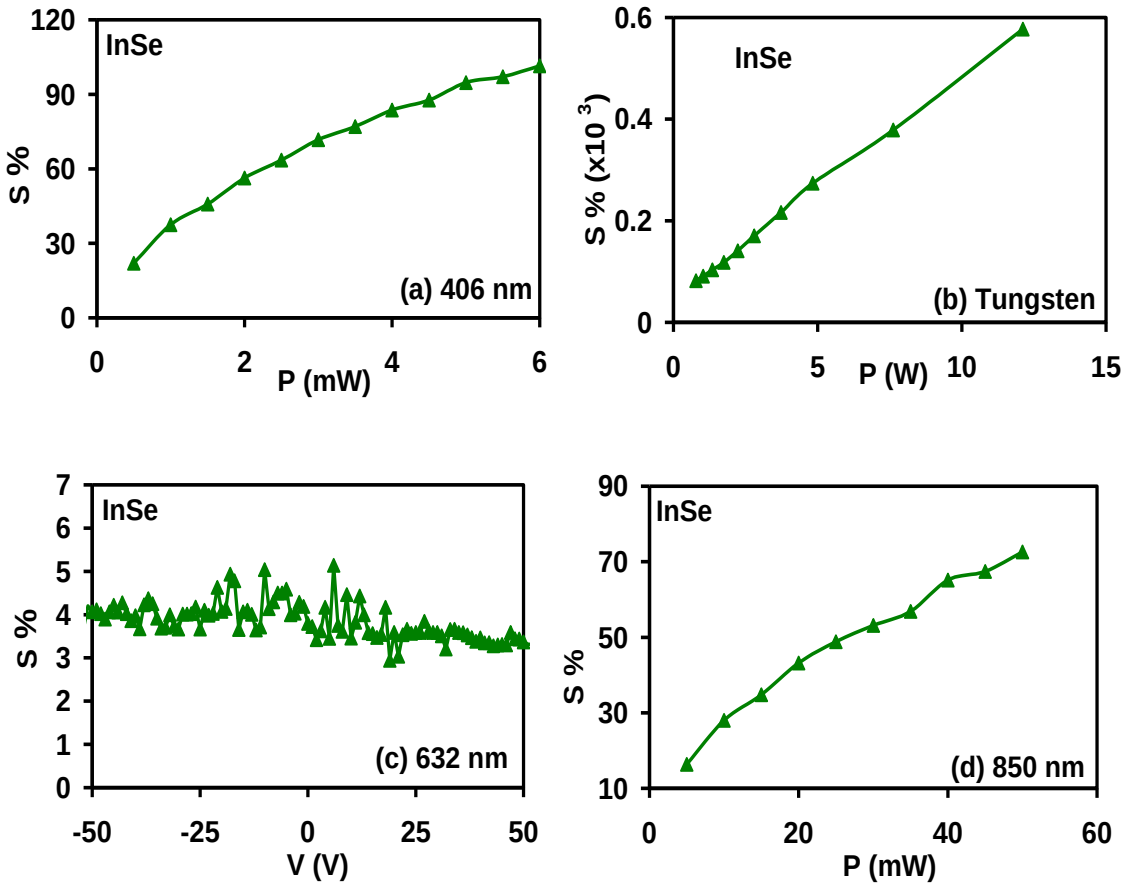

Fig. 4.14: The photosensitivity (*S*) characteristics of InSe for (a) 406-nm laser, (b) tungsten, (c) 632 nm laser and (d) 850 nm laser

The external quantum efficiency decreases with power of 406 nm, 850 nm lasers and tungsten as shown in figure 4.15(a), (b), and (d) while EQE increases with voltage for 632

nm laser at a power of 1 mW as shown in figure 4.15(c). The reducing in EQE with power for 406 nm, 850 nm lasers and tungsten maybe due to decreasing in R_S with power, absorption saturation and long-lived trap states [153]. EQE for InSe has a maximum value of 1505.7% for 406 nm laser at a power of 0.5 mW as shown in figure 4.15(a). EQE= 41.03% for 632 nm laser at a power of 1 mW and EQE = 54% for 850 nm laser at a power of 5 mW. But EQE= 0.08% for tungsten at power of 12 W.

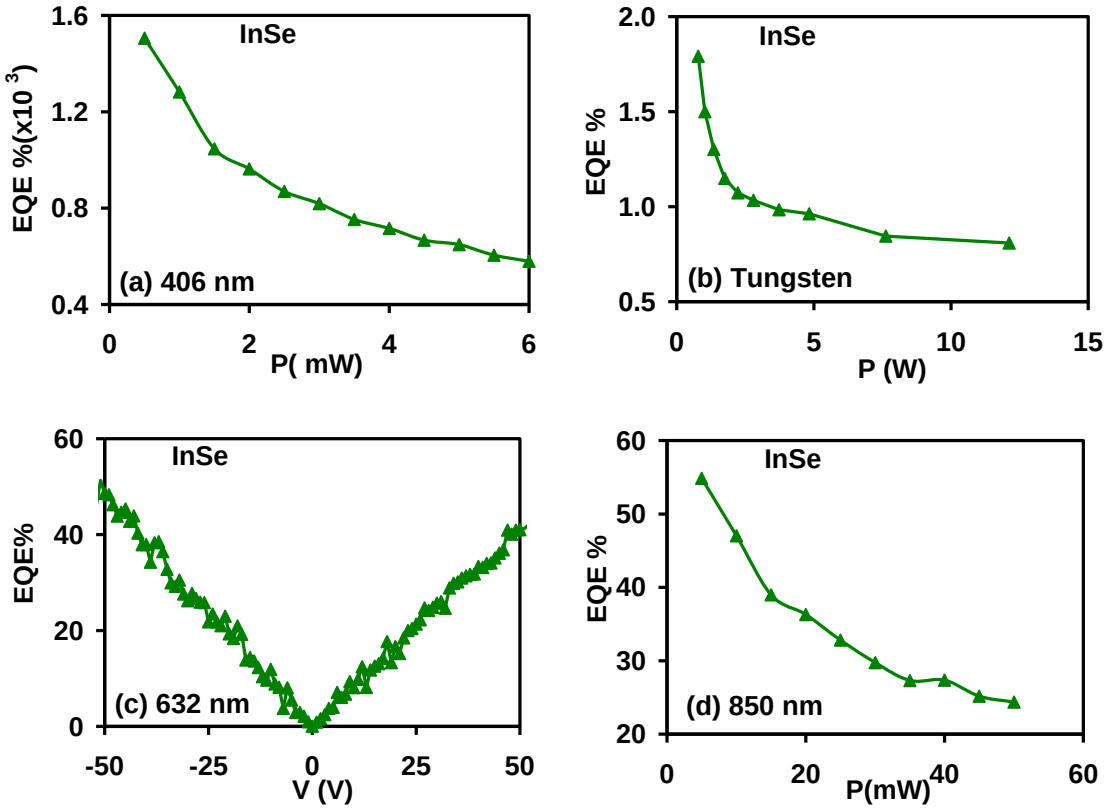

Fig.4. 15: The External Quantum Efficiency (EQE) characteristics of InSe for (a) 406 nm laser (b) tungsten (c) 632 nm laser (d) 850 nm laser

It is clear that IQE decreases with power for 406 nm, 850 nm lasers and tungsten While it is increases with voltage for 632 nm laser at a power of 1 mW as shown in figure 4.16.

Decreasing in IQE due to recombination rate decreases as the exciting power increases [164]. IQE has a maximum value of 1757% for 406 nm laser at a power of 0.5 mW as shown in figure 4.16(a). Also, IQE= 623 % for 850 nm laser at a power of 5 mW. IQE has a small value for tungsten light and 632 nm laser.

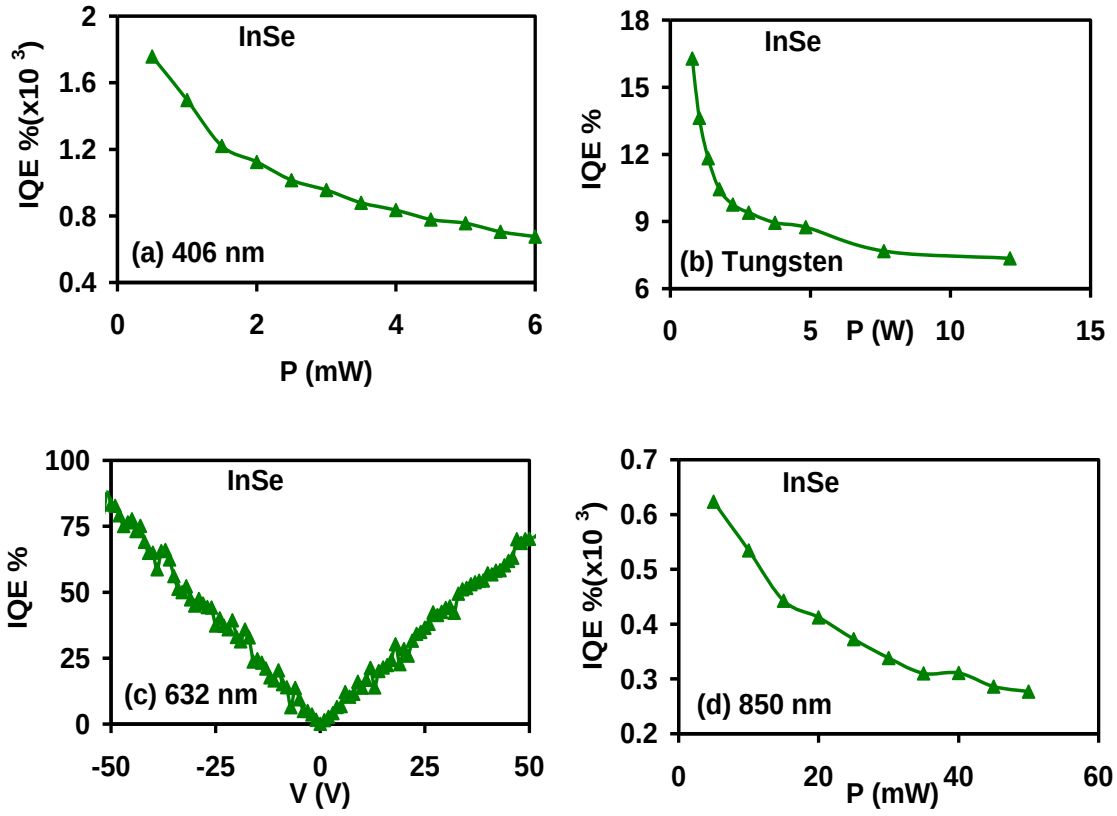

Fig. 4.16: The Internal Quantum Efficiency (IQE) characteristics of InSe for (a) 406 nm laser, (b) tungsten, (c) 632 nm laser and (d) 850 nm laser.

Finally all value for I_{ph}, R_S, S, EQE and IQE for InSe at different excitation of 406 nm, 632 nm lasers and tungsten are listed in table 4.3.

Table 4.3: Results for In/InSe/In for 406 nm, 632 nm, 850 nm lasers and tungsten excitation.

InSe	I_{ph}(nA)	S %	R_S (mA.W $^{-1}$)	EQE%	Power	IQE%
406 nm	236.1	21.9	4920	1505.7	0.5 mW	1757
tungsten	7411.4	577.1	6.65	0.08	12 W	7.35
632 nm	20.03	3.44	208.7	41.03	1 mW	70.29
850 nm	180.16	16.33	375.3	54.86	5 mW	623.4

4.2.3 Photoelectric properties of Ge

Ge is an important material that is used in our photoconductor array. In our device In/Ge/In, In metal has a work function of 4.09 eV which is less than the Ge work function 5.0 eV. So, we should not have ohmic contact [165]. The I-V characteristics of the Ge measured in the dark, under tungsten and 850 nm laser irradiation are shown in figure 4.17. The dark and under light currents increase linearly with increases voltage showing liner relation. The appearance of the ohmic character in the InGe interface is ascribed to the large separation between the two contact which cases of electron scattering leading to high resistance short ranges which is mostly controlled by the surface defects and surface roughness [166].

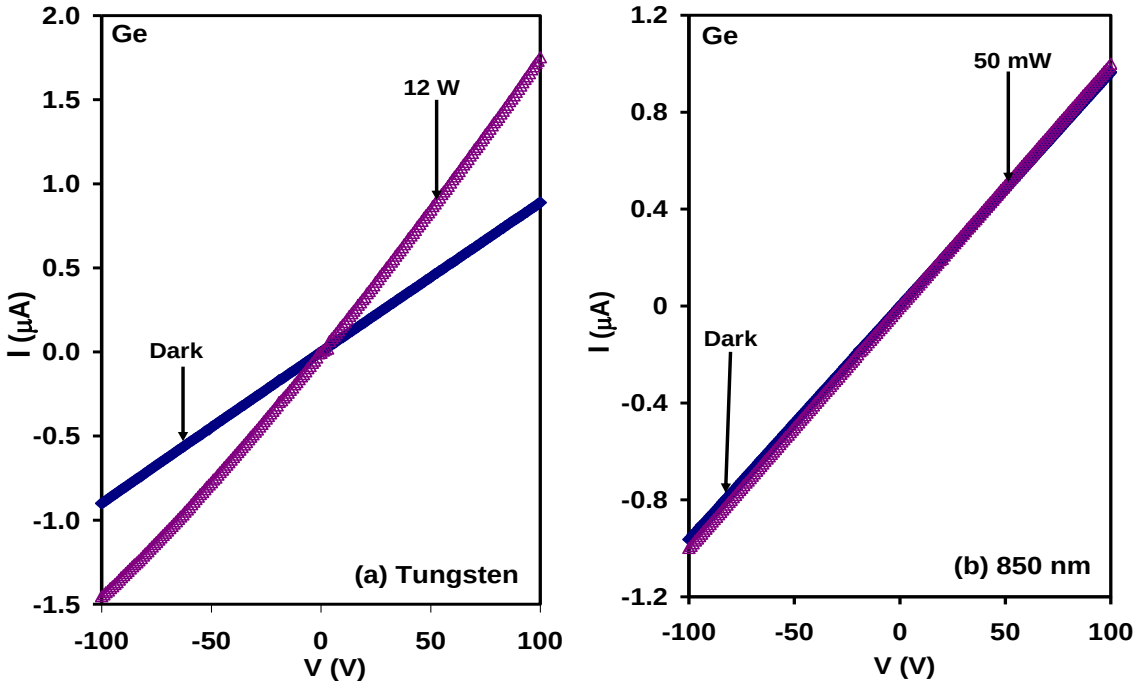

Fig. 4.17: Dark and light current I-V characteristics of Ge for (a) tungsten and (b) 850 nm laser.

When In/Ge/In is exited, the generated photocurrent changes because of the effect of the applied electric field which leds to a photocurrent that is added to the dark current, which effectively increases the conductivity [167]. As shown in figure 4.18 (a) and (b) large light current due to electron-hole pairs generated from valance band to conduction band which increases the current [143]. The maximum value of photocurrent is obtained for tungsten with photocurrent of 863.7 nA at a power of 12 W and the generated photocurrent for 850 nm laser is 7.49 nA. The generated photocurrent increases with power for 850 nm laser and tungsten in voltage biasing rang (-100 to +100 volt) as shown in figure 4.18(a) and (b). The reason for increasing photocurrent with increasing the

incident powers because it is narrow gap that suits the energy of photons irradiation from tungsten.

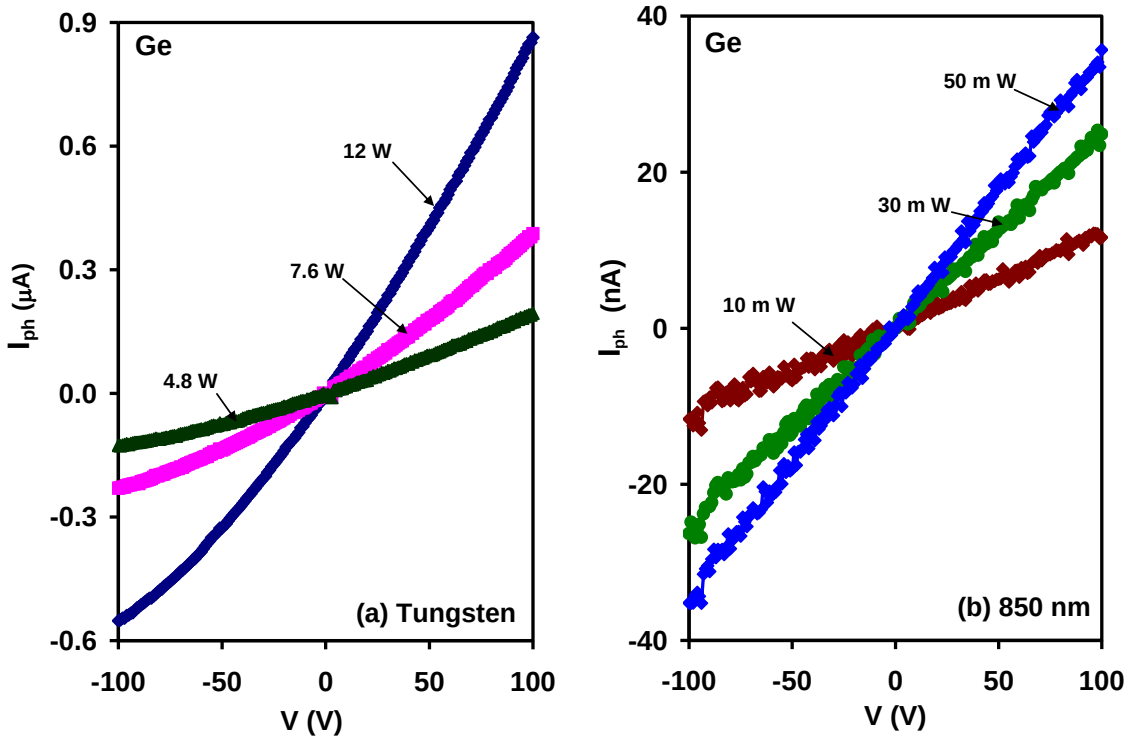

Fig. 4.18: I-V characteristics of Ge for (a) tungsten and (b) 850 nm laser.

The photoresponsivity (R_S) increases with increases the power of tungsten as shown in figure 4.19 (a) while *Rs* decreases with increases power as shown in figure 4.19(b) for 850 nm laser. The decrease in R_S with increased power of 850 nm laser could be attributed to the possibility that the photogenerated carriers were not collected to the electrodes. Another possibility is the shadow effect due to the thick electrodes (1 μm) by which a fair amount of photon could not enter the In/Ge/In [168] and because the energy photon for 850 nm laser is larger than energy band gap for Ge, the decreases is due to the high recombination via sensitizing states . The R_S variation with power under tungsten light is ascribed to the

extrinsic absorption which is dominated by energy photon for tungsten is lower than energy band gap foe Ge, the oxide layer on the top surface of Ge film . . R_S is 14 mA.W $^{-1}$ for 850 nm laser at a power of 5 mW which is larger than that for tungsten.

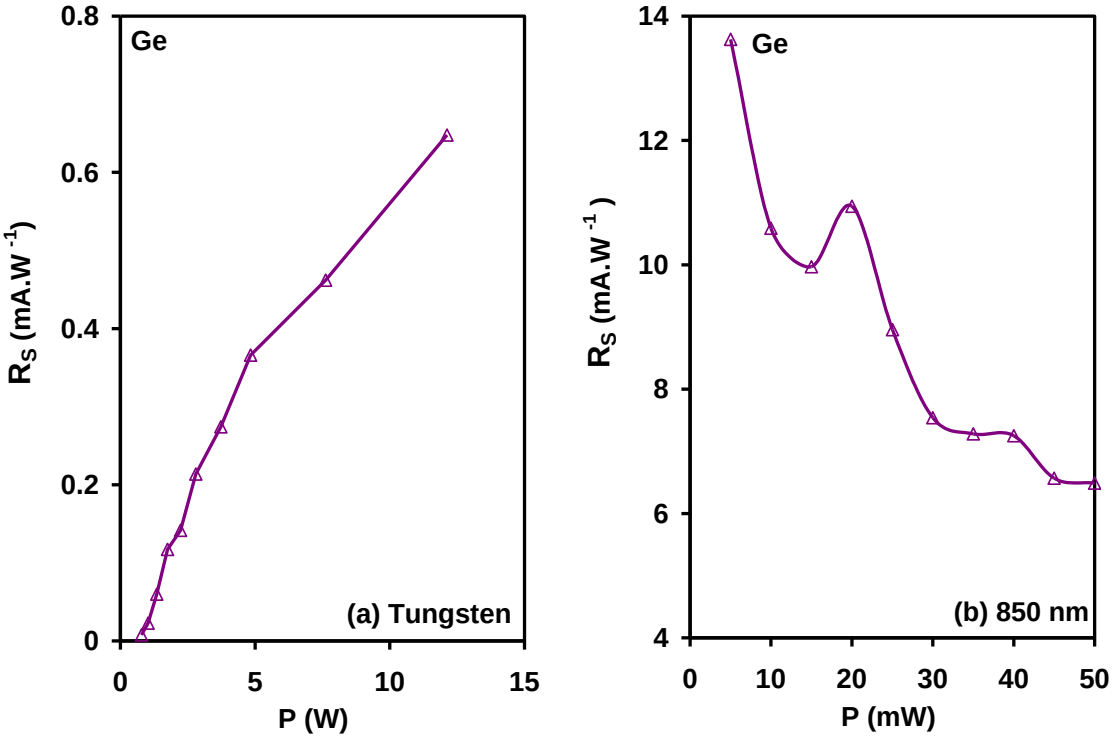

Fig. 4.19: The photoresponsivity (R_S) characteristics of Ge for (a) tungsten and (b) 850 nm laser.

Figure 4.20 show that S increases with increases power of tungsten and 850 nm laser. The device is more sensitive to tungsten light, S = 97% at a power of 12 W for tungsten and S = 0.77 % at a power of 5 mW for 850 nm laser.

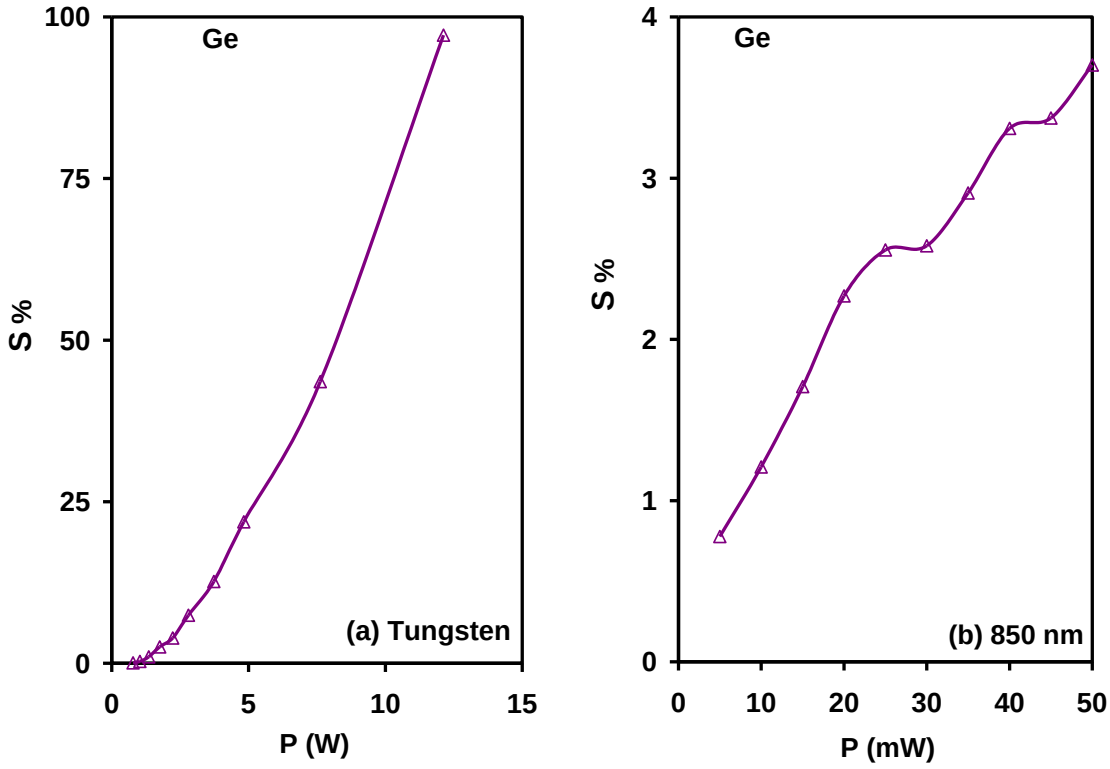

Fig. 4.20: The photosensitivity (S) characteristics of Ge for (a) tungsten and (b) 850 nm laser.

We indicate that EQE increases with power for tungsten as shown in figure 4.21(a). While it is decreases with power for 850 nm laser as shown in figure 4.21(b). The decreasing of EQE with power for 850 nm is due to decreasing in R_S with power and due to the long-lived trap states and presence of sensitizing states [155, 164]. EQE= 0.08 % for tungsten at a power of 12 W and EQE= 0.77 % for 850 nm laser at a power of 5 mW.

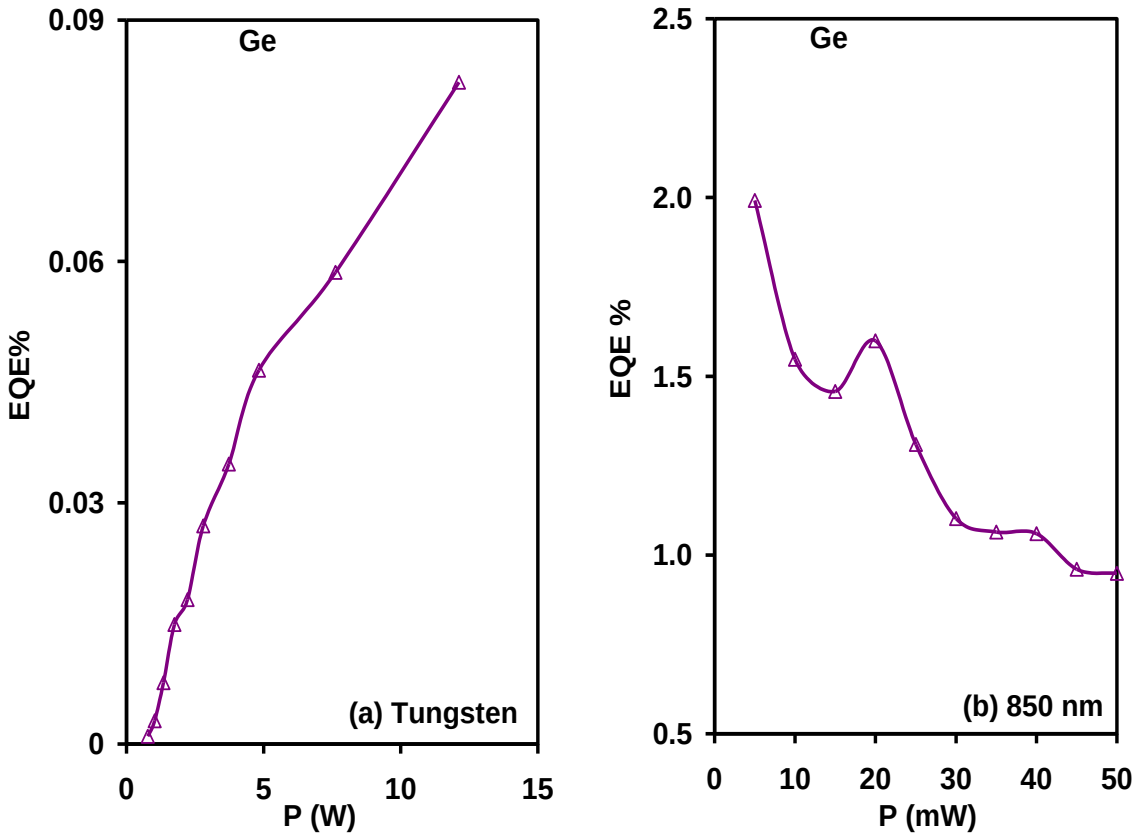

Fig.4. 21: The External Quantum Efficiency (EQE) characteristics of Ge for (a) tungsten and (b) 850 nm laser.

Figure 4.22 (a) shows that IQE increases with power for tungsten. While IQE decreases with power for 850 nm laser as shown in figure 4.22 (b). IQE = 0.179 % for tungsten at a power of 12 W and IQE= 3.21 % for 850 nm laser at a power of 5 mW. Finally all value for I_{ph}, R_S, S, EQE and IQE for Ge at different excitation of 850 nm laser and tungsten are listed in table 4.4.

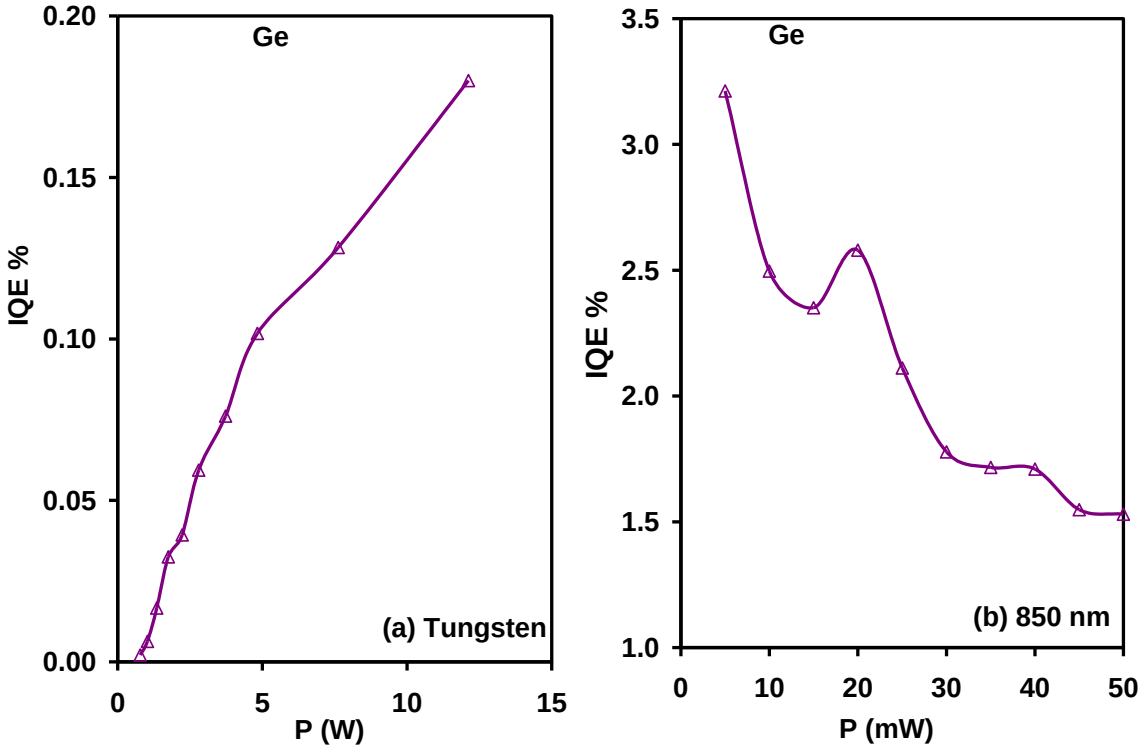

Fig. 4.22: The Internal Quantum Efficiency (IQE) characteristics of Ge for (a) tungsten and (b) 850 nm laser

Table 4.4: Results for In/Ge/In for 850 nm laser and tungsten excitation

In/Ge/In	I_{ph} (nA)	S%	R_S (mA.W $^{-1}$)	EQE%	Power	IQE%
tungsten	863.7	97.18	0.64	0.08	W12	0.179
850 nm	7.49	0.77	13.62	1.99	5 mW	3.21

4.2.4 Photoelectric properties of GaSe

GaSe is another material that is used in our photodetector array. In Our device In/GaSe/In, the metal In has a work function of 4.09 eV which is larger than the n-type GaSe work function (3.34 eV). We expect schottky behavior but, from figure 4.23 shows the I-V for GaSe under tungsten and 406 nm laser in the voltage biasing rang (-100 to +100 volt). As shown in figure 4.23 it is clear that the dark and light currents increase with increases voltage investigated that In/GaSe/In is an ohmic contact**.** The presence of ohmic contact is due to large electrodes separation and strong electric filed that make surface effects more dominate.

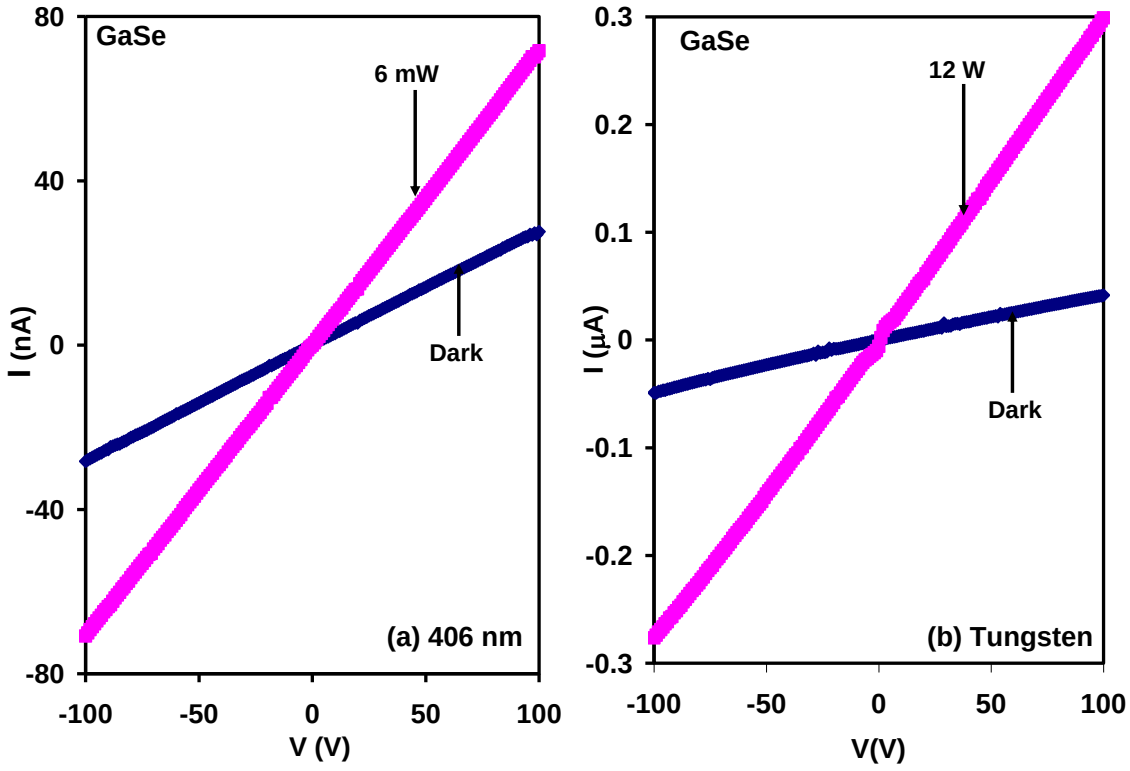

Fig. 4.23: Dark and light current I-V characteristics of GaSe for (a) 406-nm laser and (b) tungsten.

The generated photocurrent for 406 nm laser and tungsten increases with power as shown in figure 4.24. The photocurrent significantly increases under illumination compared to that of the dark current due to the photogenerated electron– hole pair which increased the photoconductivity [169]. Also, the generated photocurrent increases due to the effect of the applied electric field which leds to a photocurrent that are added to the dark current, which effectively increases the conductivity [144]. The photocurrent = 8 nA for 406 nm laser which agrees with [170]. Also, photocurrent has a maximum value of 257 nA for tungsten at power of 12 W which is due extrinsic absorption .

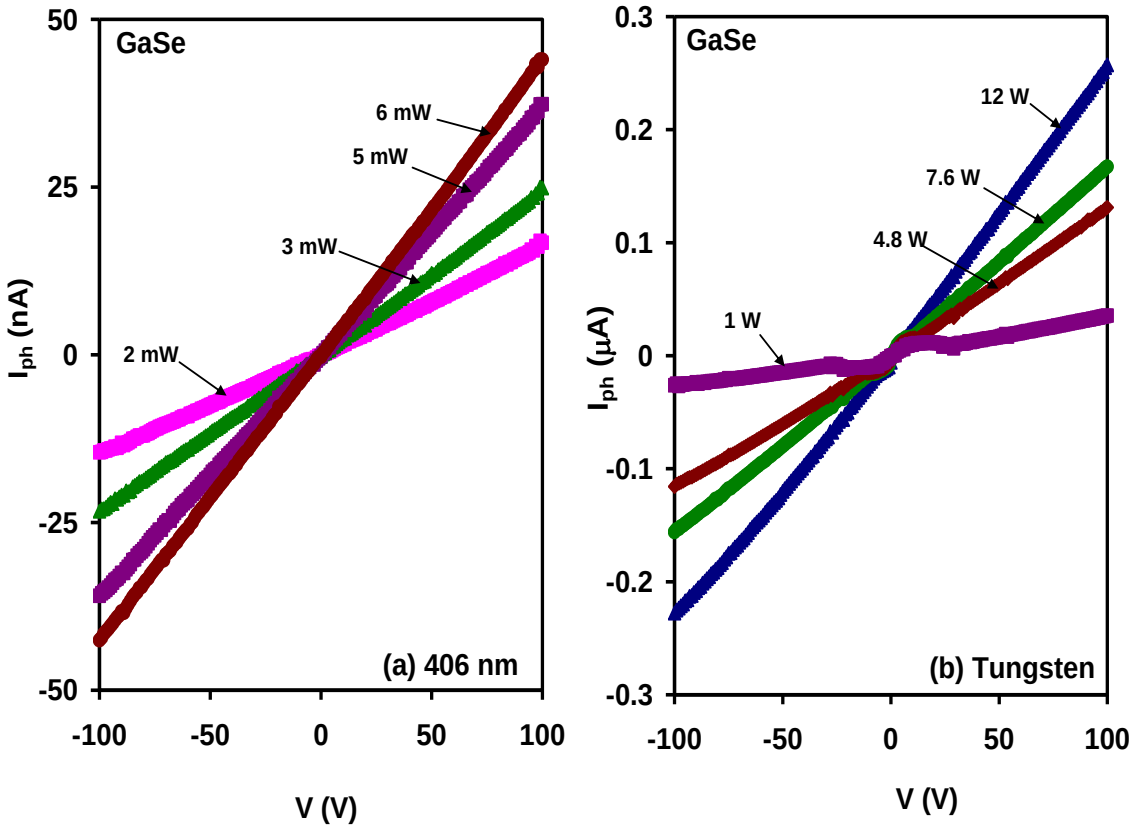

Fig. 4.24: I-V characteristics of GaSe for (a) 406-nm laser and (b) tungsten.

Figure 4.25 shows that R_S decreases with power of 406 nm and tungsten as .R_S decreases with power of 406 nm laser and tungsten due to increased recombination rate of photogenerated carriers [147] and capturing by lived trap states [149, 150] . R_S = 266.6 mA.W $^{-1}$ for 406 nm laser at a power of 0.5 mw which is the maximum value for GaSe. But, R_S= 0.35 mA.W^{-1} for tungsten at power of 12 W.

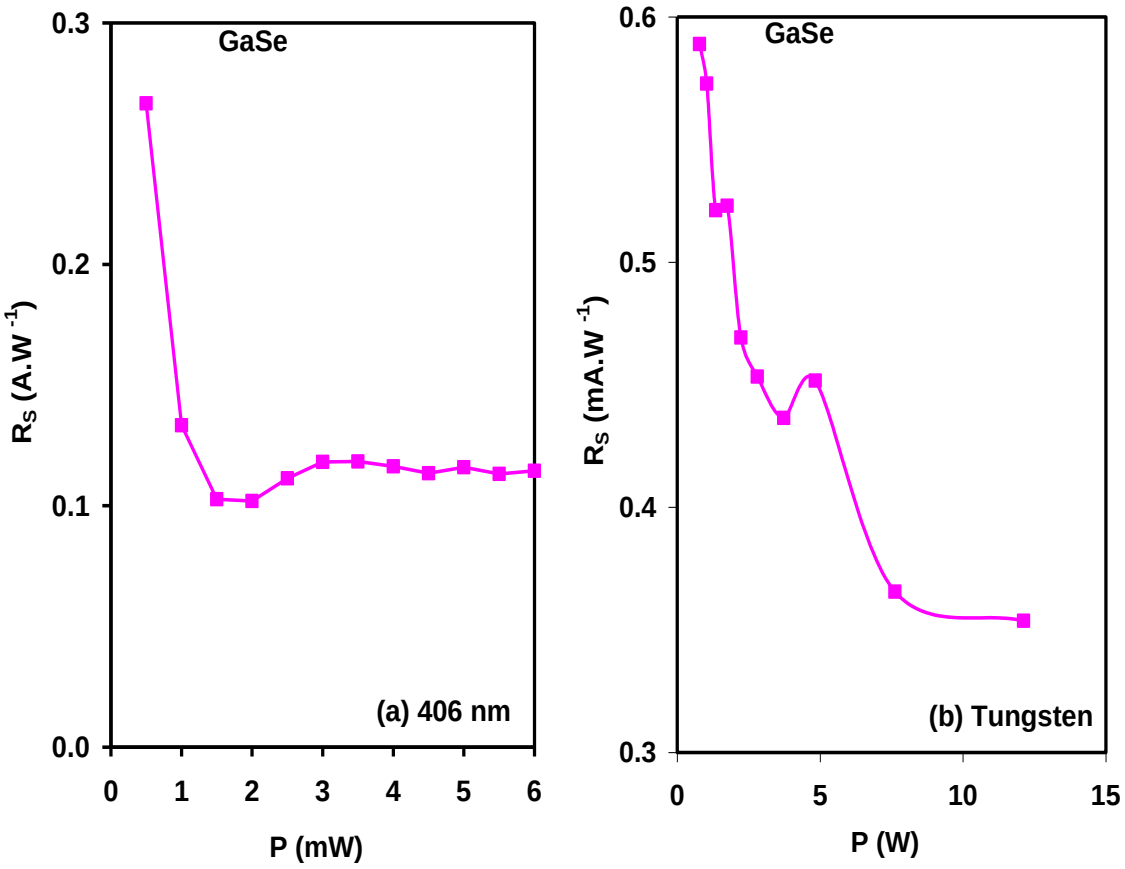

Fig. 4.25: The photoresponsivity (R_S) characteristics of GaSe for (a) 406-nm laser and (b) tungsten.

From our study, we found that GaSe is more sensitive for tungsten light. S = 618 % for tungsten at a power of 12 W. S = 28.9 % for 406 nm laser at a power of 0.5 mW. It is clear that from figure 4.26 (a) and (b) *S* increases with power of 406 nm laser and tungsten this due to increasing the number of photogenerated carriers.

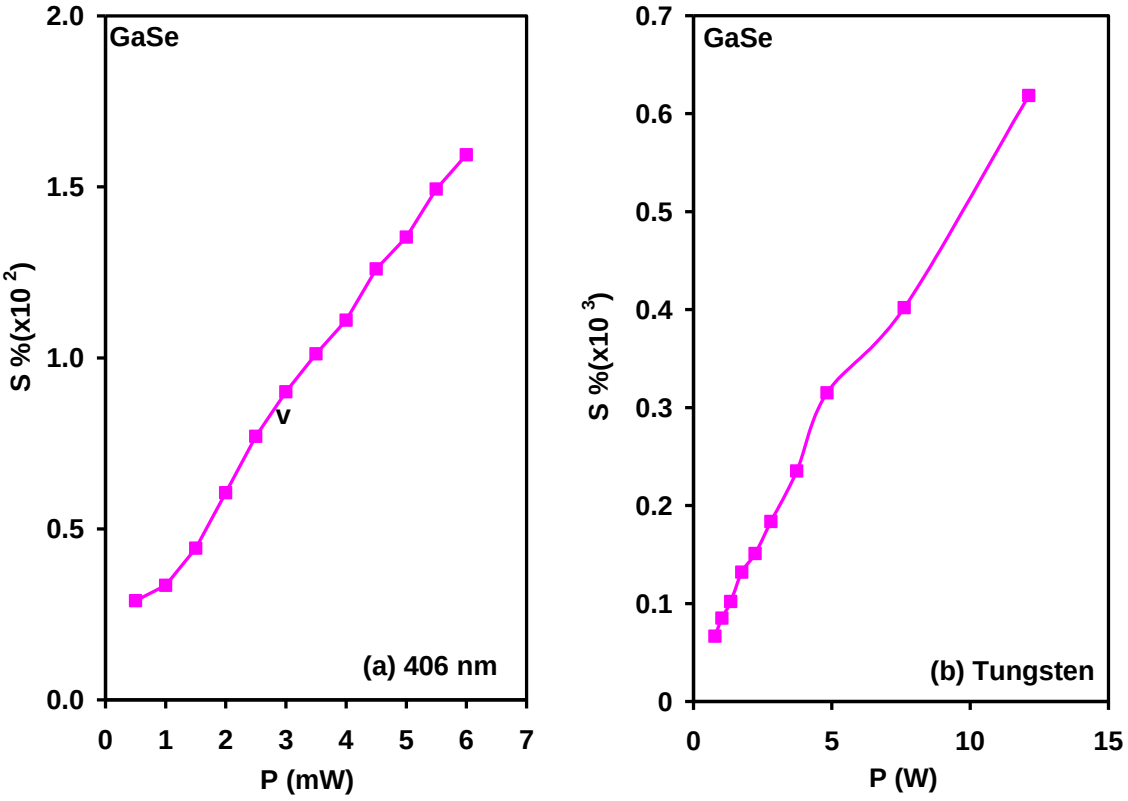

Fig. 4.26: The photosensitivity (*S*) characteristics of GaSe for (a) 406-nm laser and (b) tungsten.

EQE= 81.6 % for 406 nm laser at a power of 0.5 mW which is the maximum value that we obtained in this work for GaSe .This result agrees with [168]. EQE decreases with power of 406 nm laser and tungsten as shown in figure 4.27, because the photoresponsivity decreases as caused by trapping effects [166, 168]. EQE = 0.054 % for tungsten at a power of 12 W.

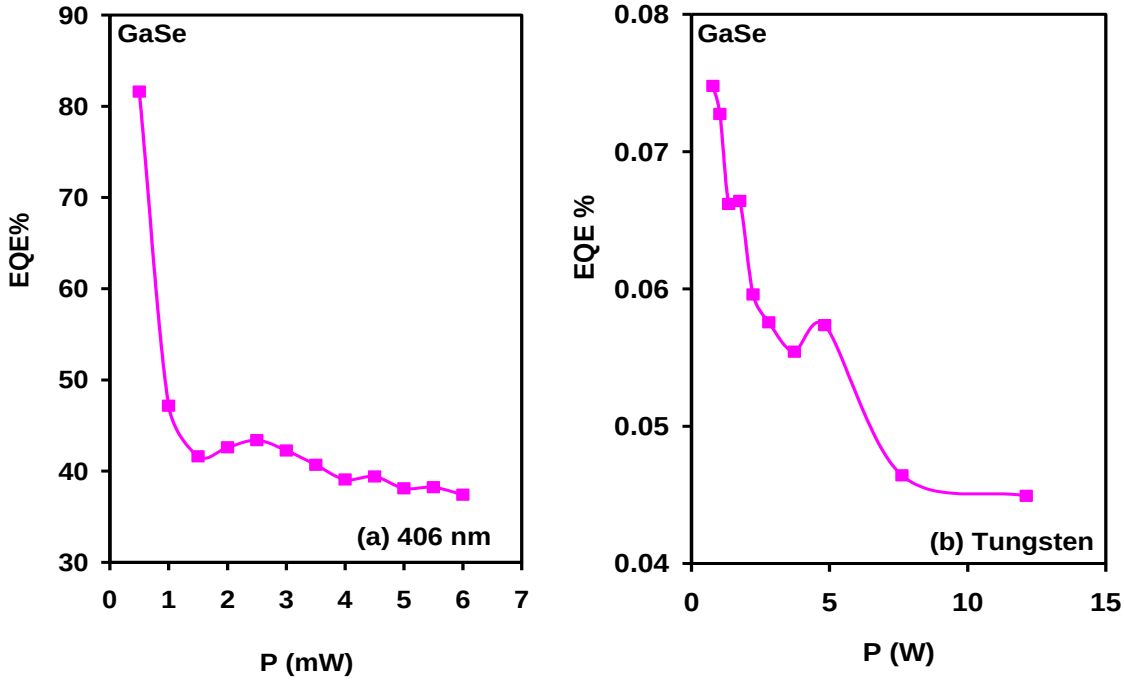

Fig. 4.27: The External Quantum Efficiency (EQE) characteristics of GaSe for (a) 406-nm laser and (b) tungsten.

IQE decreases with power for 406 nm laser and tungsten as shown in figure 4.28 (a) and (b). This due to decreasing in EQE. IQE= 91.6 % for 406 nm laser at a power of 0.5 mW which is the maximum value that we obtained for GaSe. However, it has small value for tungsten, which is equal 0.35 %. Finally, all value for I_{ph}, R_S, S, EQE and IQE for In/GaSe/In at different excitation of 406 nm laser and tungsten are listed in table 4.5.

Table 4.5: Results for In/GaSe/In for 406 nm laser and tungsten excitation.

In/GaSe/In	I_{ph}(nA)	S %	R_S (mA.W $^{-1}$)	EQE%	Power	IQE%
406 nm	8	28.9	266.6	81.6	0.5 mW	91.69
tungsten	257.3	618.5	0.35	0.04	12W	0.35

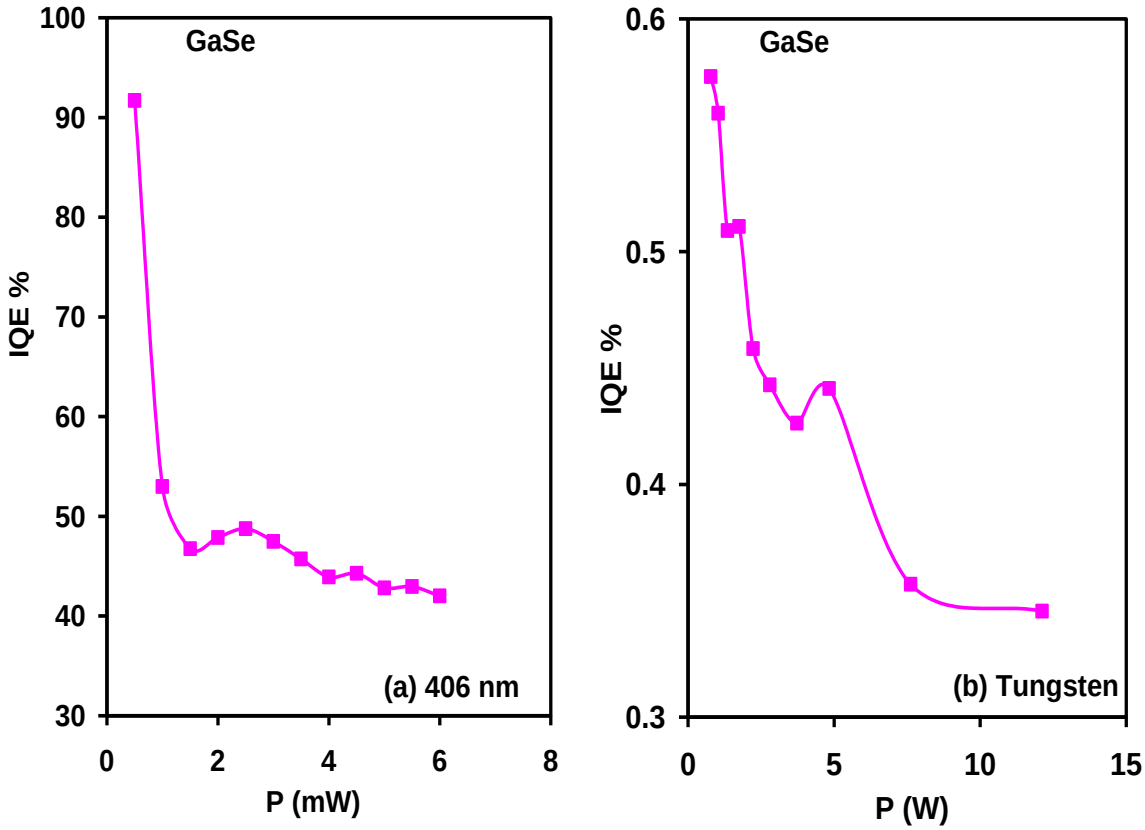

Fig. 4.28: The Internal Quantum Efficiency (IQE) characteristics of GaSe for (a) 406-nm laser and (b) tungsten.

4.2.5 Photoelectric properties of ZnS

Now we will talk about another material ZnS. In Our device (In/ZnS/In), the metal In has a work function of 4.09 eV which is lower than the p-type ZnS work function (7.0 eV) [171].We expect schottky behavior but the dark current increases with increases voltage investigated that In/ZnS/In is an ohmic contact**.** The presence of ohmic contact is due to large electrodes separation and strong electric filed that make surface effects more dominate. The measurements of the generated photocurrent for different types of lasers and tungsten are very small, because photon energies for lasers and tungsten are smaller than

the energy band gap of ZnS. Our generated photocurrent for lasers and tungsten is in the order of few nano Amperes. Our results agree with [172] in which they found that the generated photocurrent is in the order of Pico Ampere for wavelength in the range (300 to 600 nm). ZnS does not respond to tungsten and lasers so we will not take it in our photoconductor array.

4.2.6 Photoelectric properties of InSe/CdS heterojunction

We designed a heterojunction which consists of (InSe/CdS) thin films. Both of InSe and CdS are n-type semiconductors which represent isotope heterojunction device, the main difference between the two materials in the energy band gaps which exhibit respective values of 2.39 and 2.2 eV. The difference in the energy band gaps is 0.19 eV. As the electron affinity of CdS is 4.5 eV [173] and for InSe is 4.55 eV [174], then $\Delta E_{C} =$ 0.05 eV and $\Delta E_{V} =$ 0.15 eV. The low valance and conduction bands off sets for the two materials make them optically identical, but structurally different. This structure has no role on the recombination dynamics but increases photo generated pairs. Figure 4.29 shows the I-V for (InSe/CdS) heterojunction under tungsten and 406 nm laser in the voltage biasing rang (-100 to +100 volt). As shown in figure 4.29 it is clear that the dark and light currents increase with increases voltage investigated that the shoulder of the device In/ InSe/CdS /In are an ohmic contact.

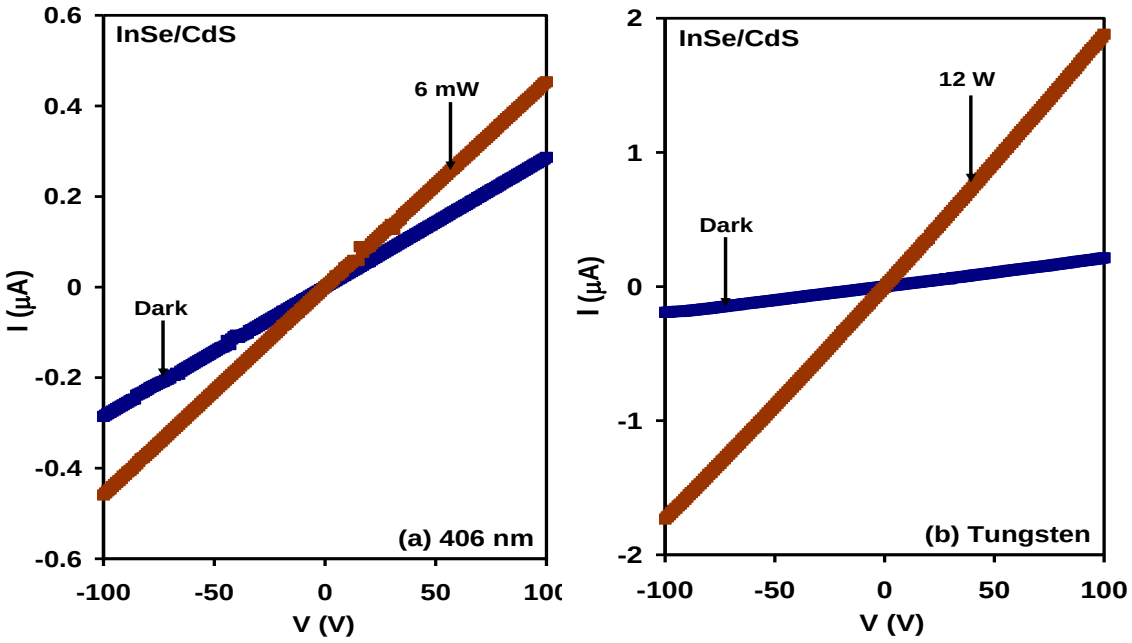

Fig. 4.29: Dark and light current I-V characteristics of (InSe/CdS) for (a) 406-nm laser and (b) tungsten.

The generated photocurrent for 406 nm laser and tungsten increases with power as shown in figure 4.30. The photocurrent significantly increases under illumination compared to that of the dark current due to the photogenerated electron– hole pair which increased the conductivity [166] and due to the effect of the applied electric field [144]. We found that the generated photocurrent for tungsten is the highest compared to 406 nm laser as shown in figure 4.30 (a) and (b) But, this value for tungsten is smaller compared to InSe and CdS thin films alone. The generated photocurrent for tungsten is 166.9 nA while it is equal 48.2 nA for 406 nm laser at power of 0.5 mW.

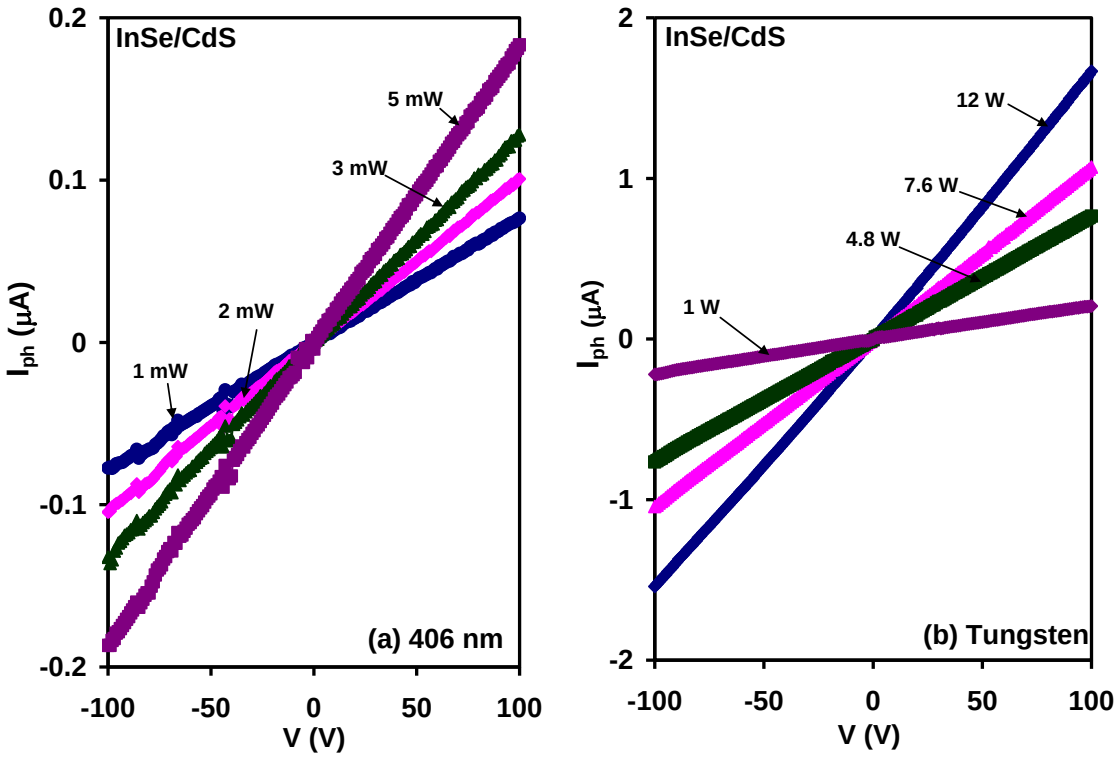

Fig. 4.30: I-V characteristics of (InSe/CdS) for. a) 406-nm laser and b) tungsten.

Figure 4.31 shows that R_S decreases with power of 406 nm and tungsten as .R_S decreases with power of 406 nm laser and tungsten due to increased recombination rate of photogenerated carriers [147] and due to capturing by trap states [168]. R_S = 2.4 A.W $^{-1}$ for 406 nm lasers at a power of 0.5 mW which is the largest value that we obtained compared to tungsten which is equal 3.5 mA.W^{-1}.

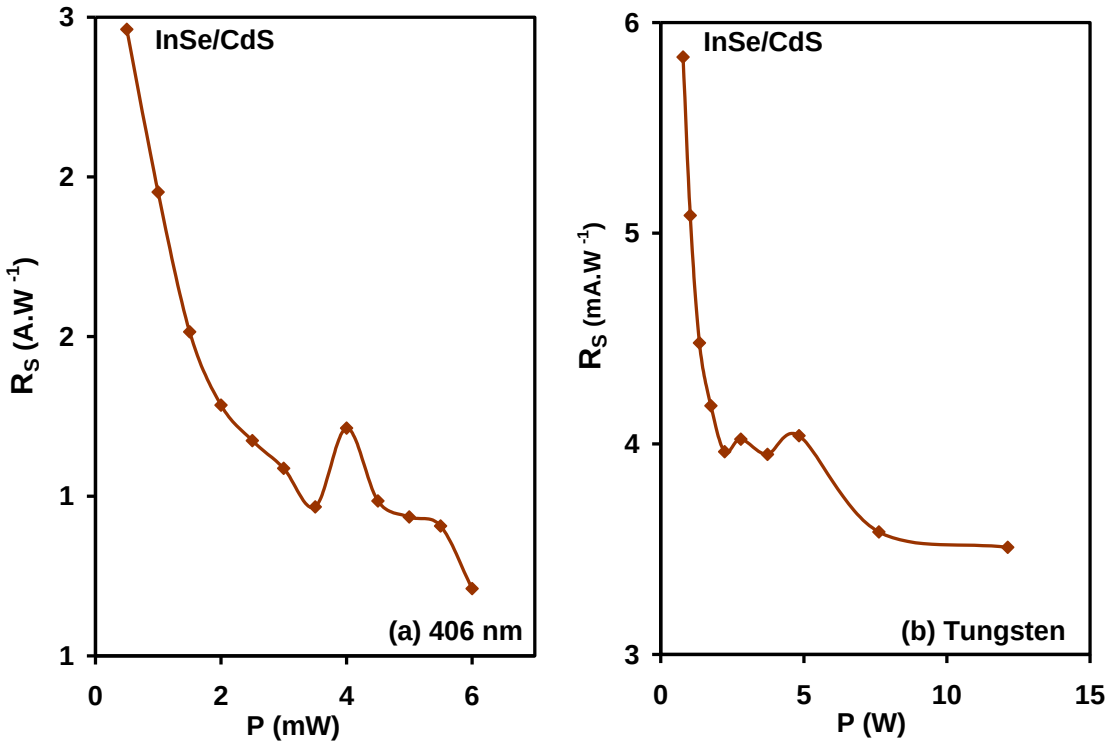

Fig. 4.31: The photoresponsivity (R_S) characteristics of (InSe/CdS) for (a) 406-nm laser and (b) tungsten.

The value of S is 780 % for tungsten at a power of 12 W which is the maximum that we obtained for InSe/CdS compared to 406 nm laser which is equal 16.8 % at power of 0.5 mW. Also, *S* increases with the power of tungsten and 406 nm laser due to the increases in the number of photo carriers with power as shown in figure 4.32.

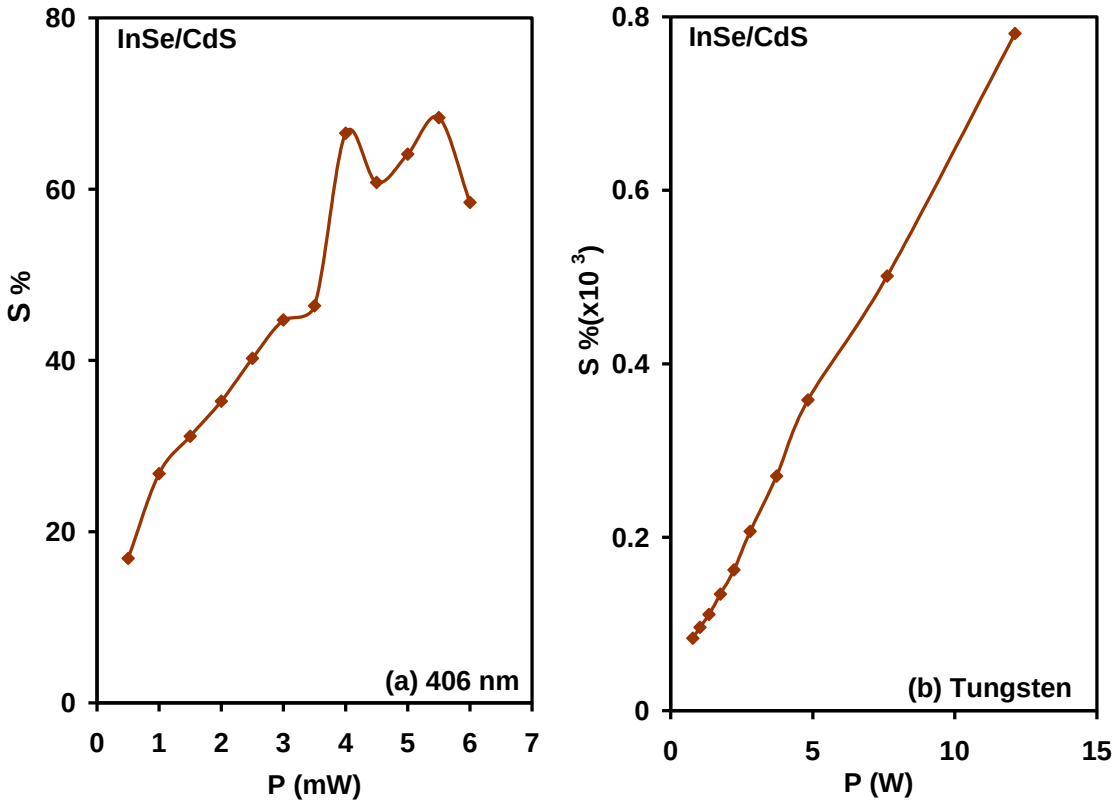

Fig. 4.32: The photosensitivity (*S*) characteristics of (InSe/CdS) for (a) 406-nm laser and (b) tungsten.

EQE= 753.56 % for 406 nm laser at a power of 0.5 mW which is the maximum value compared to tungsten which is equal 0.44% at power of 12 W. EQE decreases with power of 406 nm laser and tungsten as shown in figure 4.33,because the photoresponsivity decreases as caused by trapping effects [166, 168]. EQE is lower than that of InSe and larger than that of CdS at 406 nm laser at a power of 0.5 mW. EQE for tungsten is lower than that of InSe and larger than that of CdS.

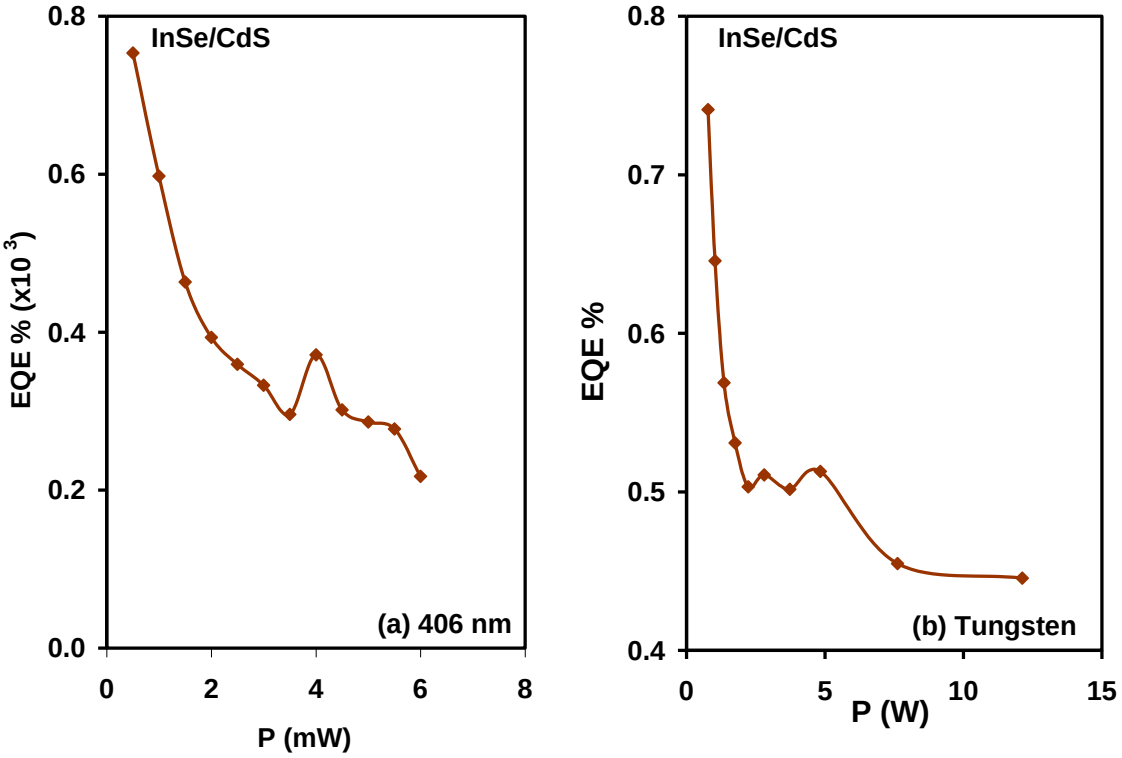

Fig. 4.33: The External Quantum Efficiency (EQE) characteristics of (InSe/CdS) for (a) 406-nm laser and (b) tungsten.

IQE decreases with power for 406 nm laser and tungsten as shown in figure 4.34 (a) and (b) due to decreasing in EQE. At 406 nm laser there is absorption saturation so internal quantum efficiency is guided by properties of EQE[153]. IQE= 793 % for (InSe/CdS) for 406 nm laser which is the largest value that we obtained compared to tungsten which is equal 1.55 % at a power of 12 W. IQE for tungsten for (InSe/CdS) is lower than that of InSe and CdS. Finally all value for I_{ph}, R_S, S, EQE and IQE for In/GaSe/In at different excitation of 406 nm laser and tungsten are listed in table 4.6.

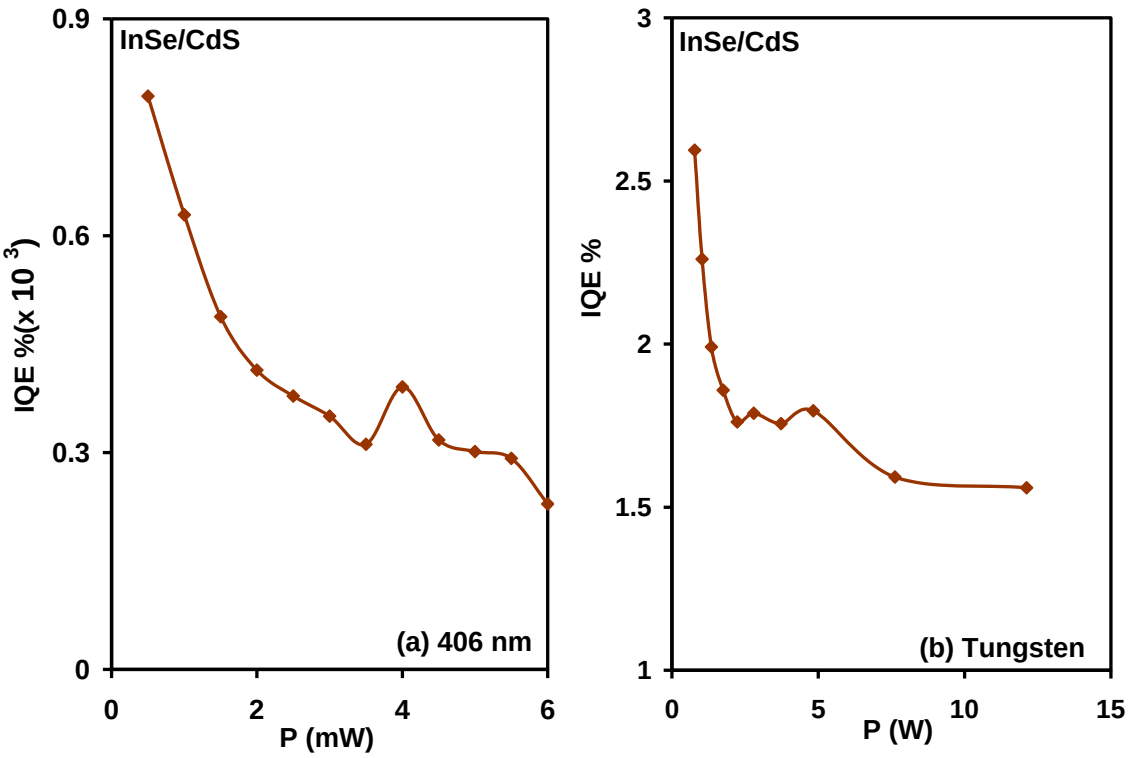

Fig. 4.34: The Internal Quantum Efficiency (IQE) characteristics of InSe/CdS for a) 406-nm laser and b) tungsten.

Table 4.6: Results for (InSe/CdS) heterojunction for 406 nm laser and tungsten excitation.

InSe/CdS	I_{ph}(nA)	S %	R_S (mA.W $^{-1}$)	EQE%	Power	IQE%
406 nm	48.2	16.87	2462.2	753.5	0.5 mW	793.1
tungsten	1666.9	780.75	3.50	0.44	W12	1.55

4.2.6 Photoelectric properties of connected and separated array

We designed a connected and separated array to study and compare photoelectric properties as shown in figure 4.35. The I-V characteristics of the array measured in the dark, under tungsten power in the range of 1.0-12.0 W. From figure 4.36 it is clear that the dark and light current increases linearly with increases voltage investigated that we have an ohmic contact.

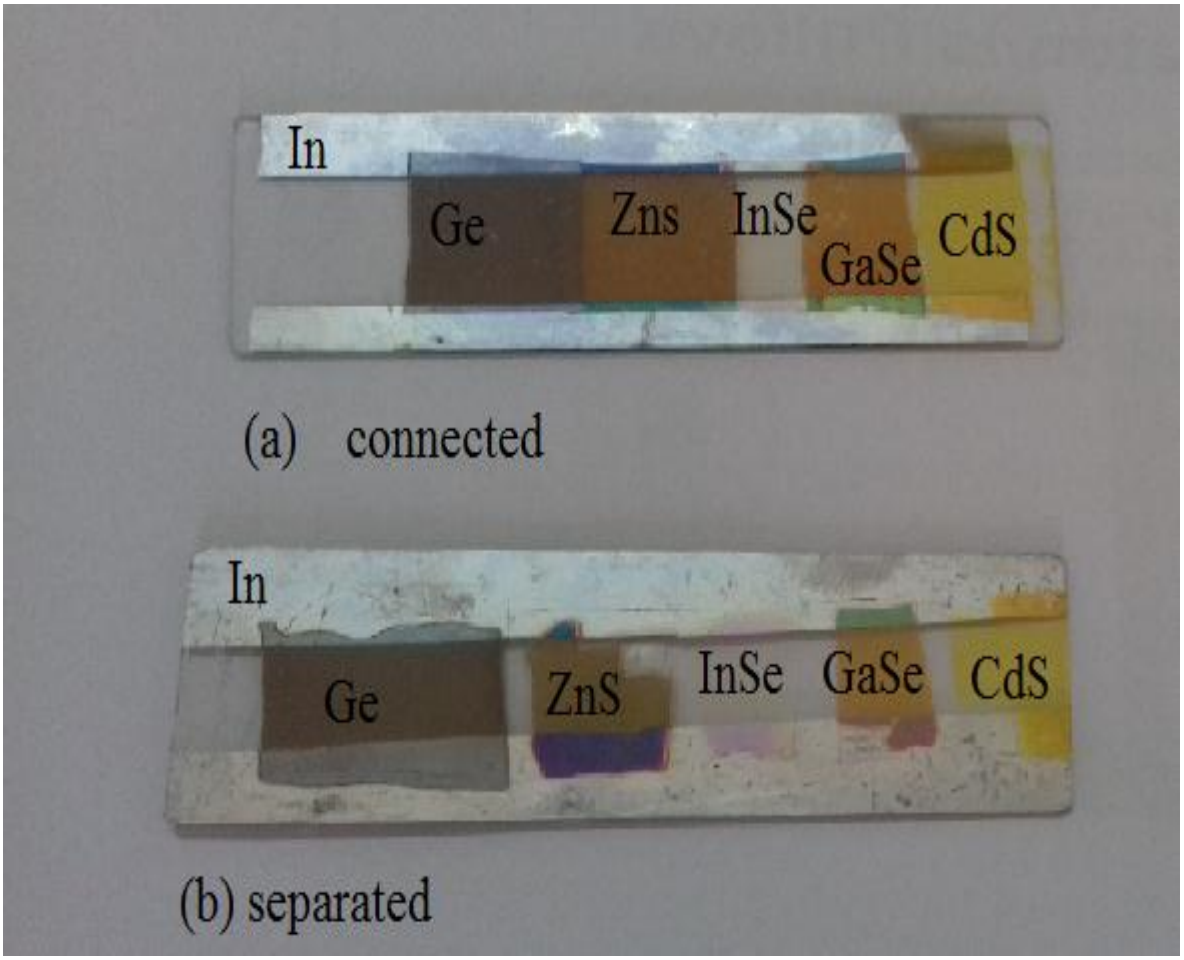

Fig.4.35: The geometrical design of (a) connected array (b) separated

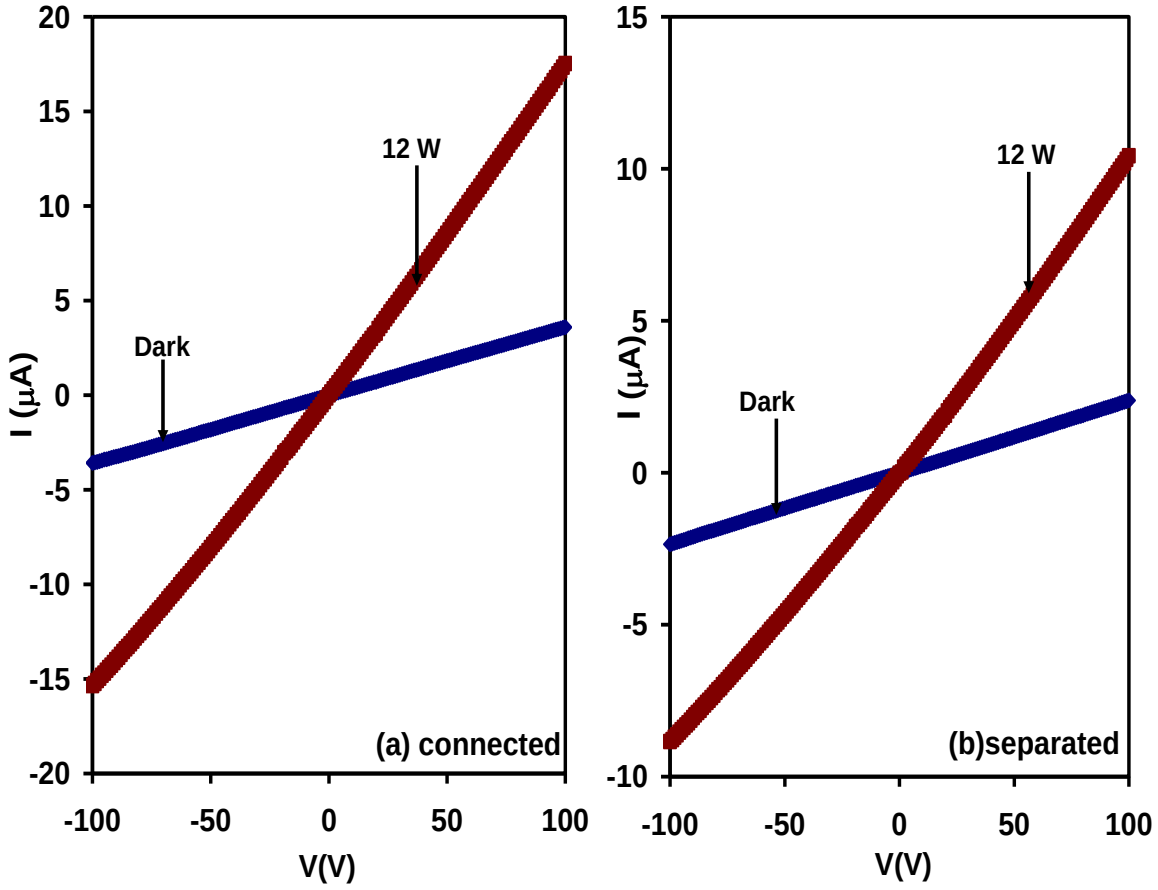

Fig. 4.36: Dark and light current I-V characteristics of (a) connected array and (b) separated array for tungsten.

Connected and separated array are illuminated with tungsten under voltage bias ranges in range of (-100 to +100 Volt). The generated photocurrent increases because of the effect of the applied electric [144] . As shown in figure 4.36 (a) and (b) the light current is larger than the dark current due to photoelectric effect [16].The generated photocurrent increases with power of tungsten in voltage biasing rang (-100 to +100 volt) as shown in figure 4.37 (a), (b).The reason for increasing photocurrent with increasing the incident powers is the availability of more free carriers associated with material supplementary. Our study

indicates that generated photocurrent for connected array equal 13925 nA is larger than that of separated array which is equal 8049 nA. The photocurrent is increased by more than 1.7 times when heterojunction between device was allowed .

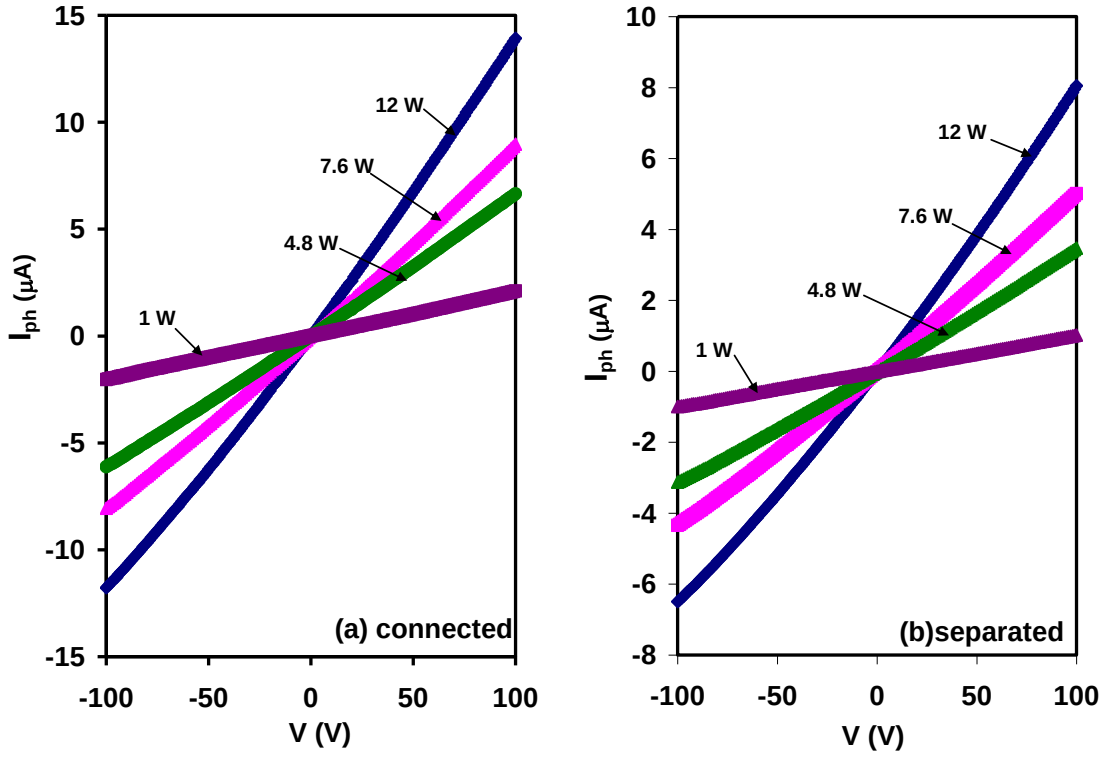

Fig. 4.37: The I-V characteristics of (a) connected array (b) separated array for tungsten.

The photoresponsivity (R_S) decreases with increases the power of tungsten as shown in figure 4.38(a) and (b). The decrease in photoresponsivity with increased power of tungsten could be attributed to trapping and sensitizing states [164] also, due to the increased recombination rate of photogenerated carriers [147]. We found that R_S = 1.59 mA.W $^{-1}$ for connected array which is larger than that of separated array. But, it is still smaller than all

other materials because the area of connected array and separated array is larger than other thin films materials and R_S decreases with area.

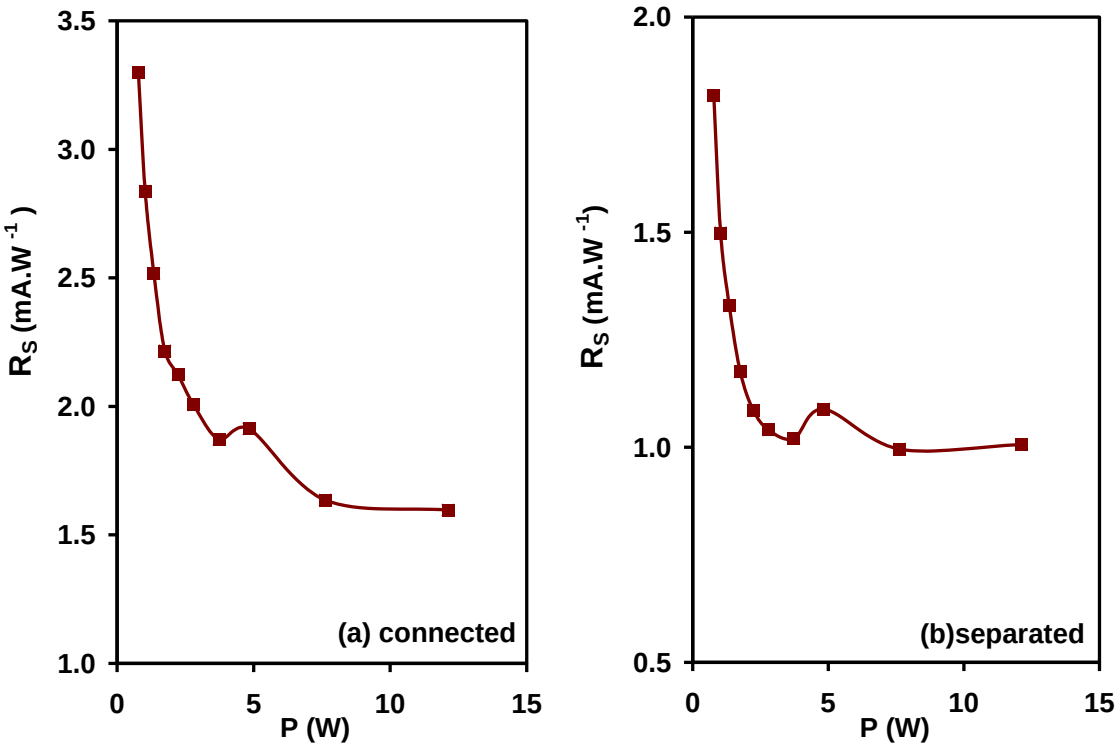

Fig. 4.38: The photoresponsivity (R_S) characteristics of a) connected array .b) separated array for tungsten.

From figure 3.39 we indicate that S increases with power. Connected array is more sensitive for tungsten light S= 387 % for connected array which is larger than that of separated array which is equal 338 %.

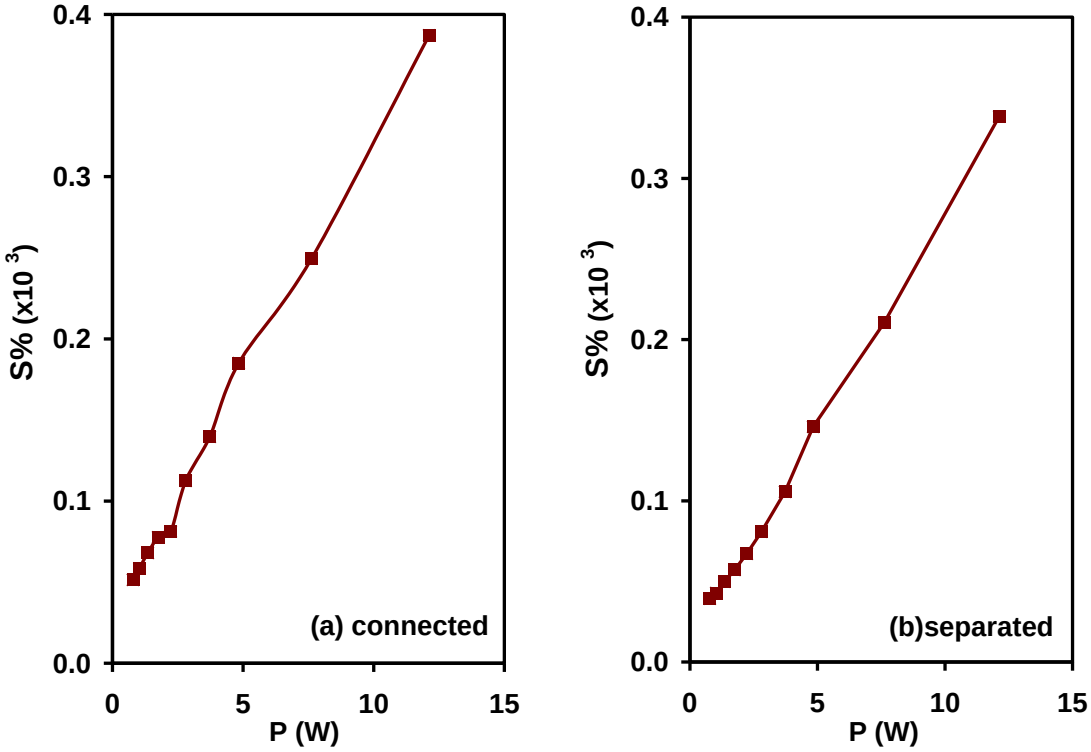

Fig. 4.39: The photosensitivity (S) characteristics of (a) connected array (b) separated array for tungsten.

It is clear that from figure 4.40 (a), (b) EQE for tungsten decreases with power. The decreasing of EQE with power for tungsten is due to decreasing in R_S with power and due to the absorption saturation [153]. Also, maybe due to long-lived trap states [153]. EQE = 0.2 % for connected array which is larger than that for separated array. Finally all value for I_{ph}, R_S, S, EQE and IQE for connected and separated array at excitation of tungsten are listed in table 4.7.

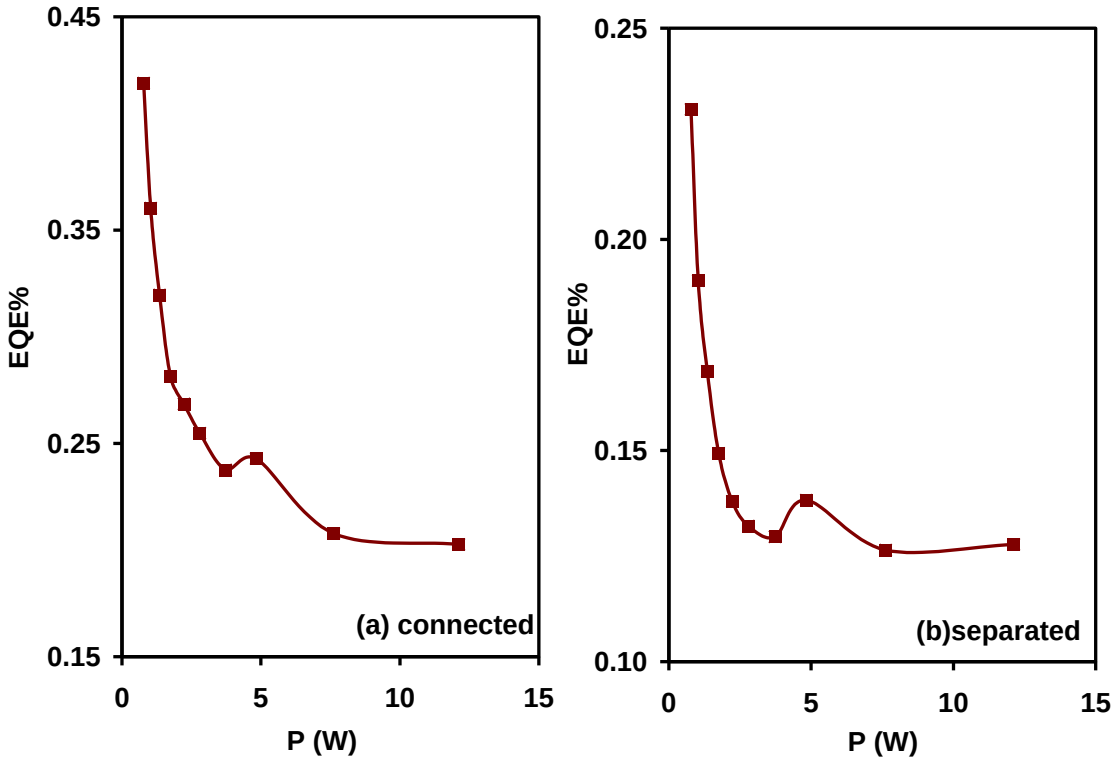

Fig. 4.40: The External Quantum Efficiency (EQE) characteristics of (a) connected array. (b) Separated array for tungsten

Table 4.7: Results for connected and separated array tungsten excitation.

Material	I_{ph} (nA)	S %	R_S (mA.W $^{-1}$)	EQE%	Power
Connected array	13925	387.1	1.59	0.20	W12
Separated array	8049	338.3	1.06	0.12	W12

Table 4.8: Results for 406 nm Laser

Material	I_{ph} (nA)	S %	R ($mA.W^{-1}$)	EQE%	P (mW)	IQE%
InSe	236.1	21.9	4920	1505.7	0.5	1757
InSe/CdS	48.2	16.87	2462.2	753.5	0.5	793.1
GaSe	8	28.9	266.6	81.6	0.5	91.69
CdS	166	21.2	2373.4	726.3	0.5	981.5

Table 4.9: Results for 632nm laser

Material	I_{ph} (nA)	S %	R ($mA.W^{-1}$)	EQE%	P (mW)	IQE%
InSe	16.3	1.32	170.7	33.5	1	57.5
CdS	20.1	6.36	143	28.1	1	937.2

Table 4.10: Results for Tungsten light.

Material	I_{ph} (nA)	S %	R ($mA.W^{-1}$)	EQE%	P (W)	IQE%
Ge	863.7	97.18	0.64	0.08	12.12	0.179
InSe	7411.4	577.1	6.65	0.08	12.12	7.35
InSe/CdS	1666.9	780.75	3.50	0.44	12.12	1.55
GaSe	257.3	618.5	0.35	0.04	12.12	0.35
CdS	4705	1277	2.75	0.34	12.12	3.17
Contacted array	13925	387.1	1.59	0.20	12.12	
Separated array	8049	338.3	1.06	0.12	12.12	

Table 4.11: Results for 850 nm laser

Material	I_{ph} (nA)	S %	R ($mA.W^{-1}$)	EQE%	P (W)	IQE%
Ge	7.49	0.77	13.62	1.99	5	3.21
InSe	180.16	16.33	375.3	54.86	5	623.4

We found from tables 4.8-4.11 that the maximum value of photosensitivity is achieved for Cadmium sulfide for 406 nm lasers at a power of 0.5 mw while the maximum value of generated photocurrent is achieved for connected array for tungsten at a power of 12 W. The maximum values of external quantum efficiency, internal quantum efficiency and photoresponsivity are achieved for Indium Selenide for 406 nm lasers at a power of 0.5 mW. It is clear that the best two materials are InSe and CdS which can be used in many applications such as photovoltaic device and light sensitive switch in visible rejoin.

Conclusions

In this thesis, a wide band photoconductor array is designed and characterized. The wide band photoconductor array is designed from materials exhibiting energy band gaps of values in the range 1.1-3.33 eV. Our photoconductor array consists of Cadmium sulfide, Gallium Selenide, Indium Selenide, Germanium, Zinc Sulfide and Indium Selenide/ Cadmium sulfide heterojunction. The photoconductor array is subjected to various types of laser excitations including lasers of wavelengths of 406, 632, 850 and 1550 nm and tungsten light. The measurements allowed determining the array photoresponsivity, photosensitivity, external quantum efficiency and internal quantum efficiency

We studied the photosensitivity, generated photocurrent, external quantum efficiency, internal quantum efficiency and photoresponsivity for Cadmium sulfide, Gallium Selenide, Indium Selenide, Germanium, Zinc Sulfide and Indium Selenide/ Cadmium sulfide heterojunction to form a photoconductor array.

For Cadmium sulfide, we found that photosensitivity and generated photocurrent increases with power for lasers and tungsten light while external quantum efficiency, internal quantum efficiency and photoresponsivity decrease with power for lasers and tungsten light. For Indium Selenide, we found that photosensitivity and generated photocurrent increases with power for lasers and tungsten light while external quantum efficiency, internal quantum efficiency and photoresponsivity decrease with power for lasers and tungsten light.

For Germanium, we found that photosensitivity increases with power for lasers and tungsten light while external quantum efficiency, internal quantum efficiency and

photoresponsivity decrease with power for 850 nm laser. But for tungsten the external quantum efficiency, internal quantum efficiency and photoresponsivity increases with power. The generated photocurrent increases with power for tungsten light and 850 nm laser. For Gallium Selenide, we found that photosensitivity and generated photocurrent increases with power for lasers and tungsten light while external quantum efficiency, internal quantum efficiency and photoresponsivity decrease with power for lasers and tungsten light.

For Indium Selenide/ Cadmium sulfide heterojunction, we found that photosensitivity and generated photocurrent increases with power for lasers and tungsten light while external quantum efficiency, internal quantum efficiency and photoresponsivity decrease with power for lasers and tungsten light.

For connected and separated photoconductors array, we found that photosensitivity and generated photocurrent increases with power for tungsten light while external quantum efficiency, internal quantum efficiency and photoresponsivity decrease with power for tungsten light.

It is clear that the best two materials are InSe and CdS which can be used in many applications such as photovoltaic device, light sensitive switch in visible rejoin and camera light meters. We are looking in the future to increasing the EQE, IQE, R_S and S for this device by design photoconductor in nanoscale technology.

References:

[1]Lev I. Beger, *Semiconductor Materials* (CRC Press, New York, 1997), p.198-199.
[2] Charles Kittel, *Introduction to Solid State Physics* (John Wiley & Sons, NJ, 2005), p.187-189

[3] Nussbaumer, Hartmut. *Herstellung und Eigenschaften rekristallisierter Siliziumschichten*. UFO, Atelier für Gestaltung und Verlag, 1996.
[4] Mak, Kin Fai, et al. "The valley Hall effect in MoS2 transistors." *Science*344.6191 (2014): 1489-1492.

[5] Chavan, Padmakar G., et al. "Photo-enhanced field emission studies of tapered CdS nanobelts." *Vacuum Nanoelectronics Conference (IVNC), 2014 27th International*. IEEE, 2014.
[6] Dey, Riya, and Vineet Kumar Rai. "Yb 3+ sensitized Er 3+ doped La 2 O 3 phosphor in temperature sensors and display devices." *Dalton Transactions*43.1 (2014): 111-118.

[7] Zhou, Huanping, et al. "Interface engineering of highly efficient perovskite solar cells." *Science* 345.6196 (2014): 542-546.
[8] Basak, D., et al. "Photoconductive UV detectors on sol–gel-synthesized ZnO films." *Journal of Crystal Growth* 256.1 (2003): 73-77.

[9] Aalseth, Craig E., et al. "CoGeNT: A search for low-mass dark matter using p-type point contact germanium detectors." *Physical Review D* 88.1 (2013): 012002.
[10]Liu, J.-M. Photonic Devices, P 943. (2005).

[11] Liu, Xingqiang, et al. "Transparent, High - Performance Thin - Film Transistors with an InGaZnO/Aligned - SnO2 - Nanowire Composite and their Application in Photodetectors." *Advanced Materials* 26.43 (2014): 7399-7404.
[12] Hazra, Purnima, S. K. Singh, and S. Jit. "Ultraviolet photodetection properties of ZnO/Si heterojunction diodes fabricated by ALD technique without using a buffer layer." *JSTS: Journal of Semiconductor Technology and Science* 14.1 (2014): 117-123.

[13] Gong, Xiwen, et al. "Highly efficient quantum dot near-infrared light-emitting diodes." *Nature Photonics* 10.4 (2016): 253-257.
[14] Konstantatos, Gerasimos, and Edward H. Sargent. "Nanostructured materials for photon detection." *Nature nanotechnology* 5.6 (2010): 391-400.

[15] Xiong, Kanglin, et al. "Single crystal gallium nitride nanomembrane photoconductor and field effect transistor." *Advanced Functional Materials*24.41 (2014): 6503-6508.
[16] A. Einstein, Ann. Phys. (Leipzig) 322, 132 (1905)

[17] Logothetidis, S., et al. "Optical properties and temperature dependence of the interband transitions of cubic and hexagonal GaN." *Physical Review B* 50.24 (1994): 18017.
[18] Dumke, W. P. "Optical transitions involving impurities in semiconductors." *Physical Review* 132.5 (1963): 1998.

[19]Hylton, N. P., et al. "Loss mitigation in plasmonic solar cells: aluminium nanoparticles for broadband photocurrent enhancements in GaAs photodiodes." *Scientific reports* 3 (2013).
[20]Gao, Wei, et al. "In0. 53Ga0. 47As metal - semiconductor - metal photodiodes with transparent cadmium tin oxide Schottky contacts." *Applied physics letters* 65.15 (1994): 1930-1932.

[21]Ghosh, Subir, et al. "A tunable colloidal quantum dot photo field-effect transistor." *Applied Physics Letters* 99.10 (2011): 101102.
[22] Petritz, Richard L. "Theory of photoconductivity in semiconductor films." *Physical Review* 104.6 (1956): 1508.

[23]Wang, Chen, et al. "High-Performance Ge pn Photodiode Achieved With Preannealing and Excimer Laser Annealing." *IEEE Photonics technology letters* 27.14 (2015): 1485-1488.
[24]Di Bartolomeo, Antonio, et al. "Hybrid graphene/silicon Schottky photodiode with intrinsic gating effect." *2D Materials* 4.2 (2017): 025075.

[25]El Amrani, A., B. Lucas, and Rémi Antony. "Organic optocoupler consisting of an optimized blue organic light emitting diode and an organic photoconductor." *Superlattices and Microstructures* 85 (2015): 880-885.
[26]Sze, Simon Min. *Semiconductor devices: physics and technology*. John Wiley & Sons, 2008.

[27]So, Hongyun, and Debbie Senesky. "Effect of Frost Formation on Operation of GaN Ultraviolet Photodetectors at Low Temperature." *IEEE Sensors Journal* (2017).
[28] Lin, Chien-Jen, and Li-Ming Deng. "Shadow approach for real-time hand gesture recognition using a light-dependent resistor array." *Sensors Applications Symposium (SAS), 2017 IEEE*. IEEE, 2017.

[29] Jin, Zhiwen, et al. "High-performance flexible ultraviolet photoconductors based on solution-processed ultrathin ZnO/Au nanoparticle composite films." *Scientific reports* 4 (2014).
[30]Lin, Keng-Te, et al. "Nanocrystallized CdS beneath the Surface of a Photoconductor for Detection of UV Light with Picowatt Sensitivity." *ACS applied materials & interfaces* 6.22 (2014): 19866-19875.

[31] Monroy, Eva, Franck Omnès, and Fernando Calle. "Wide-bandgap semiconductor ultraviolet photodetectors." *Semiconductor Science and Technology* 18.4 (2003): R33.
[32] Peng, Lin, Linfeng Hu, and Xiaosheng Fang. "Low - dimensional nanostructure ultraviolet photodetectors." *Advanced Materials* 25.37 (2013): 5321-5328.

[33] Hu, PingAn, et al. "Highly responsive ultrathin GaS nanosheet photodetectors on rigid and flexible substrates." *Nano letters* 13.4 (2013): 1649-1654.
[34] Ma, Chun, et al. "Heterostructured WS2/CH3NH3PbI3 photoconductors with suppressed dark current and enhanced photodetectivity." *Advanced Materials*28.19 (2016): 3683-3689.

[35] De Sio, A., et al. "Electro-optical response of a single-crystal diamond ultraviolet photoconductor in transverse configuration." *Applied Physics Letters* 86.21 (2005): 213504.
[36] Kurimoto, Eiji, et al. "Electrophotographic photoconductor, and image forming method, image forming apparatus, and process cartridge using the electrophotographic photoconductor." U.S. Patent No. 9,291,924. 22 Mar. 2016.

[37] Liu, P., et al. "Fast, high-efficiency Germanium quantum dot photodetectors." *Lester Eastman Conference on High Performance Devices (LEC), 2012*. IEEE, 2012.
[38] Haddab, Y., P-A. Besse, and R. S. Popovic. "Quantized current jumps in silicon photoconductors at room temperature." *Journal of applied physics*86.7 (1999): 3787-3791.

[39] Brown, E. R., D. C. Driscoll, and A. C. Gossard. "State-of-the-art in 1.55 μm ultrafast InGaAs photoconductors, and the use of signal-processing techniques to extract the photocarrier lifetime." *Semiconductor science and technology* 20.7 (2005): S199.
[40] Xiong, Kanglin, et al. "Single crystal gallium nitride nanomembrane photoconductor and field effect transistor." *Advanced Functional Materials*24.41 (2014): 6503-6508.

[41] Jin, Zhiwen, et al. "High-performance flexible ultraviolet photoconductors based on solution-processed ultrathin ZnO/Au nanoparticle composite films." *Scientific reports* 4 (2014).
[42] Aller, Mario Méndez, et al. "Pulsed THz time domain system with ErAs: In (Al) GaAs photoconductors." *Infrared, Millimeter, and Terahertz waves (IRMMW-THz), 2016 41st International Conference on*. IEEE, 2016.

[43] Yang, Bin, et al. "Increased efficiency of low band gap polymer solar cells at elevated temperature and its origins." *Applied Physics Letters* 99.13 (2011): 206.
[44] Han, M., Guo, F. & Lu, Y. Optical fiber refractometer based on cladding-mode Bragg grating. *Optics Letters* **35**, 399-401 (2010).

[45]Jie, J. S., et al. "Photoconductive characteristics of single-crystal CdS nanoribbons." *Nano letters* 6.9 (2006): 1887-1892.

[46] Ristova, M., and M. Ristov. "Silver-doped CdS films for PV application." *Solar energy materials and solar cells* 53.1 (1998): 95-102.
[47] Jadhav, U. S., S. S. Kale, and C. D. Lokhande. "Effect of Cd: S ratio on the photoconducting properties of chemically deposited CdS films." *Materials Chemistry and physics* 69.1 (2001): 125-132.

[48] Kanemitsu, Yoshihiko, et al. "Free excitons in cubic CdS films." *Applied physics letters* 80.2 (2002): 267-269.
[49] Ye, Yu, et al. "High-performance single CdS nanobelt metal-semiconductor field-effect transistor-based photodetectors." *ACS Applied Materials & Interfaces* 2.10 (2010): 2724-2727.

[50] Sebastian, P. J., and M. Ocampo. "A photodetector based on ZnCdS nanoparticles in a CdS matrix formed by screen printing and sintering of CdS and ZnCl2." *Solar energy materials and solar cells* 44.1 (1996): 1-10.
[51] Sartale, S. D., and C. D. Lokhande. "Preparation and characterization of nickel sulphide thin films using successive ionic layer adsorption and reaction (SILAR) method." *Materials Chemistry and Physics* 72.1 (2001): 101-104.

[52] Dhumure, S. S., and C. D. Lokhande. "Studies on the preparation and characterization of chemically deposited Ag2S films from an acidic bath." *Thin Solid Films* 240.1-2 (1994): 1-6.
[53] Sankapal, B. R., R. S. Mane, and C. D. Lokhande. "Deposition of CdS thin films by the successive ionic layer adsorption and reaction (SILAR) method." *Materials research bulletin* 35.2 (2000): 177-184.

[54] Mooser, E., and M. Schlüter. "The band-gap excitons in gallium selenide." *Il Nuovo Cimento B (1971-1996)* 18.1 (1973): 164-208.
[55] Huang, Hai, et al. "Highly sensitive phototransistor based on GaSe nanosheets." *Applied Physics Letters* 107.14 (2015): 143112.

[56]Leontie, L., et al. "Photoelectric properties of Bi 2 O 3⁄ Ga Se heterojunctions." *Applied Physics Letters* 94.7 (2009): 071903.
[57] Fernelius, Nils C. "Properties of gallium selenide single crystal." *Progress in Crystal Growth and Characterization of materials* 28.4 (1994): 275-353.

[58]. N. M. Mekhtiev, Yu. V. Rud, and E. Yu. Salaev, Sov. Phys. Semicond. 12, 924 (1978).
[59] Shi, Wei, et al. "Efficient, tunable, and coherent 0.18–5.27-THz source based on GaSe crystal." *Optics letters* 27.16 (2002): 1454-1456.

[60] Mancini, A. M., et al. "The Use of GaSe Semiconductor Detectors for Monitoring High Energy Muon Beams." *IEEE Transactions on Nuclear Science* 23.1 (1976): 189-197.

[61] Manfredotti, C., et al. "A particular application of GaSe semiconductor detectors in the neutrino experiment at CERN." *Nuclear Instruments and Methods* 131.3 (1975): 457-462.
[62] Castellano, Alfredo. "GaSe detectors for x - ray beams." *Applied physics letters* 48.4 (1986): 298-299.

[63] Hu, PingAn, et al. "Synthesis of few-layer GaSe nanosheets for high performance photodetectors." *ACS nano* 6.7 (2012): 5988-5994.
[64] Parlak, M., A. F. Qasrawi, and C. Ercelebi. "Growth, electrical and structural characterization of β-GaSe thin films." *Journal of materials science* 38.7 (2003): 1507-1511.

[65] Tatsuyama, C., et al. "Substrate orientation dependence of the growth of GaSe thin films on GaAs." *Applied surface science* 117 (1997): 523-529.
[66] Vaidyanathan, Raman, et al. "Formation of In 2 Se 3 thin films and nanostructures using electrochemical atomic layer epitaxy." *Journal of Electroanalytical Chemistry* 559 (2003): 55-61.

[67] Cheon, Jinwoo, et al. "Metalorganic Chemical Vapor Deposition of Semiconducting III/VI In2Se3 Thin Films from the Single-Source Precursor: In [SeC (SiMe3) 3] 3." *Chemistry of materials* 7.12 (1995): 2273-2276.
[68] Groot, CH de, and J. S. Moodera. "Growth and characterization of a novel In 2 Se 3 structure." *Journal of Applied Physics* 89.8 (2001): 4336-4340.

[69] De Blasi, C., et al. "Growth and characterization of high qualitY InSe single crystals." *Materials Chemistry and Physics* 9.1-3 (1983): 55-64.
[70] De Blasi, C., et al. "Large InSe single crystals grown from stoichiometric and non-stoichiometric melts." *Journal of Crystal Growth* 57.3 (1982): 482-486.

[71] Popović, Stanko, et al. "Revised and new crystal data for indium selenides." *Journal of Applied Crystallography* 12.4 (1979): 416-420.
[72] Chevy, A., A. Kuhn, and M-S. Martin. "Large InSe monocrystals grown from a non-stoichiometric melt." *Journal of Crystal Growth* 38.1 (1977): 118-122.

[73] Hu, PingAn, et al. "Synthesis of few-layer GaSe nanosheets for high performance photodetectors." *ACS nano* 6.7 (2012): 5988-5994.
[74] Lei, Sidong, et al. "Synthesis and photoresponse of large GaSe atomic layers." *Nano letters* 13.6 (2013): 2777-2781.

[75] Lei, Sidong, et al. "Evolution of the electronic band structure and efficient photo-detection in atomic layers of InSe." *ACS nano* 8.2 (2014): 1263-1272.
[76] Mudd, Garry W., et al. "Tuning the bandgap of exfoliated InSe nanosheets by quantum confinement." *Advanced Materials* 25.40 (2013): 5714-5718.

[77] Mudd, Garry W., et al. "Tuning the bandgap of exfoliated InSe nanosheets by quantum confinement." *Advanced Materials* 25.40 (2013): 5714-5718.
[78] Cheon, Jinwoo, et al. "Metalorganic Chemical Vapor Deposition of Semiconducting III/VI In2Se3 Thin Films from the Single-Source Precursor: In [SeC (SiMe3) 3] 3." *Chemistry of materials* 7.12 (1995): 2273-2276.

[79] Kuroda, N., and Y. Nishina. "Resonance Raman scattering study on exciton and polaron anisotropies in InSe." *Solid State Communications* 34.6 (1980): 481-484.
[80] Kress-Rogers, E., et al. "Cyclotron resonance studies on bulk and two-dimensional conduction electrons in InSe." *Solid State Communications* 44.3 (1982): 379-383.

[81] Kress-Rogers, E., et al. "Cyclotron resonance studies on bulk and two-dimensional conduction electrons in InSe." *Solid State Communications* 44.3 (1982): 379-383.
[82]Camassel, J., et al. "Excitonic absorption edge of indium selenide." *Physical Review B* 17.12 (1978): 4718.

[83] Martínez - Pastor, J., et al. "Electrical and photovoltaic properties of indium - tin - oxide/p - InSe/Au solar cells." *Journal of applied physics* 62.4 (1987): 1477-1483.
[84] Shi, Wei, and Yujie J. Ding. "A monochromatic and high-power terahertz source tunable in the ranges of 2.7–38.4 and 58.2–3540 μm for variety of potential applications." *Applied physics letters* 84.10 (2004): 1635-1637.

[85] Kaindl, R. A., et al. "Broadband phase-matched difference frequency mixing of femtosecond pulses in GaSe: Experiment and theory." *Applied Physics Letters* 75.8 (1999): 1060-1062.
[86] Gordillo, G., and C. Calderon. "CIS thin film solar cells with evaporated InSe buffer layers." *Solar energy materials and solar cells* 77.2 (2003): 163-173.

[87] Katerinchuk, V. N., and M. Z. Kovalyuk. "Homogeneous pn InSe photodiodes." *Soviet physics. Semiconductors* 25.5 (1991): 577-579.
[88] Bernede, J. C., and S. Marsillac. "Band alignment at the interface of a SnO2/γ-In2Se3 heterojunction." *Materials research bulletin* 32.9 (1997): 1193-1200.

[89] Marsillac, S., and J. C. Bernede. "New γ-In 2 Se 3/TCO (SnO 2 or ZnO) thin film rectifying heterojunction." *Thin Solid Films* 315.1 (1998): 5-8.
[90]Manno, D., et al. "Structural and electrical properties of In2O3/SeO2 thin films for gas-sensing applications." *Journal of Physics D: Applied Physics*34.14 (2001): 2097.

[91] Koshkin, V. M., et al. "Unstable equilibrium and radiation defects in solids." *Solid State Communications* 13.1 (1973): 1-4.

[92] Kenawy, M. A., et al. "Electrical and switching properties of InSe amorphous thin films." *Thin Solid Films* 200.2 (1991): 203-210.
[93] Niquet, Y. M., et al. "Quantum confinement in germanium nanocrystals." *Applied Physics Letters* 77.8 (2000): 1182-1184.

[94] Bostedt, C., et al. "Strong quantum-confinement effects in the conduction band of germanium nanocrystals." *Applied physics letters* 84.20 (2004): 4056-4058.
[95] Günal, I., and A. F. Qasrawi. "Temperature effects on the properties of Ge thin films." *Journal of materials science* 34.20 (1999): 5033-5037.

[96] Morii, Kiyohito, et al. "High performance GeO 2/Ge nMOSFETs with source/drain junctions formed by gas phase doping." *Electron Devices Meeting (IEDM), 2009 IEEE International*. IEEE, 2009.
[97] Bao, Yiliang, et al. "Germanium pn junctions by laser doping for photonics/microelectronic devices." *IEEE Photonics Technol. Lett* 26.14 (2014): 1422-1425.

[98]Günal, I., and A. F. Qasrawi. "Temperature effects on the properties of Ge thin films." *Journal of materials science* 34.20 (1999): 5033-5037.
[99] Brunco, D. P., et al. "Germanium MOSFET devices: Advances in materials understanding, process development, and electrical performance." *Journal of The Electrochemical Society* 155.7 (2008): H552-H561.

[100] Yuan, J., B. Chen, and A. L. Holmes. "Near-infrared quantum efficiency of uncooled photodetectors based on InGaAs/GaAsSb quantum wells lattice-matched to InP." *Electronics letters* 47.20 (2011): 1144-1145.
[101] B. Chen et al., "Natural lithography nano-sphere texturing as antireflective layer on InGaAs PIN photodiodes," Electron.
Lett., vol. 48, pp. 1340–1341, 2012

[102] Kumar, Vipin, et al. "Polycrystalline ZnS thin films by screen printing method and its characterization." *Chalcogenide letters* 5.11 (2008): 289-295.
[103] Antony, A., et al. "The effect of the pH value on the growth and properties of chemical-bath-deposited ZnS thin films." *Materials Chemistry and Physics*90.1 (2005): 106-110.

[104] Borah, Jyoti P., J. Barman, and K. C. Sarma. "Structural and optical properties of ZnS nanoparticles." *Chalcogenide Lett* 5.9 (2008): 201-208.
[105] Moore, Daniel, and Zhong L. Wang. "Growth of anisotropic one-dimensional ZnS nanostructures." *Journal of Materials Chemistry* 16.40 (2006): 3898-3905.

[106] Nizamoglu, Sedat, et al. "White light generation using CdSe/ZnS core–shell nanocrystals hybridized with InGaN/GaN light emitting diodes." *Nanotechnology* 18.6 (2007): 065709.

[107] Ledger, Anthony M. "Inhomogeneous interface laser mirror coatings." *Applied optics* 18.17 (1979): 2979-2989.
[108] Moore, Daniel, and Zhong L. Wang. "Growth of anisotropic one-dimensional ZnS nanostructures." *Journal of Materials Chemistry* 16.40 (2006): 3898-3905.

[109] Zhang, Haitao, et al. "Preparation of sensitized ZnS and its photocatalytic activity under visible light irradiation." *Journal of Physics D: Applied Physics*40.21 (2007): 6846.
[110] Wu, Peng, et al. "A Multidimensional Sensing Device for the Discrimination of Proteins Based on Manganese - Doped ZnS Quantum Dots." *Angewandte Chemie International Edition* 50.35 (2011): 8118-8121.

[111] Mirov, S.; Fedorov, W.; Graham, K.; Moskalev, I.; Badikov, V.; Panyutin, V.: Erbium Fiber Laser–Pumped Continuous-Wave Microchip Cr2+:ZnS and Cr2+:ZnSe Lasers. Optics Letters 2002, 27, 909-911.
[112] Devi, BS Rema, R. Raveendran, and A. V. Vaidyan. "Synthesis and characterization of Mn2+-doped ZnS nanoparticles." *energy* 2 (2007): 2e.

[113] Han, Jiaguang, et al. "Far-infrared characteristics of ZnS nanoparticles measured by terahertz time-domain spectroscopy." *The Journal of Physical Chemistry B* 110.5 (2006): 1989-1993.
[114] Bouhafs, D., et al. "Design and simulation of antireflection coating systems for optoelectronic devices: Application to silicon solar cells." *Solar Energy Materials and Solar Cells* 52.1 (1998): 79-93.

[115] Elidrissi, B., et al. "Structure, composition and optical properties of ZnS thin films prepared by spray pyrolysis." *Materials Chemistry and Physics* 68.1 (2001): 175-179..
[116] Elidrissi, B., et al. "Structure, composition and optical properties of ZnS thin films prepared by spray pyrolysis." *Materials Chemistry and Physics* 68.1 (2001): 175-179.

[117] Yoneta, Minoru, et al. "Low temperature molecular beam epitaxial growth of ZnS/GaAs (001) by using elemental sulfur source." *Journal of crystal growth*127.1-4 (1993): 314-317.
[118] Goudarzi, Alireza, et al. "Ammonia-free chemical bath deposition of nanocrystalline ZnS thin film buffer layer for solar cells." *Thin Solid Films*516.15 (2008): 4953-4957.

[119] O'Brien, Paul, and John McAleese. "Developing an understanding of the processes controlling the chemical bath deposition of ZnS and CdS." *Journal of Materials Chemistry* 8.11 (1998): 2309-2314.
[120] Kim, Yong Shin, and Sun Jin Yun. "Studies on polycrystalline ZnS thin films grown by atomic layer deposition for electroluminescent applications." *Applied surface science* 229.1 (2004): 105-111.

[121] Shao, Le-Xi, Kuen-Huei Chang, and Huey-Liang Hwang. "Zinc sulfide thin films deposited by RF reactive sputtering for photovoltaic applications." *Applied Surface Science* 212 (2003): 305-310.
[122]Chyi, J - I., et al. "Molecular beam epitaxial growth and characterization of InSb on Si." *Applied physics letters* 54.11 (1989): 1016-1018.

[123]J. I. Pankove, Optical process in semiconductors (Dover Publications, Inc. New York 1971), p. 3, 34.
[124]Bardeen, J., F. J. Blatt, and L. H. Hall. "Proceedings of the Conference on Photoconductivity, Atlantic City, November 4-6, 1954." (1956): 146.
[125] M. Fox, Optical Properties of Solids, Second Edi (Oxford University Press, New York, 2010).

[126] Tauc, Jan. "Optical properties and electronic structure of amorphous Ge and Si." *Materials Research Bulletin* 3.1 (1968): 37-46.
[127] J.I. Pankove, *Optical Processes in Semiconductors* (Dover Publications, New York, 1975).

[128]Huxter, Vanessa M., et al. "Demonstration of bulk semiconductor optical properties in processable Ag2S and EuS nanocrystalline systems." *Advanced Materials* 20.12 (2008): 2439-2443.
[129] Congreve, Daniel N., et al. "External quantum efficiency above 100% in a singlet-exciton-fission–based organic photovoltaic cell." *Science* 340.6130 (2013): 334-337.

[130]Söderström, K., et al. "Highly reflective nanotextured sputtered silver back reflector for flexible high-efficiency n–i–p thin-film silicon solar cells." *Solar Energy Materials and Solar Cells* 95.12 (2011): 3585-3591.
[131] Hu, Linfeng, et al. "Ultrahigh external quantum efficiency from thin SnO2 nanowire ultraviolet photodetectors." *small* 7.8 (2011): 1012-1017.

[132]Chandrasekaran, J., et al. "Hybrid solar cell based on blending of organic and inorganic materials—An overview." *Renewable and Sustainable Energy Reviews* 15.2 (2011): 1228-1238.
[133] Pospischil, Andreas, et al. "Integration of graphene photodetectors with silicon-on-insulator waveguides." *CLEO: Science and Innovations*. Optical Society of America, 2013.

[134] Lee, Youngbin, et al. "High - performance perovskite–graphene hybrid photodetector." *Advanced materials* 27.1 (2015): 41-46.
[135] Ulaganathan, Rajesh Kumar, et al. "High photosensitivity and broad spectral response of multi-layered germanium sulfide transistors." *Nanoscale* 8.4 (2016): 2284-2292.

[136] Ulaganathan, Rajesh Kumar, et al. "High photosensitivity and broad spectral response of multi-layered germanium sulfide transistors." *Nanoscale* 8.4 (2016): 2284-2292.

[137] khmayies, Shadia Jamil, and Riyad N. Ahmad-Bitar. "A study of the optical bandgap energy and Urbach tail of spray-deposited CdS: In thin films." *Journal of Materials Research and Technology* 2.3 (2013): 221-227).

[138] J. I. Pankove" ,Optical processes in semiconductors) "New Jersey: Prentice-Hall) p. 93 (1971
[139] Soltani, Nayereh, et al. "Influence of the polyvinyl pyrrolidone concentration on particle size and dispersion of ZnS nanoparticles synthesized by microwave irradiation." *International journal of molecular sciences* 13.10 (2012): 12412-12427

[140] Zhang, Kaiyou, et al. "Stable and highly photosensitive device of CdSe nanorods." *Physica E: Low-dimensional Systems and Nanostructures* 43.4 (2011): 943-947.
[141] Qasrawi, A. F. "Refractive index, band gap and oscillator parameters of amorphous GaSe thin films." *Crystal Research and Technology* 40.6 (2005): 610-614.

[142] Hwang, Dong Hyun, et al. "Structural and optical properties of ZnS thin films deposited by RF magnetron sputtering." *Nanoscale research letters* 7.1 (2012): 26.
[143] Lei, Sidong, et al. "Evolution of the electronic band structure and efficient photo-detection in atomic layers of InSe." *ACS nano* 8.2 (2014): 1263-1272.
[144] Mahdi, M. A., et al. "Synthesis and characterization of single-crystal CdS nanosheet for high-speed photodetection." *Physica E: Low-dimensional Systems and Nanostructures* 44.7 (2012): 1716-1721.
[145] D. Decoster, J. Harari, Optoelectronic Sensor, ISTE Ltd, London, U.K, 2009.

[146]Jie, J. S., et al. "Photoconductive characteristics of single-crystal CdS nanoribbons." *Nano letters* 6.9 (2006): 1887-1892.
[147]Fan, Zhiyong, et al. "Photoluminescence and polarized photodetection of single ZnO nanowires." *Applied Physics Letters* 85.25 (2004): 6128-6130.

[148] Yu, Wenzhi, et al. "Near - Infrared Photodetectors Based on MoTe2/Graphene Heterostructure with High Responsivity and Flexibility." *Small* (2017).
[149] Sorokin, A. A., et al. "Photoelectric effect at ultrahigh intensities." *Physical review letters* 99.21 (2007): 213002.
[150] Li, Liang, et al. "Single - crystalline CdS nanobelts for excellent field - emitters and ultrahigh quantum - efficiency photodetectors." *Advanced Materials* 22.29 (2010): 3161-3165.

[151] Konstantatos, Gerasimos, et al. "Sensitive solution-processed visible-wavelength photodetectors." *Nature photonics* 1.9 (2007): 531-534.
[152] Ai, Na, et al. "Achieving high sensitivity in single organic submicrometer ribbon based photodetector through surface engineering." *Organic Electronics* 14.4 (2013): 1103-1108.

[153]Ohsawa, Jun, et al. "Low-dark-current large-area narrow-band photodetector using InGaN/GaN layers on sapphire." *Japanese journal of applied physics*44.5L (2005): L623.
[154]Jie, J. S., et al. "Photoconductive characteristics of single-crystal CdS nanoribbons." *Nano letters* 6.9 (2006): 1887-1892.
[155] Wang, Qing, et al. "Characteristics of high efficiency dye-sensitized solar cells." *The Journal of Physical Chemistry B*110.50 (2006): 25210-25221.
[156] Zheng, X. J., et al. "Photoconductive semiconductor switch based on ZnS nanobelts film." *Sensors and Actuators B: Chemical* 147.2 (2010): 442-446.

[157] Xie, Chao, et al. "Photodetectors Based on Two - Dimensional Layered Materials Beyond Graphene." *Advanced Functional Materials* 27.19 (2017).
[158] Alexander, J. Nicholas, et al. "Deposition and characterization of cadmium sulfide (CdS) by chemical bath deposition using an alternative chemistry cadmium precursor." *Solar Energy Materials and Solar Cells* 125 (2014): 47-53.

[159] Mamy, R., et al. "Au/InSe Schottky barrier height determination." *Revue de Physique Appliquée* 25.9 (1990): 947-950.
[160]Svatek, S. A., et al. "Graphene-InSe-graphene van der Waals heterostructures." *Journal of Physics: Conference Series*. Vol. 647. No. 1. IOP Publishing, 2015.

[161] Lei, Sidong, et al. "An atomically layered InSe avalanche photodetector." *Nano letters* 15.5 (2015): 3048-3055.
[162]Island, Joshua O., et al. "Gate controlled photocurrent generation mechanisms in high-gain In2Se3 phototransistors." *Nano letters* 15.12 (2015): 7853-7858.

[163] Chen, Zhesheng, Johan Biscaras, and Abhay Shukla. "A high performance graphene/few-layer InSe photo-detector." *Nanoscale* 7.14 (2015): 5981-5986.
[164]He, Yi Ting, et al. "Internal quantum efficiency droop of GaN LED." *Solid State Lighting (SSLCHINA), 2014 11th China International Forum on*. IEEE, 2014.

[165] Owolabi, Taoreed O., Kabiru O. Akande, and Sunday O. Olatunji. "Support vector machines approach for estimating work function of semiconductors: addressing the limitation of metallic plasma model." *Applied Physics Research* 6.5 (2014): 122.
[166] Porter, N. A., J. Carter Gartside, and C. H. Marrows. "Scattering mechanisms in textured FeGe thin films: Magnetoresistance and the anomalous Hall effect." *Physical Review B* 90.2 (2014): 024403.

[167] D. Decoster, J. Harari, Optoelectronic Sensor, ISTE Ltd, London, U.K, 2009.
[168] Cho, Minkyu, et al. "Resonant cavity germanium photodetector via stacked single-crystalline nanomembranes." *Journal of Vacuum Science & Technology B, Nanotechnology and Microelectronics: Materials, Processing, Measurement, and Phenomena* 34.4 (2016): 040604.

[169]Ramasamy, Parthiban, et al. "Solution synthesis of GeS and GeSe nanosheets for high-sensitivity photodetectors." *Journal of Materials Chemistry C* 4.3 (2016): 479-485.
[170] Hu, PingAn, et al. "Synthesis of few-layer GaSe nanosheets for high performance photodetectors." *ACS nano* 6.7 (2012): 5988-5994.
[171] Fang, X. S., et al. "Ultrafine ZnS nanobelts as field emitters." *Advanced Materials* 19.18 (2007): 2593-2596.
[172] Fang, Xiaosheng, et al. "Single - crystalline ZnS nanobelts as ultraviolet - light sensors." *Advanced Materials* 21.20 (2009): 2034-2039
[173]Zhao, H., et al. "Controlling photoinduced electron transfer from PbS@ CdS core@ shell quantum dots to metal oxide nanostructured thin films." *Nanoscale* 6.12 (2014): 7004-7011.
[174]Mudd, Garry W., et al. "High Broad - Band Photoresponsivity of Mechanically Formed InSe–Graphene van der Waals Heterostructures." *Advanced Materials* 27.25 (2015): 3760-3766

Conferences

- Sufyan Rateb Shehada, Muayad Abu Saa, Hazem. Khanfar, A. F. Qasrawi. Fabrication and Characterization of Wide Band Photoconductor Array(oral presentation), Second Palestinian International Graduate Conference on Natural, Medical and Health Sciences and Humanities (SPIGCNMHSH 2017), An-Najah National University-Nablus. 2017.
- Sufyan Rateb Shehada, A. F. Qassrawi, Exploring External Quantum Efficiency, PhotoResponsivity, Photosensitivity of InSe/GaSe/Ga2S3 photodiode arrays (poster), Fifth Palestinian Conference on Modern Trends in Mathmetics and Physics, Arab American University-Jenin. 2016.

تصميم ودراسة حزمة موصلات ضوئية واسعة المدى

اعداد

سفيان راتب سليم شحادة

اشراف

دكتور مؤيد ابو صاع

والمشرف

دكتور حازم خنفر

الملخص

في هذه الدراسة تم تصميم موصلات ضوئية واسعة المدى من مواد ذات طاقة تتراوح من 1.1 الى 3.33 الكترون فولت . حزمة الموصلات الضوئية تم تصنيعها من كبريتيد الكادميوم,غاليوم سيلينيد, إنديوم سيلينايد, جرمانيوم وكبريتيد الزنك .حزمة الموصلات الضوئية تم دراستها تحت تاثير انواع مختلفة من الليزرذات اطوال موجية 406 ,632 و850 نانومتر وتحت تاثير ضوء التنجستون . اتاحت هذه القياسات الحساسية الضوئية والاستجابة الضوئية وكفاءة الكم الداخلية و كفاءة الكم الخارجية .

الحساسية الضوئية والتيار الضوئي ازداد بزيادة قدرة الليزرات وضوء التنجستون . لكن كفاء الكم الداخلية وكفاءة الكم الخرجية والاستجابة الضوئية قلت بزيادة قدرة الليزرات وضوء التنجستون.

اكبر قيمة للحساسية الضوئية تم تسجيلها لكبريتيد الكادميوم و اكبر قيمة للتيار الضوئي تم تسجيلها لحزمة الموصلات الضوئية المتصلة . لكن اكبر قيمة لكفاءة الكم الداخلية وكفاءة الكم الخارجية والاستجابة الضوئية تم تسجيلها لإنديوم سيلينايد.